ADVANCED METHODS FOR LIGHT TRAPPING IN OPTICALLY THIN SILICON SOLAR CELLS

by

James Richard Nagel

A dissertation submitted to the faculty of
The University of Utah
in partial fulfillment of the requirements for the degree of

Doctor of Philosophy

Department of Electrical and Computer Engineering

The University of Utah

December 2011

The University of Utah Graduate School

STATEMENT OF DISSERTATION APPROVAL

The dissertation of **James Richard Nagel**

has been approved by the following supervisory committee members:

Michael Scarpulla	, Chair	**10/26/11** Date Approved
Cynthia Furse	, Member	**10/26/11** Date Approved
Steve Blair	, Member	**10/26/11** Date Approved
Gerald Stringfellow	, Member	**10/2811** Date Approved
Rajesh Menon	, Member	**10/26/11** Date Approved

and by **Gianluca Lazzi** , Chair of the Department of **Electrical and Computer Engineering**

and by Charles A. Wight, Dean of The Graduate School.

ABSTRACT

The field of *light trapping* is the study of how best to absorb light in a thin film of material when most light either reflects away at the surface or transmits straight through to the other side. This has tremendous application to the field of photovoltaics where thin silicon films can be manufactured cheaply, but also fail to capture all of the available photons in the solar spectrum. Advancements in light trapping therefore bring us closer to the day when photovoltaic devices may reach grid parity with traditional fossil fuels on the electrical energy market.

This dissertation advances our understanding of light trapping by first modeling the effects of loss in planar dielectric waveguides. The mathematical framework developed here can be used to model any arbitrary three-layer structure with mixed gain or loss and then extract the total field solution for the guided modes. It is found that lossy waveguides possess a greater number of eigenmodes than their lossless counterparts, and that these "loss guided" modes attenuate much more rapidly than conventional modes.

Another contribution from this dissertation is the exploration of light trapping through the use of dielectric nanospheres embedded directly within the active layer of a thin silicon film. The primary benefit to this approach is that the device can utilize a surface nitride layer serving as an antireflective coating while still retaining the benefits of light trapping within the film. The end result is that light trapping and light injection are effectively decoupled from each other and may be independently optimized within a single photovoltaic device.

The final contribution from this work is a direct numerical comparison between multiple light trapping schemes. This allows us to quantify the relative performances of various design techniques against one another and objectively determine which ideas tend to capture the most light. Using numerical simulation, this work directly compares the absorption gains due to embedded nanoparticles, surface textures, antireflective coatings, and plasmonic nanospheres. This work also introduces a new mathematical metric for differentiating between index matching and angular scattering at a textured surface. Such information will prove useful in guiding future scientific efforts in the fields of light trapping and light management in thin film photovoltaics.

CONTENTS

LIST OF FIGURES

ACKNOWLEDGEMENTS

I would like to extend my gratitude and appreciation to the following individuals:

Dr. Michael Scarpulla, for recruiting me into the project, for his guidance with my research, and for his patience with my learning.

Dr. Cynthia Furse, for providing me with countless opportunities and for always encouraging my creative endeavors. I would not be here without her.

Dr. Steve Blair for his excellent technical support and advice. This research has been vastly improved because of him.

All those who have supported me with friendship and encouragement.

And of course, my parents, Barbara and David Nagel, for encouraging me to work hard and for always supporting me in my goals.

CHAPTER 1

INTRODUCTION

With the rising costs of fossil fuels and the growing desire for security in our national energy infrastructure, demand for renewable energy has been steadily growing in recent years. This has led to enormous research expenditures into cost-effective technologies for harvesting energy from wind, solar, geothermal, and tidal resources. In particular, photovoltaics (PV), the direct conversion of sunlight into electrical current, is an especially promising technology with vast, untapped potential. Unfortunately, current PV technologies are still unable to economically compete with traditional grid-level sources on the electrical energy market. The desire for "grid parity" has therefore led to a strong national focus on an ultimate utility-scale cost of one dollar per watt by the year 2017 [1, 2]. This target represents the combined cost of the PV module itself ($0.50/W), power inversion equipment ($0.10/W), and any "balance of system" (BOS) costs that include such factors as installation, mechanical mounting, energy storage, and tracking ($0.40/W).

Although power inversion and BOS costs are expected to decline through advances in process design and system integration, PV modules will require fundamental revision to the underlying technologies upon which they are based. For instance, the ideal choice of semiconductor material for the PV substrate is still an open issue, and many candidates are openly competing for market share [3]. One high-profile candidate is cadmium telluride (CdTe), which became a major contender in 2009 when it reached $0.98/W for commercial PV modules [4]. Yet despite this economic advantage, CdTe faces many obstacles that potentially limit its growth in the near future [5]. One of the more pressing of these is the fact that cadmium and tellurium are primarily harvested as the byproducts of zinc and copper production. This places an upper limit to the amount of material that may be produced in a given year. It is also questionable as to whether there is sufficient mineral resource available worldwide to accommodate global electrical demand in the near future [3]. Such obstacles illustrate the nature of the many economic challenges faced by leading contenders in the PV energy market. The future of PV technology therefore remains an open issue with many technologies fiercely competing within the industry.

1.1 Thin-Film Silicon

In principle, the optimal PV material should be nontoxic, abundant in the Earth's crust, optimal in bandgap, and easily processed on an industrial scale [6]. One example of such a viable candidate is copper-zinc-tin-sulfide (Cu_2ZnSnS_4), and great research efforts are currently exploring the potential PV applications of this material [7]. Iron pyrite (FeS_2) is another example semiconductor that has been researched for similar reasons [8]. However, of all the competing choices in the current market, one of the most promising candidates by far is silicon [9, 10]. Not only does silicon satisfy the many requirements for a viable PV technology, but there already exists a multibillion dollar infrastructure dedicated to the production of semiconductor-grade material. It is therefore no surprise that the PV market share has been dominated by silicon-based technologies for the last decade [11], and will likely continue to be so in the foreseeable future.

Despite the many advantages associated with silicon, there are still difficult challenges to overcome before reaching the target module cost of \$0.5/W. One of these has traditionally been the manufacturing cost of semiconductor-grade crystalline silicon (c-Si). For example, a typical high-efficiency silicon solar cell can readily achieve efficiencies of nearly 25 % in laboratory devices, but also requires a film thickness beyond 200–300 μm in order to do so [12]. Although this may not sound like very much, the raw semiconductor material in such a module can readily account for anywhere between 30–50 % of the total manufacturing cost in a commercial product [13].

In an effort to alleviate the material costs of traditional silicon-based PV, new designs have been developed that reduce bulk semiconductor thicknesses from the usual hundred-micron scale down to as little as 1.0 μm or less. These *thin film* designs are therefore exceptionally cheaper to manufacture on a large scale due to the vast reduction in material cost. Such technologies also have the added advantage of being able to deposit directly onto large areas as opposed to traditional solar panels which must be compiled together from individual wafers onto a large surface [14]. This has led to a tremendous boost in market share for thin-film devices, though they still remain a far cry from the \$0.5/W goal.

One of the major limitations of thin-film silicon is the fact that silicon is an indirect band gap semiconductor. This means that the top of the valence band in c-Si is at a different momentum state than the bottom of the conduction band. Consequently, if an electron is expected to capture a photon and jump between energy levels, conservation of momentum also requires the capture of an appropriate phonon. The net effect is that c-Si becomes a very poor light absorber when compared to direct band gap semiconductors like GaAs or

CdTe. This fact is illustrated in Figure 1.1, which plots the absorption lengths for c-Si and GaAs as a function of wavelength. Consequently, when film thicknesses reach as little as 1.0 μm, many incident photons will simply pass through the c-Si film unabsorbed. For this reason, thin-film solar cells based on c-Si have a difficult time reaching conversion efficiencies greater than 10–12 % [15]. Until this problem is remedied, such devices will continue to struggle for competitiveness on an open energy market.

1.2 The Solar Resource and Light Trapping

The foundation of all PV power generation is the influx of electromagnetic radiation from the sun. The actual availability of this resource varies greatly with such factors as weather conditions, latitude, and time of day, but statistically averages to a mean daily value for any given location on Earth's surface. One measure of this availability is the *Air Mass 1.5 Solar Reference* (AM 1.5), denoted as $\Phi_0(\lambda)$, which is a measure of incident solar radiation as a function of wavelength λ. Plotted in Figure 1.2, $\Phi_0(\lambda)$ represents the mean influx of solar

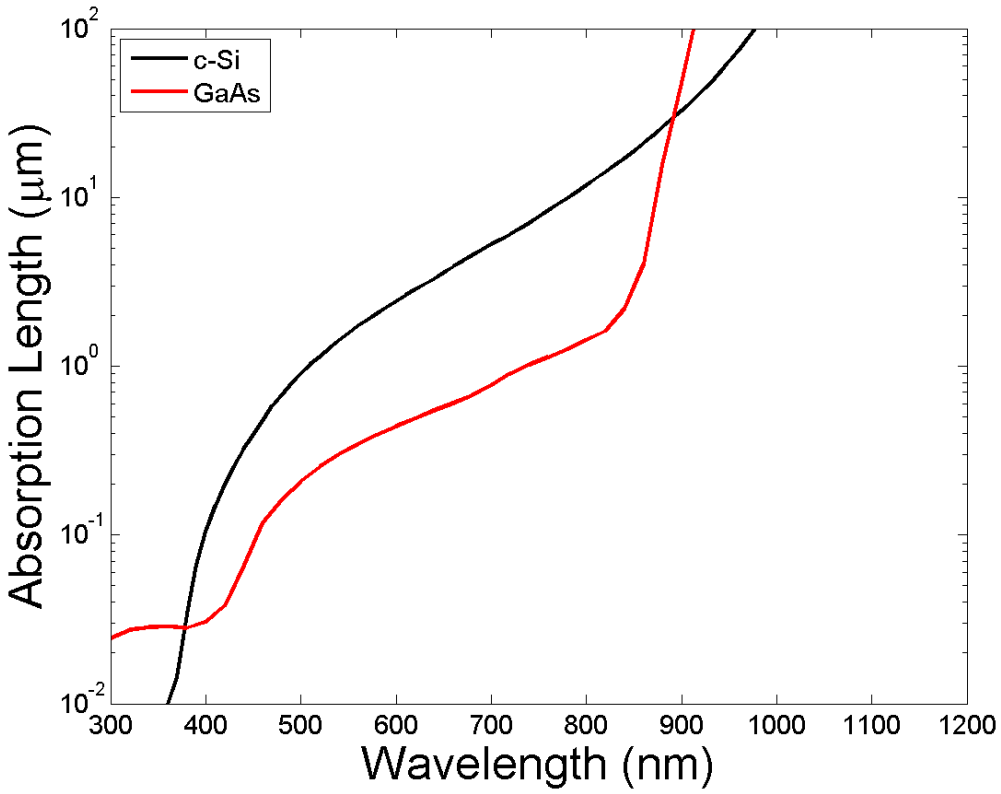

Figure 1.1. Absorption lengths for c-Si and GaAs. Note that the bandgap wavelength for GaAs is at 870 nm and becomes essentially lossless above this value.

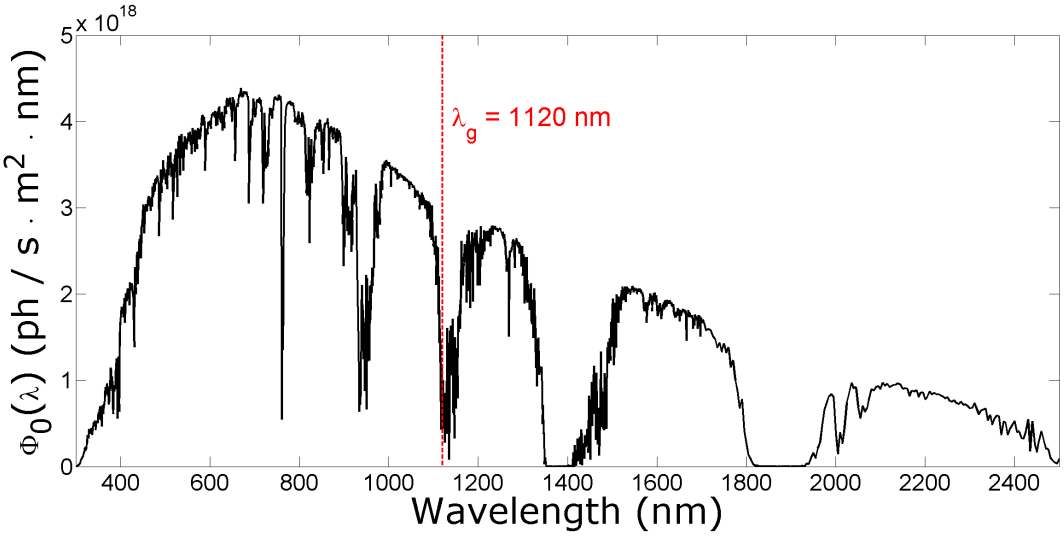

Figure 1.2. The AM 1.5 solar spectral reference. The red vertical line indicates the band gap for silicon. All photons to the left of this line possess enough energy to excite electrons in a c-Si solar cell.

power available to a generic collector within the continental United States [16]. This data is made available online for free by the National Renewable Energy Laboratory (NREL) [17], and is used as a standard benchmark for evaluating the performance of a PV device.

Ordinarily, $\Phi_0(\lambda)$ is expressed in units of $\mathrm{W}\cdot\mathrm{m}^{-2}\cdot\mathrm{nm}^{-1}$. However, for our purposes, it is convenient to convert $\Phi_0(\lambda)$ into units of photonic flux density, or $\mathrm{photons}\cdot\mathrm{s}^{-1}\cdot\mathrm{m}^{-2}\cdot\mathrm{nm}^{-1}$. This is to emphasize the fact that absorption of a single photon, no matter what its energy, can only create a single electron-hole pair. Any extra energy within a photon that exceeds the band gap of the material is generally unusable and wasted as heat. The total power output of a PV device is therefore proportional to the total number of captured photons and not necessarily to the actual energy contained within them. For the case of crystalline silicon, the band gap energy is approximately 1.11 eV, corresponding to a photon wavelength of $\lambda_g = 1120$ nm. This value is indicated by the vertical bar in the figure. All photons to the left of this bar can be readily converted into electrical current, while all photons to the right are generally unusable by a c-Si solar cell.

To understand the absorption problem of thin film PV, consider a 1.0 μm film of c-Si deposited onto a perfect electrical conductor (PEC). Shown in Figure 1.3(a), such a model is an idealized representation of the basic geometry of a thin-film solar cell. If this device is irradiated by the AM 1.5 spectrum, then some fraction of that incident light will be absorbed by the c-Si layer and converted into electron-hole pairs. The rest of those photons

will then simply reflect away from the device and are never seen again. A graph of the absorbed photons within the c-Si film as a function of wavelength is called an *absorbance spectrum*, and is indicated by the red curve in Figure 1.3(b). Using numerical integration, we can also count the total number of photons that are absorbed by the c-Si film and divide them by the total available photons from the AM 1.5 spectrum. The result is a *spectrally integrated absorption efficiency*, or IAE, of 27 % of all photons with wavelengths below λ_g. Clearly, this leaves a great deal of room for improvement!

Due to the poor absorption limits imposed by thin c-Si films, *antireflection* and *light trapping* have emerged as intense areas of scientific study. In principle, antireflection is simply a tool that minimizes the initial reflection of light at the top surface of the cell, thereby maximizing the injection of light into the film. This is commonly achieved through impedance matching methods like the simple step-index antireflection coating described in Chapter 2.2 of this dissertation. More advanced methods include such schemes as graded index coatings [18] or pyramidal surfaces [19]. In contrast, light trapping describes any mechanism by which incident radiation is scattered laterally within the film region after it has entered. This principle can be understood by realizing that the total collecting area of a typical thin-film device is many square-centimeters or even square-meters in size. So although the film region itself may be too thin to completely absorb photons at normal incidence, there is virtually unlimited thickness along the lateral directions for light to propagate through.

To visualize the principles of light trapping, consider the diagram in Figure 1.4(a). In this case, the same 1.0 μm film has been treated with a special roughened surface known as a *Lambertian* scatterer. For the special case of isotropic illumination over a low-loss film with large optical thickness, it can even be shown that such a surface actually produces the theoretical upper-limit to absorption that can possibly occur [20, 21, 22]. This makes the Lambertian scatterer a commonly-used benchmark for evaluating the general performance of a given light-trapping scheme. The absorption spectrum for a 1.0 μm film is therefore plotted in Figure 1.4(b), which leads to 81 % absorption of the available photons. This is often referred to as the *Yablonovitch limit*, the *ergodic limit*, or the *Lambertian limit*. So although it is not quite 100 %, it is still many times greater than the original 27 % produced by a bare surface alone.

Because the ergodic limit is such a popular benchmark, research in the area of light-trapping is generally focused on finding new ways to reach, or even exceed, this value. Many publications exist, but the majority of them can generally be categorized into a few specific

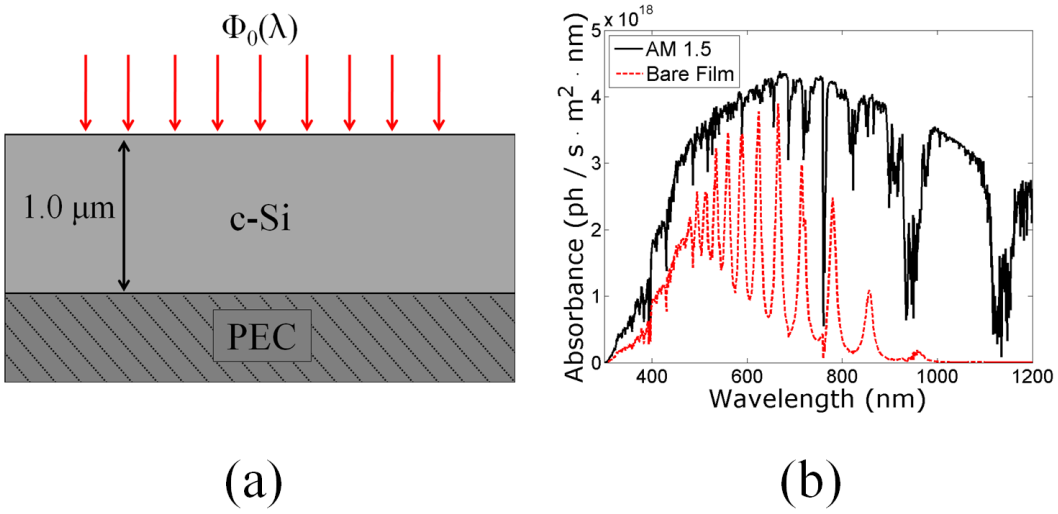

Figure 1.3. Optical absorption in a simplified solar cell model. (a) A bare film of c-Si is deposited on a perfect electrical conductor and illuminated by the AM 1.5 spectrum. (b) Absorbance spectrum of the 1.0 μm film. Total photonic absorption is only 27 % of the available photons below λ_g.

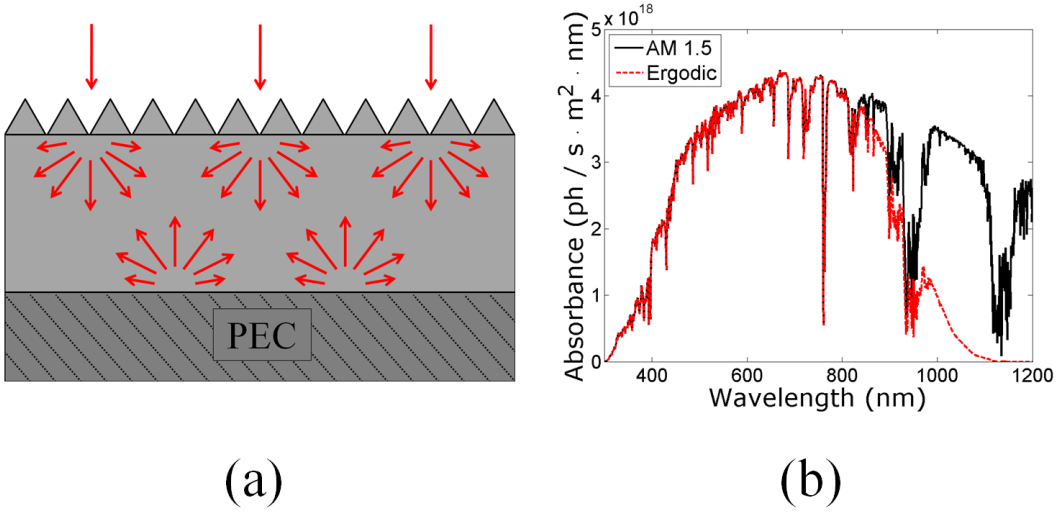

Figure 1.4. Optical absorption with light trapping. (a) The same 1.0 μm film of c-Si with Lambertian scattering along the surfaces. (b) Corresponding absorbance spectrum at the ergodic limit. Photonic absorption is now 81 % of the available total.

areas. For example, surface texturing is an effective tool that has been demonstrated via etched pyramids [23], rectangular trenches [24], and random roughness [25]. Back-contact texturing is another effective tool for scattering light after entering the semiconductor layer [26]. Plasmonic nanoparticles placed along the surface or rear of the cell have likewise demonstrated light-trapping properties [27]. All of these techniques perform with varying degrees of success, and all share the same goal of maximizing light capture within the film.

Despite the reported success of these many strategies, some tend to be at odds with other well-established methods for increased light absorption. For instance, an antireflective coating (ARC) is a simple and effective tool that eliminates surface reflections by depositing a thin layer of dielectric on top of a bare cell. For the case of the 1.0 μm film in Figure 1.3(a), an ideal ARC can even lead to an IAE of 40 % of the available photons. However, plasmonic nanospheres deposited along the surface of a solar cell will often diminish the overall absorption efficiency of the device when used in conjunction with a simple nitride layer [28, 29]. Surface texturing likewise faces similar setbacks, despite the tremendous success in its theoretical light-trapping abilities. One example is the increase in surface recombination and sheet resistivity that occurs within the texture itself. Other issues can arise in ultra-thin films below 1.0 μm, where the necessary dimensions required for efficient surface texturing can easily exceed the total film thickness. The ability to economically fabricate a quality surface texture over large surface areas is likewise a legitimate concern. It is therefore currently an open issue as to which light-trapping designs will prevail in the open market.

1.3 Contributions

This dissertation seeks to improve on our knowledge about the fundamental physics of light propagation in lossy planar structures. This will be accomplished by modeling a solar cell as a layered dielectric structure and then directly solving for the total electric and magnetic field distributions according to Maxwell's equations. For the case of excitation by an external source, this problem has been well-studied and shall be reviewed for the benefit of the reader. However, for the case of wave guidance in the longitudinal direction, the full-field solution still contains gaps in our scientific understanding. This dissertation therefore directly solves for the analytical field profiles of an electromagnetic wave that is guided by a lossy dielectric structure.

Another contribution from this dissertation is the exploration of light trapping through the use of dielectric nanospheres embedded directly within the active layer of a thin silicon film. This concept is similar to the use of plasmonic nanoparticles placed along the surface

of a solar cell, but merely shifts the location of the scatterers. The primary benefit to this approach is that the device can utilize a surface nitride layer serving as an ARC while still retaining the benefits of light trapping within the film. The end result is that light trapping and light injection are effectively decoupled from each other and may be independently optimized within a single PV device.

The final contribution from this work is a comparison between multiple light-trapping schemes. This will allow us to quantify the relative performance of various design techniques against one another and objectively determine which ideas tend to capture the most light. Using numerical simulation, it is possible to directly compare the absorption due to embedded nanoparticles, surface textures, antireflective coatings, and plasmonic nanospheres. Such information will prove useful in determining which methods provide the greatest efficiency gains in a thin film device and help guide future efforts in scientific research.

1.4 Summary Outline

This dissertation is organized as follows:

Chapter 2, *Electromagnetic Fundamentals for Photovoltaic Modeling*, provides a basic mathematical introduction to electromagnetic propagation in planar dielectric structures. It also introduces the reader to such concepts as optical path length and path length enhancement, which are frequently referenced throughout this dissertation and in the scientific literature.

Chapter 3, *Electromagnetic Wave Guidance in Lossy Thin Films*, derives the full-field solution for wave guidance in a generic dielectric slab. This chapter is unique in that the solution also includes the effects of loss within each dielectric layer. Lossy waveguides are very frequently ignored throughout the scientific literature, even though such structures serve as highly descriptive models for thin-film photovoltaic devices.

Chapter 4, *Enhanced Light Absorption from Embedded Dielectric Nanoparticles*, explores the effects of light scattering by dielectric spheres placed directly underneath an ARC. It is shown that such designs can enhance light absorption within the active absorber layer without disrupting the light-injection properties of the ARC. These designs are also compared against plasmonic nanoparticles placed along the surface of the device, which do not cooperate well with the ARC.

Chapter 5, *Design Principles for Light-Trapping in Thin Silicon Films with Embedded Dielectric Nanoparticles*, expounds on the previous chapter by including the effects of a back contact in the device. The question of ideal size and placement of the embedded dielectric

spheres is explored in great detail, with several discussions on the underlying physics which dominate the net absorption within the active layer.

Chapter 6, *Embedded Dielectric Nanoparticles Versus Surface Texturing*, compares the absorption gains due to two light trapping mechanisms. The question of embedded spheres versus surface texture arose from the work of Nunomura, et al [30], which demonstrated a 17 % absorption gain from embedded SiO_2 spheres within a silicon solar cell. However, by embedding the spheres into the active semiconductor layer, the solar cells were also roughened along the surface. This chapter therefore answers the question of which effect dominates the overall absorption gain: Embedded dielectric nanospheres or surface roughening.

Chapter 7, *Conclusion*, reviews the main findings of this research and discusses opportunities for further investigation in the future.

CHAPTER 2

ELECTROMAGNETIC FUNDAMENTALS FOR PHOTOVOLTAIC MODELING

Because most photovoltaic devices are constructed through the deposition of various materials into a layered structure, it is important to understand the physics of light propagation through a planar, stratified medium. Such models can be described entirely through analytical expressions, thereby making them ideal benchmarks from which to model designs and validate simulation results. These simple structures can also serve as the references against which to define the absorption gain of various light-trapping schemes. The first part of this chapter will therefore present a theoretical overview of electromagnetic wave propagation in a layered, dielectric structure excited by an external plane wave source.

For the second part of this chapter, we shall introduce the concepts of optical path length and path-length enhancement. These ideas are frequently referenced throughout the light-trapping literature, especially in the context of the ergodic limit for light absorption. It is therefore important for the student of light-trapping to appreciate these ideas on a rigorous, theoretical level.

Finally, it should be emphasized that light absorption is only the first step in a long chain of physical events that must occur in order to produce a functional photovoltaic cell. Once a photon has been captured by the absorbing layer, the resultant electron-hole pair undergoes an elaborate dance of particle diffusion before work is eventually extracted from the device. However, without that initial captured photon, none of those other steps can ever occur. An understanding of electromagnetic theory is therefore fundamental to the proper design of an efficient solar cell, and the focus of this dissertation is limited almost exclusively to the physics of photon propagation and absorption. For a comprehensive introduction to the physical events that drive a photovoltaic device after the capture of a photon, the reader is referred to [31] as an excellent source for such details.

2.1 Plane Wave Propagation in Stratified Media

The physical system of interest throughout this chapter will be the stratified medium depicted in Figure 2.1. Our model consists of M planar dielectric regions excited by a plane wave source from Region 1. The incident plane wave is defined by a characteristic frequency of excitation f, but in practice it is common to use an equivalent free-space wavelength $\lambda_0 = c/f$, with c being the speed of light in a vacuum. The incident wave is also defined by an arbitrary angle of incidence θ with respect to the z-axis. Finally, two possible polarization states exist for the incident field intensity. Under transverse-electric (TE) polarization, the incident electric field $\mathbf{E}$ is assumed to be y-polarized. For transverse-magnetic (TM) polarization, it is the magnetic field $\mathbf{H}$ that is assumed to be y-polarized.

Each region in the model is filled with a linear, isotropic medium, defined by a complex index of refraction:

$$\tilde{n}_i = n_i + j\kappa_i \ , \tag{2.1}$$

where n_i is the real index of refraction and κ_i is the extinction coefficient. Region 1 and Region M are infinite half-spaces, with the boundaries between each layer placed at the points d_1 through d_{M-1}. Inside each region is a forward- and reverse-propagating plane wave with amplitude A_i and B_i, respectively. The incident field amplitude A_1 is a known value that is usually normalized to unit intensity. For TE polarization, this implies $A_1 = 1.0$ V/m (electric field intensity), while for TM polarization we have $A_1 = 1.0$ A/m (magnetic field intensity). We shall also assume that there is no reverse-propagating wave in Region M,

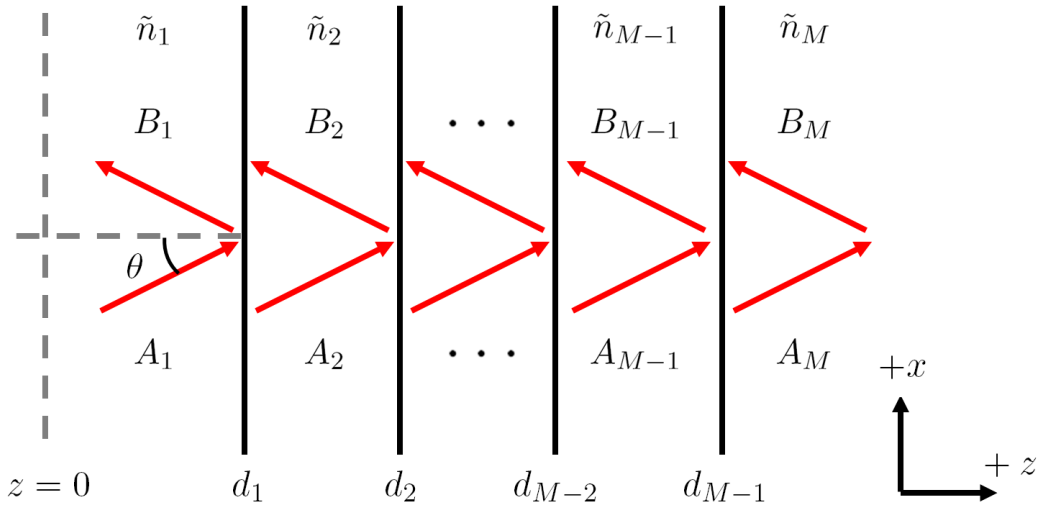

Figure 2.1. A stratified medium is excited by a plane wave from the left.

thereby setting $B_M = 0$. Using these given parameters, it is our goal to solve for all the field amplitudes throughout the system.

A comprehensive solution to this model can be found in many standard references, and the following derivation is based largely on the information found in [32]. However, this discussion also includes many practical aspects of a stable numerical implementation that are difficult to find in the standard literature. For simplicity, we shall also assume that each region is nonmagnetic, since such materials rarely show up in photovoltaic systems. We may therefore set the relative permeability of each region to $\mu_r = 1$.

Finally, this dissertation adheres to the convention of a time-dependent phasor notation with the form of $\mathrm{Re}\{e^{kx}e^{-\omega t}\}$. This is consistent with the majority of the optics literature, but contrary to much of the RF and microwave literature. It also means that a positive value for the extinction coefficient κ implies a lossy material rather than a gain material. When calculating the time derivative of a phasor, we may further make the substitution $\partial/\partial t = -j\omega$.

2.1.1 TE Polarization

We begin with the case of TE polarization by expressing the forward-propagating wave in Region 1. Using phasor notation, this is written as

$$\mathbf{E}_1^+(x,z) = \hat{\mathbf{y}} A_1 e^{j(k_{1x}x + k_{1z}z)} \ . \tag{2.2}$$

The parameters k_{1x} and k_{1z} denote the x- and z-components to the wavevector in Region 1. If we define the free-space wavenumber using $k_0 = 2\pi/\lambda_0$, then the wavevector components must satisfy the *dispersion relation* given by

$$k_{1x}^2 + k_{1z}^2 = k_1^2 \ , \tag{2.3}$$

where $k_1 = k_0\tilde{n}_1$ is the wavenumber in Region 1. The wavenumber components are then related to the angle of incidence by

$$k_{1z} = k_0\tilde{n}_1 \cos\theta \ , \tag{2.4}$$

$$k_{1x} = k_0\tilde{n}_1 \sin\theta \ . \tag{2.5}$$

We now write out the expression for the reflected wave in Region 1 as

$$\mathbf{E}_1^-(x,z) = \hat{\mathbf{y}} B_1 e^{j(k_{1x}x - k_{1z}z)} \ . \tag{2.6}$$

Combining this with the forward propagating wave then gives us the total electric field for Region 1:

$$\begin{aligned}\mathbf{E}_1(x,z) &= \hat{\mathbf{y}}A_1 e^{j(k_{1x}x+k_{1z}z)} + \hat{\mathbf{y}}B_1 e^{j(k_{1x}x-k_{1z}z)} \ , \\ &= \hat{\mathbf{y}}\left(A_1 e^{+jk_{1z}z} + B_1 e^{-jk_{1z}z}\right) e^{jk_{1x}x} \ . \end{aligned} \tag{2.7}$$

Likewise, for any arbitrary region throughout the system, we can also write

$$\mathbf{E}_i(x,z) = \hat{\mathbf{y}}\left(A_i e^{+jk_{iz}z} + B_i e^{-jk_{iz}z}\right) e^{jk_{ix}x} \ . \tag{2.8}$$

The next step is to solve for the wavenumber components throughout each region. This is accomplished by enforcing the *phase-matching condition*, which simply states that all tangential wavevector components must be continuous across planar boundaries. The result of this condition is that $k_{ix} = k_{1x}$ for all layers, thereby allowing us to drop the subscript dependence on k_x. The total field in Region i therefore satisfies

$$\mathbf{E}_i(x,z) = \hat{\mathbf{y}}\left(A_i e^{+jk_{iz}z} + B_i e^{-jk_{iz}z}\right) e^{jk_x x} \ . \tag{2.9}$$

Finally, we can also solve for each k_{iz} component by applying the dispersion relation for each respective region:

$$k_{iz} = \sqrt{k_i^2 - k_x^2} = \sqrt{k_0^2\tilde{n}_i^2 - k_x^2} \ . \tag{2.10}$$

Before continuing with the derivation, it is worth noting a practical issue of numerical stability. Although Equation (2.9) is a perfectly valid expression, it is also computationally unstable for materials with complex indices. The reason for this is because the phase on each plane wave is referenced with respect to $z = 0$. For a purely lossless system, this is normally not a problem and the computations are numerically stable. However, in the presence of gain or loss, there exists a magnitude disparity between the amplitude coefficients (A_i and B_i) and their complex exponential partners ($e^{+jk_{iz}}$ and $e^{-jk_{iz}}$). Numerically speaking, this can result in a multiplication between an extremely large number and an extremely small number. When the disparity stretches across enough orders of magnitude, accurate computation becomes impossible for a machine with finite digital precision.

To avoid the instabilities of numerical computation, it is helpful to re-express Equation (2.9) by referencing the complex exponentials with respect to their plane of injection (i.e., the plane at the tail of each wavevector in Figure 2.1). This is accomplished by writing

$$\mathbf{E}_i(x,z) = \hat{\mathbf{y}}\left(A_i e^{+jk_{iz}(z-d_{i-1})} + B_i e^{-jk_{iz}(z-d_i)}\right) e^{jk_x x} \ . \tag{2.11}$$

The point defined by d_0 is arbitrary since the incident field A_1 is already given by the model and Region 1 is assumed to be lossless. Similarly, the point d_M is also arbitrary since

the assumption $B_M = 0$ negates the effect of any choice we might use. This small change in reference greatly improves the numerical stability of the model, thereby allowing us to generate a practical solution.

Now that we have determined the component wavenumbers in each region, the next step is to solve for the rest of the field amplitudes throughout the system. This is accomplished by defining the magnetic field intensities in each region and then enforcing continuity of the tangential field components. We therefore begin with Faraday's law, which states that

$$\nabla \times \mathbf{E} = -\frac{\partial \mathbf{B}}{\partial t} = j\omega\mu_0 \mathbf{H} \ . \tag{2.12}$$

Carrying out the curl operation within the ith region and solving for $\mathbf{H}_i$ then leads to

$$\begin{aligned} \mathbf{H}_i(x,z) = \quad & \hat{\mathbf{z}} \frac{k_x}{\omega\mu_0} \left(+A_i e^{+jk_{iz}(z-d_{i-1})} + B_i e^{-jk_{iz}(z-d_i)} \right) e^{jk_x x} \\ & + \hat{\mathbf{x}} \frac{k_{iz}}{\omega\mu_0} \left(-A_i e^{+jk_{iz}(z-d_{i-1})} + B_i e^{-jk_{iz}(z-d_i)} \right) e^{jk_x x} \ . \end{aligned} \tag{2.13}$$

The next step is to enforce continuity along the tangential field components at each planar boundary. For a given boundary at $z = d_i$, continuity on the electric field requires

$$a_i A_i + B_i = A_{i+1} + b_i B_{i+1} \ , \tag{2.14}$$

where, for notational compactness, the coefficients a_i and b_i are defined as

$$a_i = e^{+jk_{iz}(d_i - d_{i-1})} \ , \tag{2.15}$$

$$b_i = e^{-jk_{(i+1)z}(d_i - d_{i+1})} \ . \tag{2.16}$$

Note how a_i simply denotes the phase and amplitude change in a wave that exits the boundary at $z = d_{i-1}$ and propagates to d_i. The same is true for b_i, except for the reverse-propagating wave from d_{i+1} to d_i. If we likewise enforce continuity on the x-component to the magnetic field, we find

$$-a_i k_{iz} A_i + k_{iz} B_i = -k_{(i+1)z} A_{i+1} + b_i k_{(i+1)z} B_{i+1} \ . \tag{2.17}$$

Our goal now is to derive an expression for B_i/A_i. This process begins by first solving for $a_i A_i$ in Equation (2.14) and B_i in Equation (2.17):

$$a_i A_i = A_{i+1} + b_i B_{i+1} - B_i \ , \tag{2.18}$$

$$B_i = \frac{k_{(i+1)z}}{k_{iz}} \left(-A_{i+1} + b_i B_{i+1} \right) + a_i A_i \ . \tag{2.19}$$

Cross-substitution between these two equations then leads to

$$A_i = \frac{1}{2a_i}\left(1+\frac{k_{(i+1)z}}{k_{iz}}\right)A_{i+1} + \frac{1}{2a_i}\left(1-\frac{k_{(i+1)z}}{k_{iz}}\right)B_{i+1}b_i \ , \tag{2.20}$$

$$B_i = \frac{1}{2}\left(1-\frac{k_{(i+1)z}}{k_{iz}}\right)A_{i+1} + \frac{1}{2}\left(1+\frac{k_{(i+1)z}}{k_{iz}}\right)B_{i+1}b_i \ . \tag{2.21}$$

Finally, divide these two expressions and simplify to arrive at

$$\frac{B_i}{A_i} = a_i \frac{\left(k_{iz}-k_{(i+1)z}\right)+b_i\left(k_{iz}+k_{(i+1)z}\right)\frac{B_{i+1}}{A_{i+1}}}{\left(k_{iz}+k_{(i+1)z}\right)+b_i\left(k_{iz}-k_{(i+1)z}\right)\frac{B_{i+1}}{A_{i+1}}} \ . \tag{2.22}$$

The utility of this expression is that it provides a recursive relation between B_i/A_i and B_{i+1}/A_{i+1}. Since $B_M = 0$, the recursion terminates at $i = M$ under the condition $B_M/A_M = 0$. Equation (2.22) therefore provides a numerical algorithm for computing B_1/A_1. This algorithm is numerically stable for any combination of passive materials throughout the system, thus providing a reliable scheme for obtaining B_1. One only needs to exercise caution in the presence of gain materials within the system, which tend to numerically destabilize the calculations as a_i and b_i become excessively large.

Once B_1 is a known quantity, it can then be used to progressively solve for the rest of the wave amplitudes throughout the layers. To see how, consider the boundary at $z = d_1$. Assume also that A_i and B_i are now known values, which is certainly true for the $i = 1$ boundary. From basic theory of electromagnetic propagation between planar boundaries, we can now write

$$B_i = \Gamma_{i(i+1)}A_i a_i + \tau_{(i+1)i}B_{i+1}b_i \ , \tag{2.23}$$

where $\Gamma_{i(i+1)}$ and $\tau_{(i+1)i}$ are the Fresnel reflection coefficients. For the case of TE polarization, these are given by

$$\Gamma_{i(i+1)} = \frac{k_{iz}-k_{(i+1)z}}{k_{iz}+k_{(i+1)z}} \ , \tag{2.24}$$

$$\tau_{(i+1)i} = 1+\Gamma_{(i+1)i} \ . \tag{2.25}$$

In other words, the reverse-propagating wave amplitude B_i at the ith boundary is determined by the reflected wave from Region i and the transmitted wave that propagates backward through Region $i+1$. We may therefore solve for B_{i+1} to arrive at

$$B_{i+1} = \frac{B_i - \Gamma_{i(i+1)}A_i a_i}{\tau_{(i+1)i}b_i} \ . \tag{2.26}$$

Finally, by a similar argument, we can also formulate the relation

$$A_{i+1} = \tau_{i(i+1)}A_i a_i + \Gamma_{(i+1)i}B_{i+1}b_i \ , \tag{2.27}$$

where again, the Fresnel coefficients are defined in a similar manner.

Together, Equations (2.26) and (2.27) provide an exact solution for the rest of the wave amplitudes throughout the system. The algorithm begins with Region 1 and iterates from left to right until reaching Region M. The solution then terminates with $B_M = 0$, ending with a complete, full-field solution for all wave amplitudes throughout the entire stratified medium. The advantage to this specific approach is again a matter of numerical stability. For regions with very high loss, the b_i term will take on a very small value and cause instability if Equation (2.26) is directly applied. Consequently, for very lossy regions, one may simply assume that $B_{i+1} = 0$ and then terminate the iterations after solving for A_{i+1}. In essence, all this says is that highly lossy materials do not experience any significant reflections due to the back-and-forth propagation of waves beyond the initial boundary. A good cutoff point is $a_i < 10^{-9}$, which provides good accuracy for most desktop computers without introducing any significant numerical error.

Finally, it should be emphasized that this method is only accurate for an arbitrary combination of strictly passive layers. If the stratified medium contains a mixture of lossy and amplifying media, then numerical implementation becomes an intrinsically unstable procedure. The reason for this is the huge disparity of wave amplitudes that develop across several orders of magnitude within each layer. Because these must be numerically calculated with finite precision, accurate results may be impossible to achieve under extreme conditions. Fortunately, photovoltaic devices are almost exclusively comprised of passive layers, thereby guaranteeing accurate computations with this method.

2.1.2 TM Polarization

We now turn our attention to the case of TM polarization. By analogy with the previous section, the magnetic field in an arbitrary layer is expressed as

$$\mathbf{H}_i(x,z) = \hat{\mathbf{y}} \left(A_i e^{+jk_{iz}(z-d_{i-1})} + B_i e^{-jk_{iz}(z-d_i)} \right) e^{jk_x x} \ . \tag{2.28}$$

The electric field function is then determined from Ampere's law, given as

$$\nabla \times \mathbf{H} = \frac{\partial \mathbf{D}}{\partial t} = -j\omega\tilde{n}^2\epsilon_0\mathbf{E} \ . \tag{2.29}$$

After solving for $\mathbf{E}_i$ in Region i, we then have

$$\begin{aligned} \mathbf{E}_i(x,z) = &-\hat{\mathbf{z}}\frac{k_x}{\omega\tilde{n}_i^2\epsilon_0} \left(+A_i e^{+jk_{iz}(z-d_{i-1})} + B_i e^{-jk_{iz}(z-d_i)} \right) e^{jk_x x} \\ &+ \hat{\mathbf{x}}\frac{k_{iz}}{\omega\tilde{n}_i^2\epsilon_0} \left(+A_i e^{+jk_{iz}(z-d_{i-1})} - B_i e^{-jk_{iz}(z-d_i)} \right) e^{jk_x x} \ . \end{aligned} \tag{2.30}$$

We are now ready to enforce continuity on the tangential field components at the $z = d_i$ boundary. Just like the TE case, the result is two coupled equations of the form

$$a_i A_i + B_i = A_{i+1} + b_i B_{i+1} \ , \tag{2.31}$$

$$\frac{k_{iz}}{\tilde{n}_i^2}\left(a_i A_i - B_i\right) = \frac{k_{(i+1)z}}{\tilde{n}_{i+1}^2}\left(A_{i+1} - b_i B_{i_1}\right) \ , \tag{2.32}$$

with the a_i and b_i terms defined by the same convention as before. Combining these two expressions and simplifying then leads to another recursion equation with the form

$$\frac{B_i}{A_i} = a_i \frac{\left(k_{iz}\tilde{n}_{i+1}^2 - k_{(i+1)z}\tilde{n}_i^2\right) + b_i\left(k_{iz}\tilde{n}_{i+1}^2 + k_{(i+1)z}\tilde{n}_i^2\right)\frac{B_{i+1}}{A_{i+1}}}{\left(k_{iz}\tilde{n}_{i+1}^2 + k_{(i+1)z}\tilde{n}_i^2\right) + b_i\left(k_{iz}\tilde{n}_{i+1}^2 - k_{(i+1)z}\tilde{n}_i^2\right)\frac{B_{i+1}}{A_{i+1}}} \ . \tag{2.33}$$

With B_1 a known value, we can again solve for the rest of the wave amplitudes using Equations (2.26) and (2.27). The only change is in the Fresnel coefficients, which now take on the form of

$$\Gamma'_{i(i+1)} = \frac{k_{iz}\tilde{n}_{i+1}^2 - k_{(i+1)z}\tilde{n}_i^2}{k_{iz}\tilde{n}_{i+1}^2 + k_{(i+1)z}\tilde{n}_i^2} \ , \tag{2.34}$$

$$\tau'_{(i+1)i} = 1 + \Gamma'_{(i+1)i} \ , \tag{2.35}$$

where the prime notation indicates the reflection and transmission coefficients of the magnetic field amplitudes. Taken together, these expressions provide us with a complete, full-field solution to the problem of plane wave excitation on a stratified medium. The solution is numerically stable under any combination of passive materials, incident angle, and wave polarization.

Figure 2.2 demonstrates this algorithm by calculating the full-field solution to a plane wave exciting a simplified solar cell model. The incident plane wave has a free-space wavelength of $\lambda_0 = 600$ nm and an angle of incidence $\theta = 30°$. The model layers are given by air ($\tilde{n}_1 = 1$), an 80 nm coating made of Si_3N_4 ($\tilde{n}_2 = 2.0$), a 1.0 μm film of c-Si ($\tilde{n}_3 = 3.95 + j0.03$), and an aluminum back contact ($\tilde{n}_4 = 1.2 + j7.0$). The planar boundaries are indicated by the vertical bars. Figure 2.2(a) shows the TE (electric) field profile, while Figure 2.2(b) shows the TM (magnetic) field profile.

2.2 Antireflective Coatings

One of the more common tools we shall be referencing throughout this work is the antireflective coating (ARC). As its name implies, the ARC consists of a thin coating at the surface of a solar cell that minimizes reflection. To understand the basic principles of the ARC, we first solve for the reflection coefficient a simple three-layer system as shown

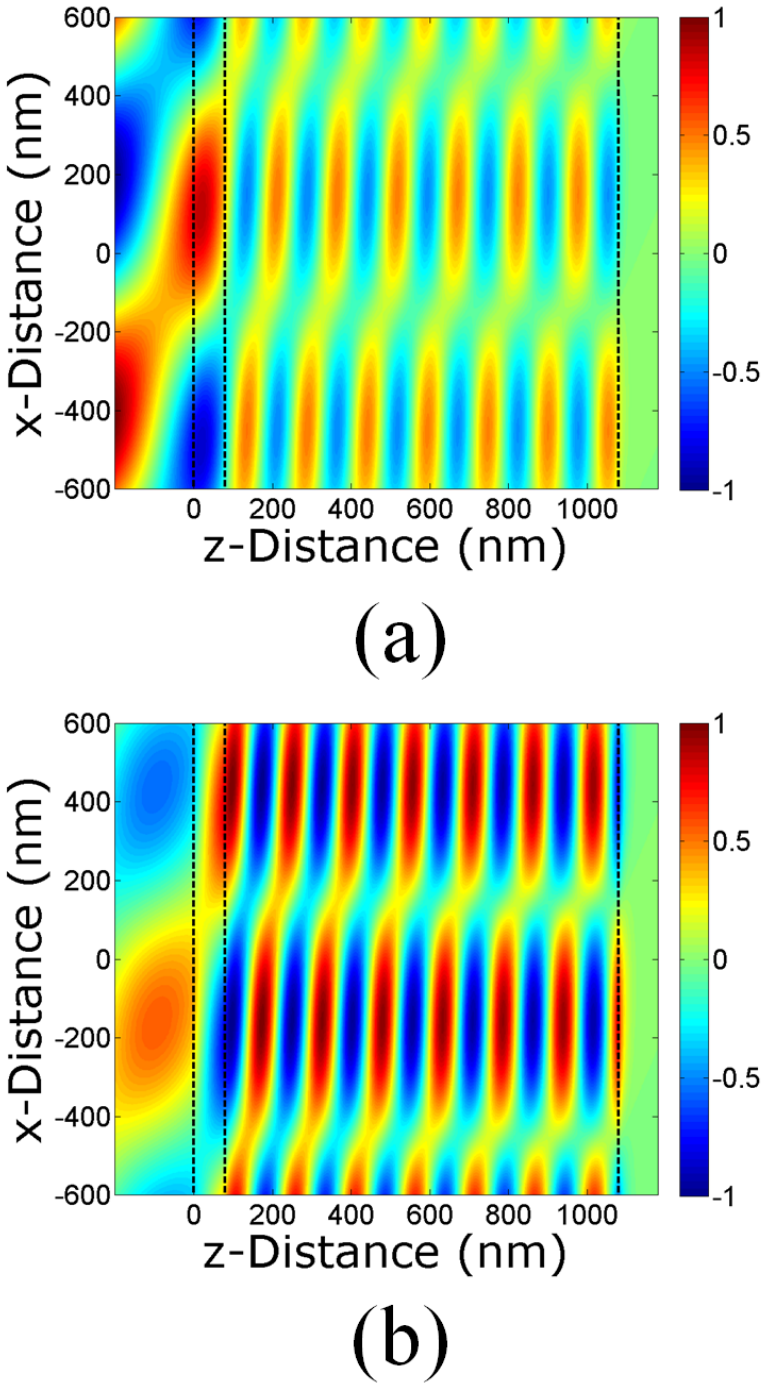

Figure 2.2. A stratified medium is excited by a plane wave with $\lambda_0 = 600$ nm and $\theta = 30°$. Region 1 is air ($\tilde{n}_1 = 1$), Region 2 is an 80 nm nitride coating ($\tilde{n}_2 = 2.0$), Region 3 is a 1.0 μm film of c-Si ($\tilde{n}_3 = 3.95 + j0.03$), and the back contact is aluminum ($\tilde{n}_4 = 1.2 + j7.0$). (a) TE electric field profile $E_y(x, z)$ in units of V/m. (b) TM magnetic field profile $H_y(x, z)$ in units of A/m. Vertical bars indicate planar boundaries.

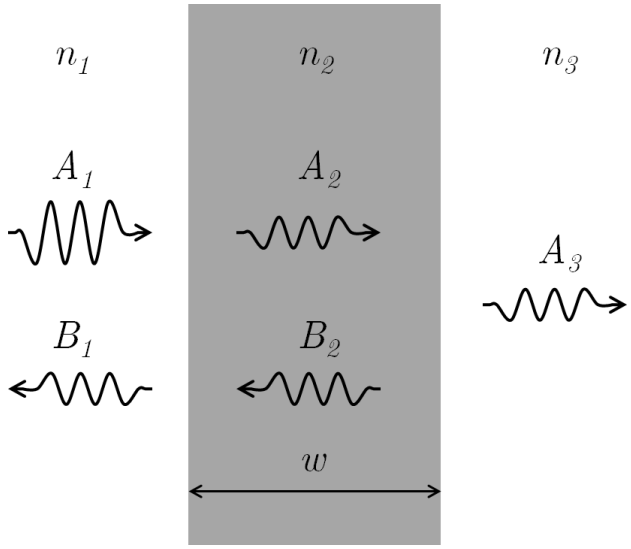

Figure 2.3. Three-layer dielectric model illustrating the principle of the antireflective coating (ARC).

in Figure 2.3. Without any loss of generality, we may assume that all three regions are lossless. Using Equation (2.26), it is then straightforward to show that the reflectance R satisfies

$$R = \left|\frac{B_1}{A_1}\right|^2 = \left|\frac{\Gamma_{12} + \Gamma_{23}e^{2j\beta_2 w}}{1 + \Gamma_{12}\Gamma_{23}e^{2j\beta_2 w}}\right|^2 , \tag{2.36}$$

Note that k_2 has been substituted with $k_2 = \beta_2$ to emphasize the purely real value of the wavenumber. The goal of the ARC is to specify the necessary physical conditions such that $R = 0$.

One of the simplest types of ARC is called the *quarter-wave transformer*. This situation occurs when the intermediate region has an electrical length of $\beta_2 w = \pi/4$, or $w = \lambda/4n_2$. This forces the complex exponential in Equation (2.36) to assume a value of $\exp(2j\beta_2 w) = -1$. Setting $R = 0$ then leads us to the condition that

$$\Gamma_{12} = \Gamma_{23} . \tag{2.37}$$

If we limit ourselves to normal incidence, this simplifies into

$$\frac{n_1 - n_2}{n_1 + n_2} = \frac{n_2 - n_3}{n_2 + n_3} . \tag{2.38}$$

Finally, solving for n_2 yields the antireflectance condition

$$n_2 = \sqrt{n_1 n_3} . \tag{2.39}$$

For the case of silicon-based solar cells, the target region will generally possess a real index of refraction around n_3 =3.5–4.0 for wavelengths near the peak of the solar spectrum.

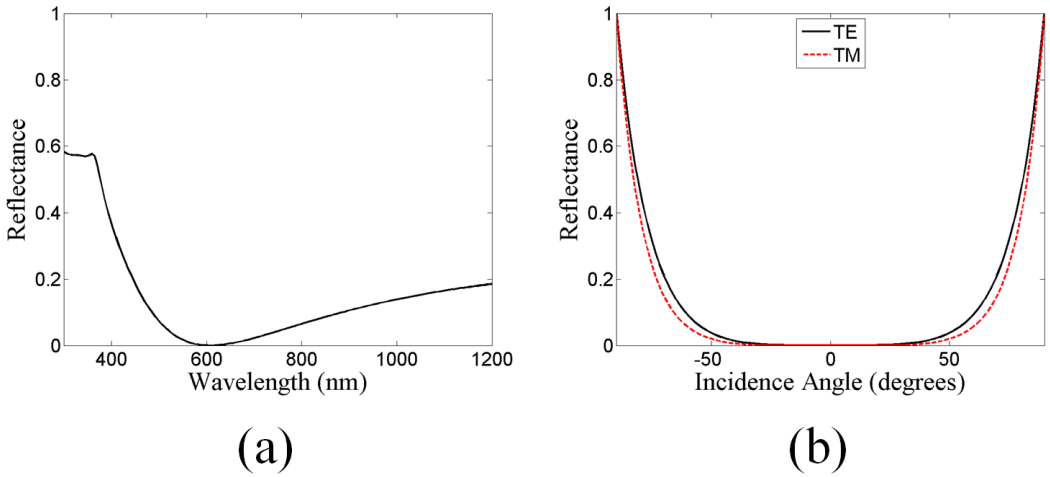

Figure 2.4. Reflectance curves for a 75 nm coating of Si_3N_4 placed atop an infinite half-space of c-Si. (a) Reflectance at normal incidence as a function of wavelength. (b) Reflectance at $\lambda = 600$ nm as a function of incidence angle.

The ideal ARC should therefore possess a real index value around n_2 =1.8–2. One example compound which satisfies these conditions is silicon nitride (Si_3N_4), thus making it a very popular choice for simple ARCs. For example, a thickness of $w = 75$ nm at a wavelength of $\lambda = 600$ nm will reduce reflections to as little as $R = 4.5 \times 10^{-4}$. In practice, however, this cannot hold over all wavelengths, incidence angles, and polarizations, so it is important to quantify performance under varying conditions. Figure 2.4 therefore plots the reflectance curves for a 75 nm ARC composed of Si_3N_4 placed atop an infinite half-space of crystalline silicon (c-Si). The optical constants for each material are summarized in Appendix A. Clearly, the simple nitride ARC performs relatively well, though not necessarily perfectly. Although it is possible to achieve even greater performance through the use of multi-layered ARC's and graded indices [33], cost and complexity generally limit the practical application of such structures.

2.3 Optical Path Length and Path Length Enhancement

The concept of optical path length enhancement is a useful tool for characterizing the effects of light-trapping in thin films. The underlying principle is reasonably straightforward on its own, but is frequently referenced in passing throughout the optics literature without a firm theoretical foundation. Some varied sources have attempted to fill this void in the literature [13], but a comprehensive discussion on the topic is difficult to find. This next section is therefore devoted to providing a thorough introduction to the principle of

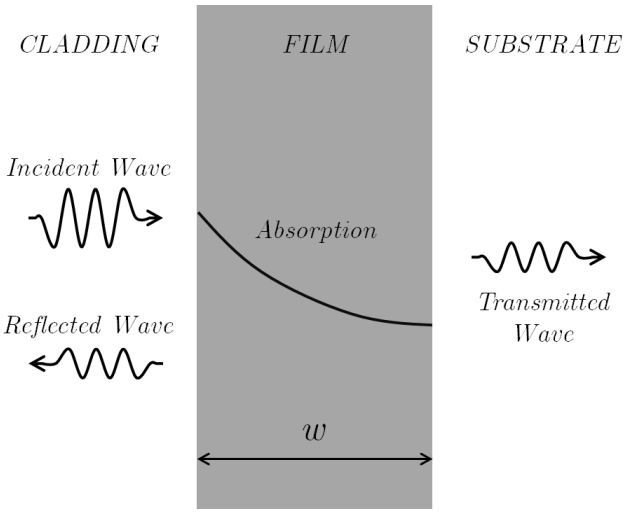

Figure 2.5. A thin dielectric slab of thickness w is embedded between two dielectric half-spaces. An incident plane wave strikes the system from the left. Some power is reflected back toward the source and some exits into the substrate.

optical path length and then exploring the consequences of such analysis from a photovoltaic perspective.

2.3.1 The Model-N Slab

The fundamental definition for optical path length can be understood by imagining a thin dielectric slab with thickness w, as shown in Figure 2.5. The incident medium, also referred to as the *cladding*, is generally assumed to be air ($\tilde{n}_1 = \tilde{n}_c = 1$), but can also be any arbitrary lossless dielectric medium. The slab region is often referred to as the *film*, and is defined by some complex index $\tilde{n}_f = n_2 + j\kappa_2$. The third region is usually referred to as either the back contact, or the *substrate*, and is defined by the complex index $\tilde{n}_s = n_3 + j\kappa_3$.

If an electromagnetic plane wave strikes the film region from the left, the incident power flow can be divided among three possible outcomes. Some of that power will reflect back into the cladding region, some will transmit into the substrate, and the rest will be absorbed within the film. If the incident wave is normalized to unit intensity, then this naturally leads to

$$1 = R + T + A \ , \tag{2.40}$$

where R is called the *reflectance*, T is called the *transmittance*, and A is called the *absorption factor*.

A special case of this scenario can be imagined by neglecting the effects of any reflections at each planar boundary. Such a system is referred to as *model-N* because it exhibits "no"

light trapping and "no" reflections [13]. In such a model, the incident light experiences a single pass through the film region and then propagates directly into the substrate. However, because the film region is lossy, the incident wave also experiences some finite amount of exponential decay. For the case of normal incidence ($\theta = 0$), the transmittance naturally satisfies

$$T = e^{-2\alpha_2 w} \ , \tag{2.41}$$

where $\alpha_2 = 2\pi\kappa_2/\lambda_0$ is the attenuation coefficient of the film. In practice, the film region is the only lossy region that is relevant for path-length analysis, so the subscript index on α can be dropped for the rest of this discussion. Furthermore, because there are no reflections, we can note that $R = 0$ and

$$A = 1 - e^{-2\alpha w} \ . \tag{2.42}$$

Finally, we can use this expression to solve for the thickness of a model-N slab:

$$w = -\frac{1}{2\alpha} \ln(1 - A) \ . \tag{2.43}$$

The usefulness of Equation (2.43) is that the film thickness w depends only on the absorption factor A and the attenuation coefficient α. This means that *any* arbitrary planar system with these specific parameters may be described entirely in terms of some equivalent model-N slab with the appropriate thickness. This allows us to define the *equivalent path length* (EPL) of a lossy film as

$$\ell = -\frac{1}{2\alpha} \ln(1 - A) \ . \tag{2.44}$$

Using Equation (2.44), the ability of any lossy dielectric film to absorb incident light may be intuitively expressed in terms of a simple geometric length. The length itself has no physical meaning other than to serve as an abstraction of whatever complex light-trapping mechanisms may exist within the cell. This distinguishes ℓ from the physical thickness w, since ℓ can take on a wide range of values that vary with such features as wavelength or incidence angle, while w is a fixed physical parameter.

A classical benchmark of EPL is the *ergodic limit* introduced by Yablonovitch and Cody in 1982 [21]. As discussed in Chapter 1, this limit occurs when the film region is low loss and when each surface is a Lambertian scatterer. In such a scenario, it can be shown that the EPL of the system is $\ell = 4n_2^2 w$. For the case of c-Si, $n_2 \approx 3.5$ over much of the near-infrared spectrum ($\lambda > 800$ nm). This means that Lambertian scattering can effectively multiply the thickness of a thin c-Si film by as much as 50 times! The ergodic limit is therefore a commonly referenced benchmark in the light-trapping literature, with many studies attempting to reach or even exceed this value [23].

Another useful metric for characterizing optical systems is called the *path-length enhancement* (PLE). For example, roughened surface texturing is a common tool for injecting extra light into a solar cell and then scattering it throughout the interior [25]. Such a design will naturally absorb more light than a strictly planar geometry, thereby indicating some sort of path-length advantage within the film. If we then define ℓ_0 as the EPL of some reference and ℓ_x as the EPL of the experimental design, then the PLE may be simply defined as

$$\text{PLE} = \frac{\ell_x}{\ell_0} \ . \tag{2.45}$$

In practice, it is common to use the model-N cell as a reference for measuring PLE. For example, the PLE of an ergodic cell is commonly referred to as the "$4n^2$" limit. However, one must be careful about utilizing this metric when describing light-trapping behavior. As we shall demonstrate later on, even a system with no internal light-scattering can still lead to a PLE value greater than unity when using the model-N reference.

2.4 Transmittance and Absorption Factor

Consider again the three-layer diagram depicted in Figure 2.5. Using Equation (2.26), it is straightforward to show that the reflectance R satisfies

$$R = \left| \frac{\Gamma_{12} + \Gamma_{23} e^{2jk_2 w}}{1 + \Gamma_{12}\Gamma_{23} e^{2jk_2 w}} \right|^2 \ . \tag{2.46}$$

To find the transmittance T, we first need to know the forward-propagating amplitude in the substrate region. Following the iterative solution, this is found to be

$$A_3 = \tau_{23} \left[\tau_{12} + \frac{\Gamma_{21}}{\tau_{21}} \left(B_1 - \Gamma_{12} \right) \right] e^{+jk_2 w} \ . \tag{2.47}$$

Next, we note that the power density of the transmitted wave satisfies

$$S_3 = \frac{1}{2} \left| A_3 \right|^2 n_s \ . \tag{2.48}$$

The transmittance is then defined as $T = S_3 / S_1$, leading us to

$$T = \left| A_3 \right|^2 \frac{n_s}{n_c} \ . \tag{2.49}$$

At first glance, it is tempting to suppose that minimizing T is a valid first-step toward maximizing the absorption factor of a solar cell. For example, such effort has been the motivation behind the use of a distributed Bragg reflector placed at the rear of the solar cell rather than simple aluminum contacts [26]. Unfortunately, due to the strong phase dependence of wave propagation in such systems, decreases in T are not always guaranteed

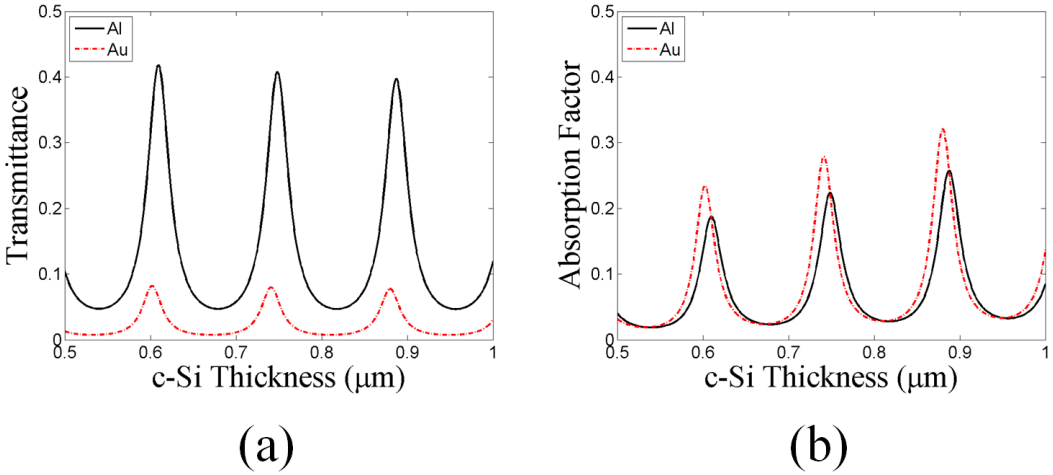

Figure 2.6. Transmittance (a) and absorption factor (b) of a silicon slab at wavelength $\lambda_0 = 1.0\ \mu$m. The rear contact is either aluminum (solid line) or gold (dashed line). The gold contact clearly lowers the overall transmittance, but is not always guaranteed to produce a higher absorption factor.

to result in higher values for A. As an example, consider the absorption in a thin layer of c-Si with an aluminum (Al) back-contact at a wavelength of $\lambda_0 = 1.0\ \mu$m. Such a system may be reasonably modeled by the indices of refraction given by

$$\begin{aligned} \text{Air:} \quad & \tilde{n}_c = 1 \ , \\ \text{c-Si:} \quad & \tilde{n}_f = 3.6 + 0.005j \ , \\ \text{Al:} \quad & \tilde{n}_s = 1.3 + 9.6j \ . \end{aligned}$$

The response of this system is depicted in Figure 2.6, which plots T and A as a function of varying slab thickness w. The peaks and valleys are characteristic of Fabry-Perot resonances which occur as the reflectivity rises and falls with the varying phase alignments of the internally-bouncing waves.

For comparison, let us now replace the Al substrate with gold (Au) by using a complex index of $\tilde{n}'_s = 0.1 + 6.3j$. The response of this model is shown by the red curves in Figure 2.6, where it is readily apparent that transmittance drops significantly across the entire range. Nevertheless, the change in absorption factor is not always for the better. Because of the new phase behavior introduced by the different back contact, the resonance spikes have shifted slightly, thereby leading to a net reduction of absorption along certain thickness for the slab. Though there are certainly other examples where one can readily increase A after decreasing T, the key insight from this demonstration is that reduction in T is not

a mathematical guarantee that A will increase. One should therefore be careful to always ensure that a design change in the rear contact does not inadvertently reduce the overall performance of a solar cell.

2.5 Equivalent Path Length with PEC Substrate

Another useful model worth exploring is the low-loss dielectric with a perfectly conducting rear contact. This greatly simplifies the expressions for R and T while providing useful behavioral insights into the nature of optical path length in thin films. We begin by letting $\kappa_3 \to \infty$ so that $T = 0$ and $\Gamma_{23} = -1$. It is also helpful to separate the wavenumber into real and imaginary components using $k_2 = \beta_2 + j\alpha$. The expression for R then takes on the form

$$R = \left| \frac{\Gamma_{12} - e^{2j\beta_2 w} e^{-2\alpha w}}{1 - \Gamma_{12} e^{2j\beta_2 w} e^{-2\alpha w}} \right|^2 . \tag{2.50}$$

The low-loss approximation for the film region occurs under the condition $\alpha w << 1$ and $\tilde{n}_f \approx n_2$. This also leads to the approximation $\Gamma_{12}^* \approx \Gamma_{12}$. We then note that $|x|^2 = xx^*$ and $e^{jx} + e^{-jx} = 2\cos x$. This allows us to rewrite the reflectance as

$$R = \frac{\Gamma_{12}^2 - 2\Gamma_{12} e^{-2\alpha w} \cos(2\beta_2 w) + e^{-4\alpha w}}{1 - 2\Gamma_{12} e^{-2\alpha w} \cos(2\beta_2 w) + \Gamma_{12}^2 e^{-4\alpha w}} . \tag{2.51}$$

Next, we rewrite the expression for Γ_{12} by defining the *reduced* index of refraction $m = n_2/n_1$ and noting that

$$\Gamma_{12} = \frac{k_0 n_1 - k_0 n_2}{k_0 n_1 + k_0 n_2} = \frac{n_1 - n_2}{n_1 + n_2} = \frac{1 - m}{1 + m} . \tag{2.52}$$

Upon substitution back into R, we finally arrive at

$$R = \frac{(1-m)^2 + 2(1-m)(1+m) e^{-2\alpha w} \cos(2\beta_2 w) + (1+m)^2 e^{-4\alpha w}}{(1+m)^2 + 2(1-m)(1+m) e^{-2\alpha w} \cos(2\beta_2 w) + (1-m)^2 e^{-4\alpha w}} . \tag{2.53}$$

The general behavior of Equation (2.53) is similar to that of a sinusoidal oscillation with an exponentially varying envelope. Our immediate goal is to solve for ℓ under the maximum and minimum conditions, which occur when $\cos(2\beta_2 w) = \pm 1$. Once again, this is the essence of a Fabry-Perot resonator as it maximizes or minimizes reflections under specific phase-matching conditions. We therefore begin with the minimum condition for R, which occurs when $\cos(2k_2 w) = -1$. This corresponds to the maximum value for A and equivalently the maximum value for ℓ. After simplification, we therefore find

$$R = \frac{\left[(1-m) - (m+1) e^{-2\alpha w}\right]^2}{\left[(1+m) - (1-m) e^{-2\alpha w}\right]^2} . \tag{2.54}$$

Next, we recall that $\ell = -\frac{1}{2\alpha} \ln(1 - A)$ and that $1 - A = R$. Solving for ℓ therefore leads to the expression

$$\ell_{max} = -\frac{1}{\alpha} \ln \left[\frac{(1-m) - (1+m) e^{-2\alpha w}}{(1+m) - (1-m) e^{-2\alpha w}} \right] . \tag{2.55}$$

Due to the assumption of a low-loss dielectric, the argument of the natural logarithm is very close to unity. This allows us to approximate $\ln x \approx x - 1$, thus giving

$$\ell_{max} \approx -\frac{1}{\alpha}\left[\frac{(1-m)-(1+m)e^{-2\alpha w}}{(1+m)-(1-m)e^{-2\alpha w}} - 1\right] \ . \tag{2.56}$$

Once again, the low-loss assumption allows us to simplify matters by replacing $e^{-2\alpha w} \approx 1 - 2\alpha w$. After combining the fractions and simplifying, the final result is found to be

$$\ell_{max} \approx 2mw \ . \tag{2.57}$$

Applying the same derivation to the case where $\cos(2k_2 w) = +1$, the minimum path-length is found to be

$$\ell_{min} \approx \frac{2w}{m} \ . \tag{2.58}$$

In practice, the incident medium will nearly always be air or free space, thus allowing us to replace $m = n_2$. In this case, Region 2 is the only dielectric medium in the system and the subscript indices become unnecessary. The limits on EPL for a low-loss dielectric with zero transmittance at normal incidence may therefore be simply expressed as

$$\ell_{max} = 2nw \ , \qquad \text{and} \qquad \ell_{min} = \frac{2w}{n} \ . \tag{2.59}$$

In addition, we can also note that for the case of zero reflection off the front surface (i.e., $m = 1$), the system is effectively model-N with a perfect rear reflector. In this case, the incident wave experiences a single pass once down through the slab and back again, thereby giving an EPL of $\ell_N = 2w$ for the model-N.

As a demonstration, consider a thin slab of silicon at wavelength $\lambda_0 = 1.0$ μm ($\tilde{n}_f = 3.6 + 0.01j$) with a perfect rear reflector. Figure 2.7(a) shows a plot of EPL as a function of varying slab thickness. Superimposed on the plot are the minimum, maximum, and model-N equivalents. Also depicted in Figure 2.7(b) is the absorption factor for a $w = 1.0$ μm slab of crystalline silicon as a function of wavelength across the visible spectrum, using the dielectric data taken from [34].

Several key insights are apparent from these demonstrations. First, the low-loss approximation is only valid when the product αw is very small. For a 1.0 μm film of crystalline silicon, this is true for the region above 600 nm in wavelength. This is an important metric to bear in mind, given that the peak in the AM 1.5 spectrum occurs at approximately 600 nm as well. If the cell were thicker or thinner, the validity of the low-loss assumption would shift in applicable wavelength.

The second insight from this demonstration is the oscillatory nature of the EPL. In effect, it shows that the EPL of any arbitrary system can both exceed and fall short of its model-N

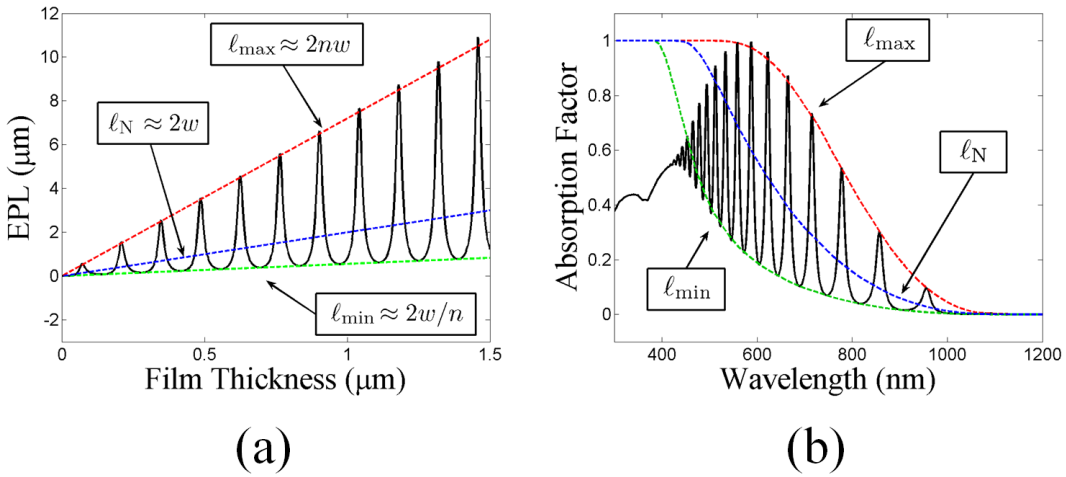

Figure 2.7. (a) EPL of a silicon slab at $\lambda_0 = 1.0$ μm with a perfectly reflecting back contact and varying thickness. (b) Absorption factor of a 1.0 μm slab of silicon as a function of wavelength. Minimum, maximum, and model-N EPLs are all indicated.

value. It is for this reason that the model-N is not necessarily a valid metric against which to measure PLE. Doing so means that any real physical system may experience both gains and losses in PLE, despite the total absence of any lateral coupling into guided modes. Because this renders the concept of PLE somewhat meaningless, it is recommended in this thesis that when measuring the PLE of some given light-trapping scheme, the ideal reference should always be an equivalent design without the specific light-trapping enhancements. This assures a PLE value of unity for any self-referenced design.

2.6 Equivalent Deflection Angle

In this final section, we shall derive another useful parameter for characterizing the relative level of deflection experienced by a wave as it scatters off of any surface features in a solar cell. We begin by considering the effects of off-normal incidence on a low-loss dielectric half-space as shown in Figure 2.8. We are interested in the fraction of incident radiation that is absorbed within the top layer of the half-space with thickness w. From this geometry, it is straightforward to show that the absorption factor satisfies

$$A = t_{12}\left(1 - e^{-2\alpha w'}\right) \ , \tag{2.60}$$

where $t_{12} = |\tau_{12}|^2$ is the *transmissivity* from Region 1 into Region 2. The parameter $w' = 2\sec\theta$ represents a normalized form of equivalent path length of propagation within the slab. If we then solve for θ, it is found that

$$\theta = \sec^{-1}\left[-\frac{1}{2\alpha w}\ln\left(1-\frac{A}{t_{12}}\right)\right] \ . \tag{2.61}$$

The significance of this expression is that it is entirely independent of any incidence angle from Region 1 or even any geometric features atop Region 2. This means that any arbitrary geometric system with an absorption factor A, a transmissivity t_{12}, an attenuation coefficient α, and a thickness of interest w may be expressed in terms of some equivalent propagation angle within Region 2. Thus, by analogy with the concept of EPL, we may define the *equivalent deflection angle* (EDA) as the equivalent angular deflection experienced by an incident plane wave due to the presence of some scattering mechanism.

A demonstration case for calculating EDA is shown in Figure 2.9 by comparing numerical simulation against the analytical solution. Using the finite-difference time-domain (FDTD) method [35], an off-normal plane wave was injected against a dielectric half-space of c-Si with an absorption thickness of $w = 1.0$ μm. Due to the nature of broadband injection with plane waves using FDTD, the angle of incidence unavoidably varies with wavelength and is not a constant value. Fortunately, it is still a known quantity that can be used to calculate θ via Snell's law. The red curve shows the calculation of EDA by applying Equation (2.61) from the simulation output and generally agrees to within $\pm 1^\circ$ of accuracy with the analytical values.

Although the simulation results agree well with the analytical solution, the price of such accuracy is relatively steep. For the simulation results in Figure 2.9, the grid resolution needed to be sampled at a uniform resolution of 1.0 nm. The reason for this is due to the sensitivity of θ with numerical errors in the simulated values for A and t_{12}. From the model in Figure 2.8(a), any errors in A or t_{12} will be interpreted as a deviation in the value for w' and cause an error in θ. To put this in perspective, if w' is off by as little as 1 % from the true value, the resultant trigonometric error for θ can reach as high as 8°. Consequently, special care must be taken to ensure a high degree of numerical accuracy within the simulation. It also means that accurate three-dimensional computation of EDA relatively prohibitive in terms of computational resources, but still reasonable for simple two-dimensional models.

As a demonstration of how EDA may be practically useful, consider the 2D triangular surface texture depicted in Figure 2.10(a). The triangles have a base of 400 nm and height of 141 nm for an angle of 55°. This value is the approximate angle of pyramids bounded by (1,1,1) planes on a (1,0,0) surface in a crystalline silicon lattice, which is a common feature when utilizing chemical etching. Due to their light-trapping and antireflective properties, sub-micron textures of this sort are of special interest for thin-film solar cells [36, 37]. The transmissivity was computed with respect to the boundary between the triangle bases and

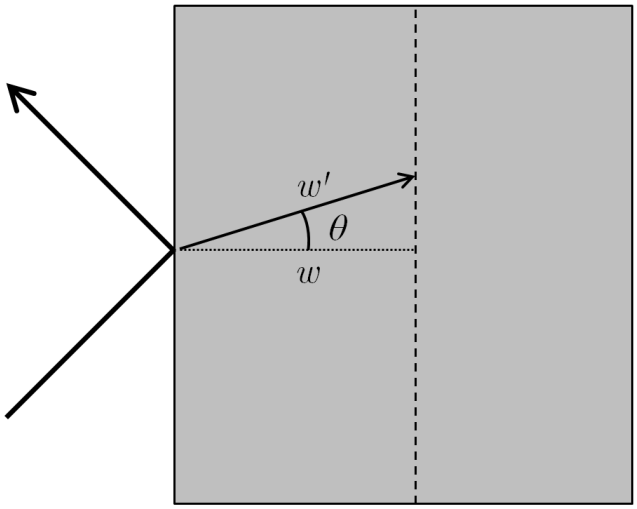

Figure 2.8. Off-normal incidence on a lossy dielectric half-space. The transmitted ray is refracted to an angle θ and partially absorbed within the top w thickness of the dielectric.

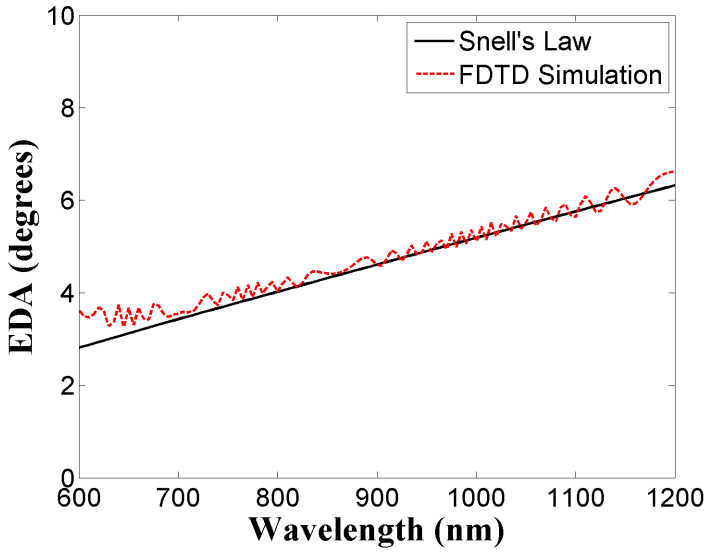

Figure 2.9. Comparison between analytical solution and simulated computation for EDA.

the $z = 0$ plane, thereby limiting our scope to absorption gain within the bulk silicon region. This prevents the extra volume of absorber within the texture itself from influencing the absorption gain calculations.

Figure 2.10(b) shows the computation of EDA from the simulation results using transverse-electric polarization ($\hat{\mathbf{E}} = \hat{\mathbf{z}}$). Below $\lambda_0 = 750$ nm, the EDA tends to fall between 25° - 30°, indicating a strong scattering of light within the absorbing material. However, the EDA falls off abruptly for $\lambda_0 > 750$ nm. This indicates a transition between regimes where the texture is both light-trapping and antireflective as opposed to merely antireflective alone.

Such behavior can be confirmed visually by inspecting the real part of the electric field profiles. Figure 2.11 shows the corresponding profiles for incident wavelengths of $\lambda = 700$ nm and $\lambda = 800$ nm. Clearly, the 700 nm profile exhibits much stronger angular scattering, which manifests as lateral variation in the field profile. On the other hand, the 800 nm profile looks like a nearly undistorted plane wave. The long-wavelength profile is therefore governed strictly by antireflection, while the short-wavelength profile experiences both antireflection and light-trapping properties. These results illustrate the utility of EDA calculations, since EPL cannot distinguish between index matching and angular scattering.

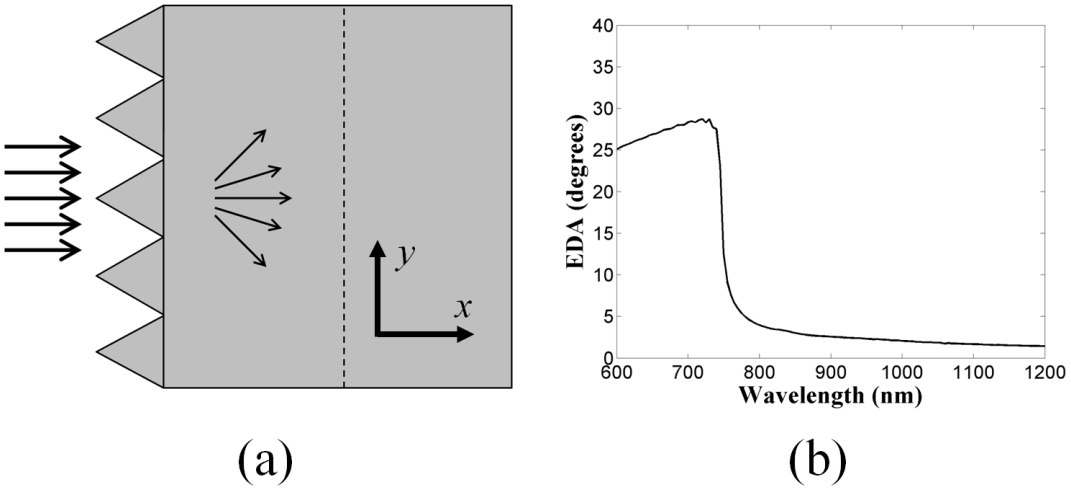

Figure 2.10. Numerical simulation of a triangular surface texture. (a) Bases are 400 nm and heights are 141 nm. (b) Simulated values for EDA.

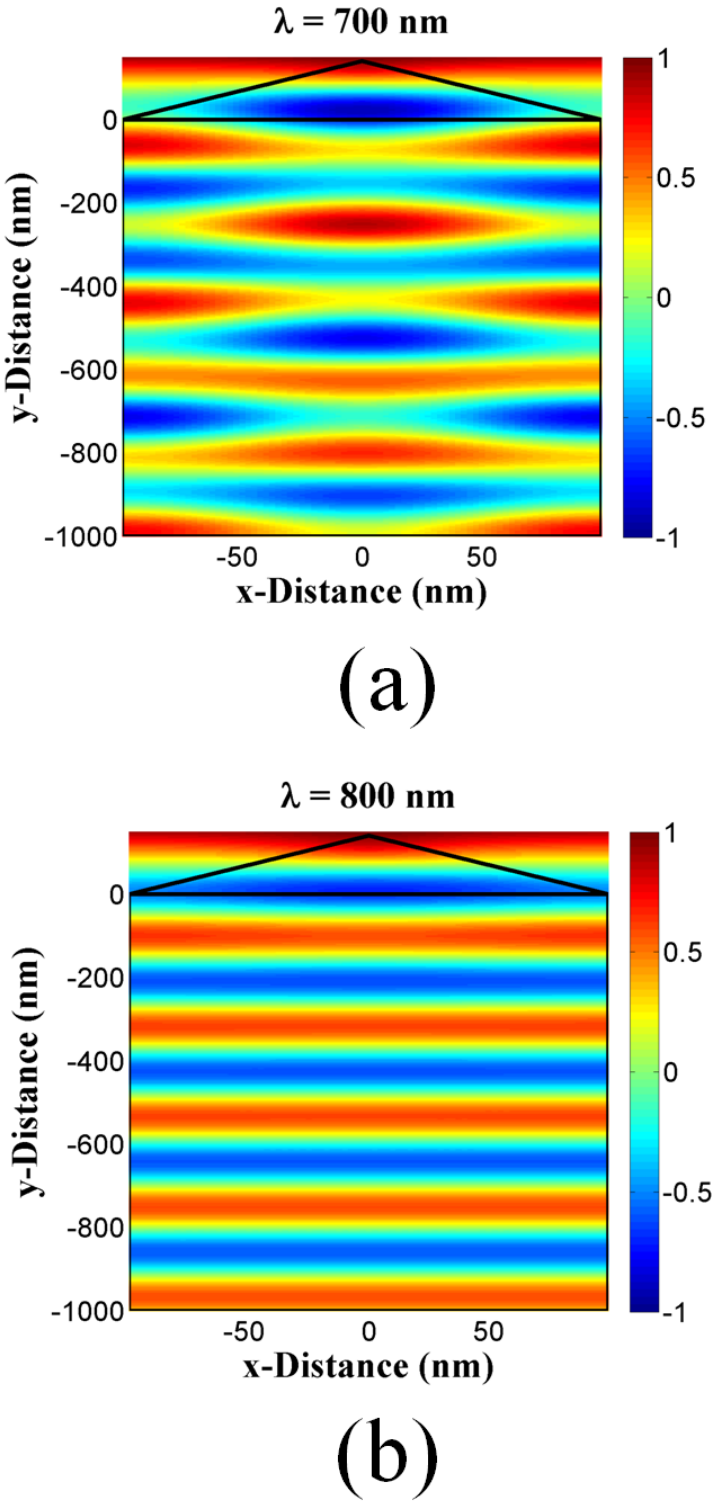

Figure 2.11. Real part of the electric field profiles for the triangular surface texture at (a) $\lambda = 700$ nm and (b) $\lambda = 800$ nm. Dark outlines indicate the surface texture.

CHAPTER 3

WAVE GUIDANCE IN LOSSY THIN FILMS

The theory of guided wave propagation has a long and rich history with many classic references at the graduate level [38, 32, 39, 40, 41]. Even so, the problem of guided wave propagation in lossy media is not nearly as well-understood as the lossless case. Because thin film solar cells may be modeled as planar dielectric waveguides with loss, it can be very useful to extend our understanding of wave guidance into the field silicon-based photovoltaics. Although significant progress was initially made in the late 60s and early 70s [42, 43, 44], the scope of such analysis still remains fairly limited. Later research in the field of semiconductor lasers eventually prompted the study of wave guidance in amplifying media [45], which is mathematically analogous to that of wave guidance in a lossy substrate. Eventually, the generalized problem of wave propagation in an n-layer guiding structure was solved in 1995 [46], though the generality of such a solution tends to obscure much of the underlying physics within the model.

The goal of this chapter is to examine the problem of lossy waveguide propagation by utilizing the familiar formalism of field matching at planar boundaries found in most classical references. Doing so reveals useful insight into the behavior of such physical models while also serving as a template for understanding variations on the same basic structure. It can further be shown that simple approximations to the exact solutions provide very high accuracy without the need for heavy complication of the classic formulations. Most importantly, extra mode solutions appear in the lossy case that do not exist in the classical set. These modes have tremendous longitudinal attenuation, making them especially interesting for the study of thin film photovoltaics.

The model structure of interest for this chapter is depicted in Figure 3.1 and consists of a dielectric slab with thickness $2h$ placed between two half-spaces. The dielectric slab, also called the *film* region, is lossy and may therefore be characterized by a complex index of refraction $\tilde{n}_f = n_f + j\kappa_f$. The region defined by $x > h$ is called the *cladding* region and has the complex index $\tilde{n}_c = n_c + j\kappa_c$. The region where $x < h$ is called the *substrate* and

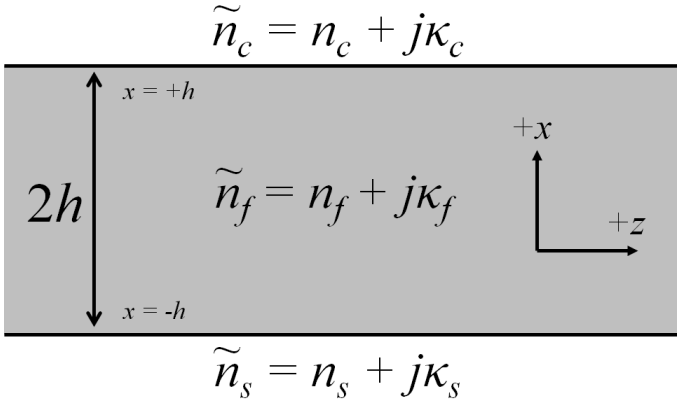

Figure 3.1. A dielectric slab waveguide with thickness $2h$. The cladding, film, and substrate regions are all defined by the complex indices of refraction $\tilde{n}_c$, $\tilde{n}_f$, and $\tilde{n}_s$.

has the complex index $\tilde{n}_s = n_s + j\kappa_s$. For the special case when $\tilde{n}_c = \tilde{n}_s$, the structure is said to be *symmetric*. Otherwise, the structure is *asymmetric*. This chapter first analyzes the fundamental physics behind the symmetric case before moving on to a more general analysis of the asymmetric case.

Just like in Chapter 2 of this dissertation, we shall adhere to the convention of a time-dependent phasor notation with the form of $\mathrm{Re}\{e^{jkx}e^{-j\omega t}\}$. The ultimate field solutions can likewise assume two possible polarization states, which are the transverse-electric (TE) and transverse-magnetic (TM) polarizations. For the TE case, the electric field intensity $\mathbf{E}$ is polarized along the $\hat{\mathbf{y}}$-direction. For the TM case, the magnetic flux density $\mathbf{H}$ is $\hat{\mathbf{y}}$-polarized.

3.1 Symmetric Waveguide, TE Polarization

We begin by assuming TE polarization in a symmetric dielectric waveguide so that $\hat{\mathbf{E}} = \hat{\mathbf{y}}$ and $\tilde{n}_c = \tilde{n}_s$. Like all propagation problems in a uniform medium, the functional form of the field solution must satisfy the vector Helmholtz equation, given by [38]

$$\nabla^2\mathbf{E}(x,z) + k^2\mathbf{E}(x,z) = 0\ . \tag{3.1}$$

For the case of a lossy film region, the propagation constant $k = k_f$ is a complex number that may be written as $k_f = k_0\tilde{n}_f$. The free-space wavenumber is then given by $k_0 = 2\pi/\lambda_0$, where λ_0 is the free-space wavelength of excitation for the model. The functional expression for $\mathbf{E}(x,z)$ can take on many forms, and the only conditions for a "correct" choice are the

constraints that the solutions satisfy the boundary conditions imposed by the geometry of the model and that the solutions be bounded over x.

When inside the film region ($|x| \leq h$), we shall assume that the electric field can be expressed in the following form:

$$\mathbf{E}(x,z) = \hat{\mathbf{y}}\, E_0 \left(e^{+j\beta_x x} e^{-\alpha_x x} \pm e^{-j\beta_x x} e^{+\alpha_x x} \right) e^{+j\beta_z} e^{-\alpha_z z} \ . \tag{3.2}$$

This expression represents two uniform plane waves propagating through a lossy medium. The constants β_x and β_z are the transverse and longitudinal *phase constants*, while α_x and α_z are the transverse and longitudinal *attenuation coefficients*, respectively. Both waves possess a forward component along the $+\hat{\mathbf{z}}$-direction and opposing components along $\hat{\mathbf{x}}$. The $\pm$ sign is indicative of a choice between either even (+) or odd (-) symmetry along x. E_0 is an arbitrary complex constant that determines the overall intensity and phase of the electric field.

The functional form of the field solution can be simplified by defining the complex-valued wavenumbers $k_x = \beta_x + j\alpha_x$ and $k_z = \beta_z + j\alpha_z$. Plugging back into Equation (3.2) therefore leads to

$$\mathbf{E}(x,z) = \hat{\mathbf{y}}\, E_0 \left(e^{+jk_x x} \pm e^{-jk_x x} \right) e^{+jk_z} \ . \tag{3.3}$$

This expression is identical to the field profiles typically assumed for the lossless case, with the only change being the assumption of complex values for the wavenumbers. The procedure is therefore directly analogous to the lossless case found in most references and will be followed here.

The cases for even and odd symmetry are usually managed separately by noting the Euler identities

$$2\cos(k_x x) = e^{+jk_x x} + e^{-jk_x x} \ , \tag{3.4}$$

$$2j\sin(k_x x) = e^{+jk_x x} - e^{-jk_x x} \ . \tag{3.5}$$

We may now write the even and odd field intensities using

$$\mathbf{E}_e(x,z) = \hat{\mathbf{y}}\, E_0 \cos(k_x x) e^{+jk_z} \qquad \text{(Even)} \ , \tag{3.6}$$

$$\mathbf{E}_o(x,z) = \hat{\mathbf{y}}\, E_0 \sin(k_x x) e^{+jk_z} \qquad \text{(Odd)} \ , \tag{3.7}$$

where the constant coefficients have been lumped into the E_0 term during substitution. If either of these expressions are plugged back into the Helmholtz equation, we find that the wavenumbers must satisfy the *dispersion relation*,

$$k_x^2 + k_z^2 = k_f^2 \ . \tag{3.8}$$

The next step is to assume a functional form for the field profile within the cladding region ($|x| \geq h$). In this case, we shall assume that $\mathbf{E}$ may be written as

$$\mathbf{E}(x,z) = \hat{\mathbf{y}}\, C E_0 e^{+jk_z z} \begin{cases} e^{+j\gamma(x-h)} & (x > h) \\ \pm e^{-j\gamma(x+h)} & (x < h) \end{cases} . \tag{3.9}$$

Note that because of the phase-matching condition between planar boundaries, the z-component to the wavenumber is identical in both the slab and cladding regions. We have also introduced the constant coefficient C to be determined later after enforcing continuity at the boundaries. The $\pm$ symbol is again determined by imposing even or odd symmetry onto the field solution. The complex propagation constant $\gamma = \gamma_r + j\gamma_i$ then satisfies another dispersion relation given by

$$\gamma^2 + k_z^2 = k_c^2 , \tag{3.10}$$

where $k_c = k_0 \tilde{n}_c$ is the intrinsic wavenumber of the cladding region.

The total electric field through all space may now be expressed as a piecewise function. For the even case, this takes on the form of

$$\mathbf{E}_e(x,z) = \hat{\mathbf{y}}\, E_0 e^{+jk_z z} \begin{cases} Ce^{+j\gamma(x-h)} & (x > h) \\ \cos(k_x x) & (|x| \leq h) \\ Ce^{-j\gamma(x+h)} & (x < h) \end{cases} . \tag{3.11}$$

For odd symmetry, we have a similar expression given by

$$\mathbf{E}_o(x,z) = \hat{\mathbf{y}}\, E_0 e^{+jk_z z} \begin{cases} Ce^{+j\gamma(x-h)} & (x > h) \\ \sin(k_x x) & (|x| \leq h) \\ -Ce^{-j\gamma(x+h)} & (x < h) \end{cases} . \tag{3.12}$$

With the total electric field now in hand, we are ready to solve for $\mathbf{H}(x,z)$. This is accomplished by applying Faraday's law,

$$\nabla \times \mathbf{E} = j\omega\mu_0 \mathbf{H} . \tag{3.13}$$

After carrying out the curl operation for the case of even symmetry, the result is found to be

$$\mathbf{H}_e(x,z) = \frac{E_0}{\omega\mu_0} e^{+jk_z z} \begin{cases} C\left(\gamma\,\hat{\mathbf{z}} - k_z\,\hat{\mathbf{x}}\right) e^{+j\gamma(x-h)} & (x > h) \\ jk_x\,\hat{\mathbf{z}}\sin(k_x x) - k_z\,\hat{\mathbf{x}}\cos(k_x x) & (|x| \leq h) \\ -C\left(\gamma\,\hat{\mathbf{z}} + k_z\,\hat{\mathbf{x}}\right) e^{-j\gamma(x+h)} & (x < h) \end{cases} . \tag{3.14}$$

For the case of odd symmetry, the solution is

$$\mathbf{H}_o(x,z) = \frac{E_0}{\omega\mu_0} e^{+jk_z z} \begin{cases} C\left(\gamma\,\hat{\mathbf{z}} - k_z\,\hat{\mathbf{x}}\right) e^{+j\gamma(x-h)} & (x > h) \\ -jk_x\,\hat{\mathbf{z}}\cos(k_x x) - k_z\,\hat{\mathbf{x}}\sin(k_x x) & (|x| \leq h) \\ C\left(\gamma\,\hat{\mathbf{z}} + k_z\,\hat{\mathbf{x}}\right) e^{-j\gamma(x+h)} & (x < h) \end{cases} , \tag{3.15}$$

The final step is to apply boundary conditions by enforcing continuity along the tangential field components at $x = \pm h$. Starting with the even case, continuity on the E-field implies

$$\cos(k_x h) = C \ . \tag{3.16}$$

Applying continuity on the z-component to the H-field then gives us

$$jk_x \sin(k_x h) = C\gamma \ . \tag{3.17}$$

Now divide Equation (3.17) by Equation (3.16) to find

$$jk_x \tan(k_x x) = \gamma \ . \tag{3.18}$$

Applying a similar procedure to the odd case likewise results in

$$-jk_x \cot(k_x x) = \gamma \ . \tag{3.19}$$

To handle the γ term, we combine Equations (3.8) and Equation (3.10) to arrive at

$$\gamma = j\sqrt{k_f^2 - k_c^2 - k_x^2} \ . \tag{3.20}$$

Substitution with this expression therefore leads us to the TE *eigenvalue equations* for the symmetric waveguide:

$$k_x \tan(k_x h) = \sqrt{k_f^2 - k_c^2 - k_x^2} \qquad \text{(TE, Even)} \ , \tag{3.21}$$

$$-k_x \cot(k_x h) = \sqrt{k_f^2 - k_c^2 - k_x^2} \qquad \text{(TE, Odd)} \ . \tag{3.22}$$

3.2 Symmetric Waveguide, TM Polarization

The derivation of the eigenvalue equations for the TM case follows a nearly identical procedure as the TE case. We therefore begin with the total field profile under even symmetry given by

$$\mathbf{H}_e(x,z) = \hat{\mathbf{y}}\, H_0 e^{+jk_z z} \begin{cases} Ce^{+j\gamma(x-h)} & (x > h) \\ \cos(k_x x) & (|x| \le h) \\ Ce^{-j\gamma(x+h)} & (x < h) \end{cases} \ . \tag{3.23}$$

For odd symmetry, the profile is

$$\mathbf{H}_o(x,z) = \hat{\mathbf{y}}\, H_0 e^{+jk_z z} \begin{cases} Ce^{+j\gamma(x-h)} & (x > h) \\ \sin(k_x x) & (|x| \le h) \\ -Ce^{-j\gamma(x+h)} & (x < h) \end{cases} \ . \tag{3.24}$$

We now need to solve for the total electric field. Beginning with Ampere's law, we know that

$$\nabla \times \mathbf{H} = -j\omega\epsilon_r\epsilon_0 \mathbf{E} \ , \tag{3.25}$$

where $\tilde{n}^2 = \epsilon_r$ for each dielectric region. For the case of even symmetry, this leads to

$$\mathbf{E}_e(x,z) = \frac{H_0}{\omega\epsilon_0} e^{+jk_z z} \begin{cases} \left(C/\tilde{n}_c^2\right)\left(-\gamma\,\hat{\mathbf{z}} + k_z\,\hat{\mathbf{x}}\right) e^{+j\gamma(x-h)} & (x > h) \\ \left(-jk_x/\tilde{n}_f^2\right)\,\hat{\mathbf{z}}\sin(k_x x) + \left(k_z/\tilde{n}_f^2\right)\,\hat{\mathbf{x}}\cos(k_x x) & (|x| \le h) \\ \left(C/\tilde{n}_c^2\right)\left(\gamma\,\hat{\mathbf{z}} + k_z\,\hat{\mathbf{x}}\right) e^{-j\gamma(x+h)} & (x < h) \end{cases} . \tag{3.26}$$

For the case of odd symmetry, the solution is

$$\mathbf{E}_o(x,z) = \frac{H_0}{\omega\epsilon_0} e^{+jk_z z} \begin{cases} \left(C/\tilde{n}_c^2\right)\left(-\gamma\,\hat{\mathbf{z}} + k_z\,\hat{\mathbf{x}}\right) e^{+j\gamma(x-h)} & (x > h) \\ \left(jk_x/\tilde{n}_f^2\right)\,\hat{\mathbf{z}}\cos(k_x x) + \left(k_z/\tilde{n}_f^2\right)\,\hat{\mathbf{x}}\sin(k_x x) & (|x| \le h) \\ -\left(C/\tilde{n}_c^2\right)\left(\gamma\,\hat{\mathbf{z}} + k_z\,\hat{\mathbf{x}}\right) e^{-j\gamma(x+h)} & (x < h) \end{cases} , \tag{3.27}$$

Finally, we enforce continuity on the tangential field components at $x = \pm h$. After following a similar procedure to the TE case, the TM eigenvalue equations are found to satisfy

$$k_x \tan(k_x h) = \frac{\tilde{n}_f^2}{\tilde{n}_c^2}\sqrt{k_f^2 - k_c^2 - k_x^2} \qquad \text{(TM, Even)} , \tag{3.28}$$

$$-k_x \cot(k_x h) = \frac{\tilde{n}_f^2}{\tilde{n}_c^2}\sqrt{k_f^2 - k_c^2 - k_x^2} \qquad \text{(TM, Odd)} . \tag{3.29}$$

3.3 Nonlinear Inversion

Because the eigenvalue equations are transcendental in nature, they cannot be directly solved for analytically. We must therefore utilize iterative inversion methods in order to find values for k_x that solve the eigenvalue equations. The process begins by defining the *residual* function $f(k_x)$ as the error in the eigenvalue equation with respect to k_x. These are functions are simply given by

$$f(k_x) = k_x \tan(k_x h) - \left[k_f^2 - k_c^2 - k_x^2\right]^{1/2} \qquad \text{(TE, Even)} , \tag{3.30}$$

$$f(k_x) = k_x \cot(k_x h) + \left[k_f^2 - k_c^2 - k_x^2\right]^{1/2} \qquad \text{(TE, Odd)} , \tag{3.31}$$

$$f(k_x) = \tilde{n}_c^2 k_x \tan(k_x h) - \tilde{n}_f^2\left[k_f^2 - k_c^2 - k_x^2\right]^{1/2} \qquad \text{(TM, Even)} , \tag{3.32}$$

$$f(k_x) = \tilde{n}_c^2 k_x \cot(k_x h) + \tilde{n}_f^2\left[k_f^2 - k_c^2 - k_x^2\right]^{1/2} \qquad \text{(TM, Odd)} . \tag{3.33}$$

Next, we define the *misfit* function ϕ as the squared norm of the residual:

$$\phi(k_x) = f(k_x) f^*(k_x) = ||f(k_x)||^2 . \tag{3.34}$$

Note that the asterisk $\{*\}$ denotes the complex conjugate operation. Our goal is to solve for all complex values of k_x such that $\phi(k_x) = 0$. We shall also enforce the condition $\beta_x > 0$.

The task of finding the zero values for ϕ may be accomplished through standard nonlinear optimization techniques. One common method is the *steepest descent method with linear*

line search [47, 48] and shall be applied to this problem. The first step is to compute the complex-valued derivatives of the residual with respect to k_x. It is therefore straightforward to show that

$$f'(k_x) = \quad k_x h \sec^2(k_x h) + \tan(k_x h) + k_x \left[k_f^2 - k_c^2 - k_x^2\right]^{-1/2} \qquad \text{(TE, Even)} , \quad (3.35)$$

$$f'(k_x) = -k_x h \csc^2(k_x h) + \cot(k_x h) - k_x \left[k_f^2 - k_c^2 - k_x^2\right]^{-1/2} \qquad \text{(TE, Odd)} , \quad (3.36)$$

$$f'(k_x) = \quad k_x \tilde{n}_c^2 h \sec^2(k_x h) + \tan(k_x h) + k_x \tilde{n}_f^2 \left[k_f^2 - k_c^2 - k_x^2\right]^{-1/2} \qquad \text{(TM, Even)} , \quad (3.37)$$

$$f'(k_x) = -k_x \tilde{n}_c^2 h \csc^2(k_x h) + \cot(k_x h) - k_x \tilde{n}_f^2 \left[k_f^2 - k_c^2 - k_x^2\right]^{-1/2} \qquad \text{(TM, Odd)} . \quad (3.38)$$

Starting with a trial solution $k_{x,0}$, we now execute the following algorithm:

$$f_n = f(k_{x,n}) \quad (3.39)$$

$$F_n = f'(k_{x,n}) \quad (3.40)$$

$$\ell_n = F_n^* f_n \quad (3.41)$$

$$g_n = -F_n \ell_n \quad (3.42)$$

$$u_n = \frac{||\ell_n||^2}{||g_n||^2} \quad (3.43)$$

$$k_{x,n+1} = k_{x,n} - u_n \ell_n . \quad (3.44)$$

This algorithm is repeated until $\phi(k_{x,n})$ falls below some given threshold of error tolerance (say, 10^{-9}). For the case of relatively low-loss dielectrics, a good choice for $k_{x,0}$ is the mode solution to an equivalent system without any loss. It is also important to bear in mind that the line-search algorithm applies a linear approximation to the derivative of the residual when determining the optimal step size u_n. As a result, u_n can often be over-estimated, thus leading to a divergence in the search algorithm. This can be alleviated by ensuring that each step of the algorithm enforces the *descent condition*, which is written as

$$\phi(k_{x,n+1}) < \phi(k_{x,n}) . \quad (3.45)$$

Whenever a new iteration fails to satisfy this condition, a very simple remedy is to reduce u_n by a factor of 1/2. The iteration attempt is then repeated until Equation (3.45) finally holds, and the search can then continue normally.

3.4 Field Profiles

As a demonstration case, let us assume TE polarization with $\tilde{n}_f = 2.0 + j0.5$, $\tilde{n}_c = 1.5$, and a normalized film thickness of $h/\lambda_0 = 0.5$. The logarithmic power of the misfit function, $10 \log_{10} \phi$, is plotted in Figure 3.2 for the even modes. The initial trial solution is chosen by

the $M = 2$ mode for an equivalent lossless system ($\beta_x \lambda_0 = 7.27$) and indicated by the "X" mark. After applying the steepest decent method, the exact solution converges to a value of $k_x \lambda_0 = 7.89 + j0.77$, indicated by the "O" mark. Solving Equations (3.8) and (3.20) then produces the full set of propagation constants. Expressed in terms of electrical length, these are

$$k_z \lambda_0 = 9.89 + j3.38 \ ,$$
$$\gamma \lambda_0 = -5.89 + j5.67 \ .$$

Figure 3.3 shows the electric fields along both x and z generated from Equation (3.11) and normalized to unit amplitude. The horizontal lines indicate the waveguide boundaries. We can also observe the exponential decay in field strength along z, which we naturally expect from propagation through a lossy film.

Figure 3.4 shows the first four mode profiles for the same model. These mode profiles are generally analogous to the same solutions for a lossless system and propagate in a similar manner. An exception to this is the $M = 3$ mode, which actually does not exist as a viable solution for a lossless slab. This is a key difference between lossy and lossless waveguides, where lossy systems possess an equal or greater number of eigenmodes. These extra modes are referred to as *loss guided* modes [45], since they only occur in lossy films. We can also solve for the *effective index* of the waveguide by using

$$n_{eff} = k_z / k_0 = 1.14 + j0.6 \ ,$$

which is less than the real index of either the film or the cladding layers.

Figure 3.5, demonstrates the change in the $M = 2$ mode as the extinction coefficient is incremented from $\kappa_f = 0.01$ to $\kappa_f = 2$. It is useful to note that as the film region grows more lossy, its field profile within the slab experiences relatively little perturbation with respect to the lossless case. The only significant change is that higher loss tends to result in greater field confinement within the slab.

Another apparent aspect of the field solution is that γ possesses a real-valued component. Under lossless conditions, γ would be purely imaginary, thereby producing strict exponential decay to the fields in the cladding region. When the film is lossy, the real component to γ causes an additional phase oscillation with respect to x on top of the decay fields. Using the diagram in Figure 3.6, we can understand this behavior by depicting the evanescent fields as rays that leave the waveguide at some point z and then re-enter at some point $z + \Delta z$ (a common description for the Goos-Hanchen effect [49]). However, because the film

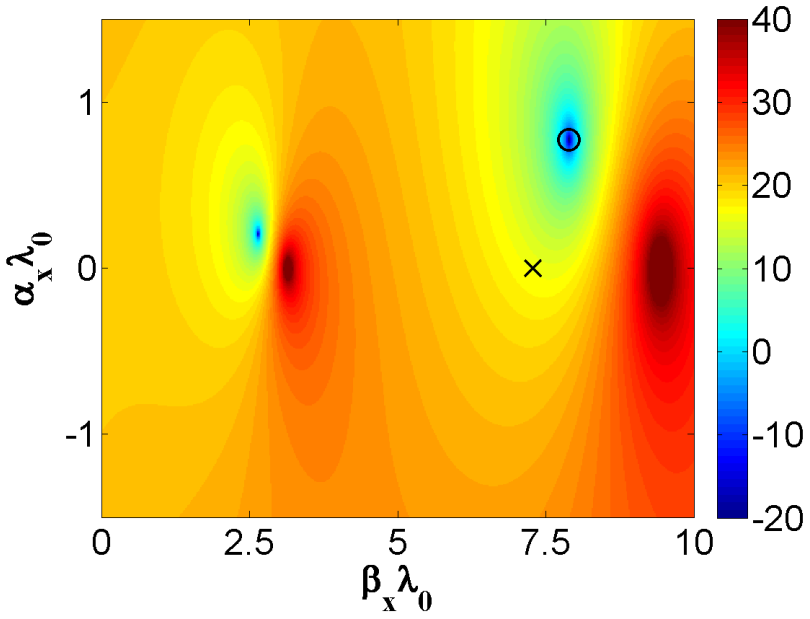

Figure 3.2. Logarithmic power of the misfit function, $10\log_{10}\phi$, for the even modes ($M = 0$ and $M = 2$ solutions indicated). Model parameters are $\tilde{n}_f = 2 + j0.5$, $\tilde{n}_c = 1.5$, and $h/\lambda_0 = 0.5$. The "X" mark indicates the initial trial solution ($k_{x,0}\lambda_0 = 7.27$). The "O" mark indicates the lossy solution for the $M = 2$ mode ($k_x\lambda_0 = 7.89 + j0.77$).

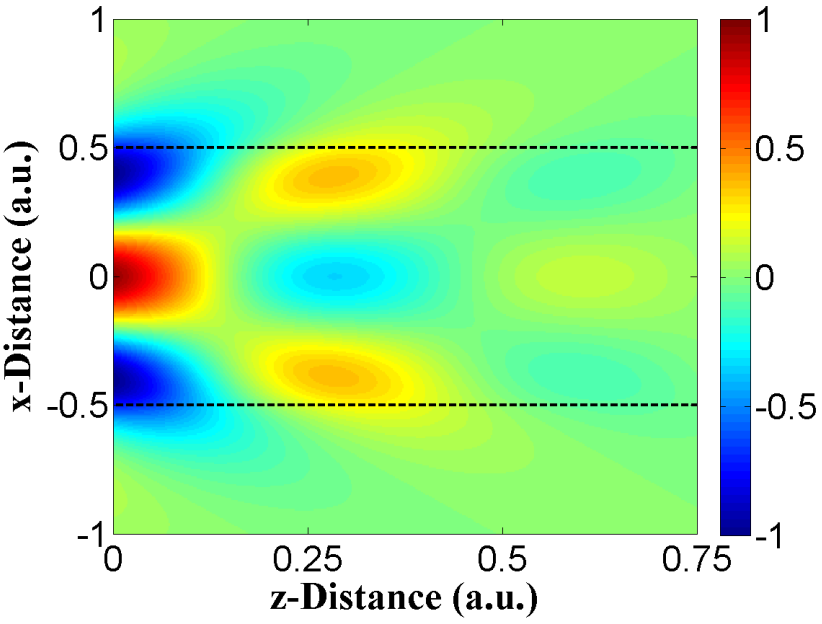

Figure 3.3. Normalized electric field profile along both x and z (V/m). Horizontal bars indicate the waveguide boundaries.

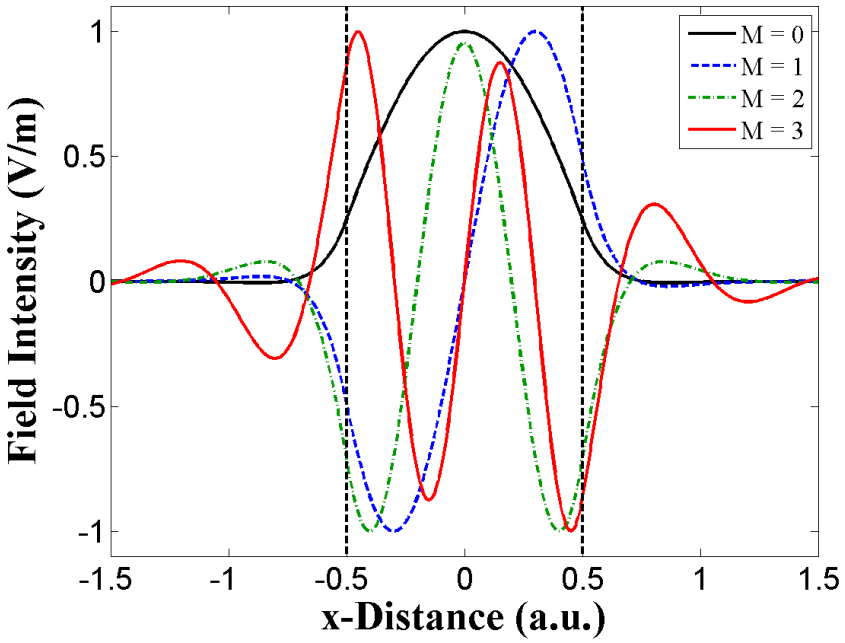

Figure 3.4. The first four modes of the lossy waveguide example from Figure 3.2.

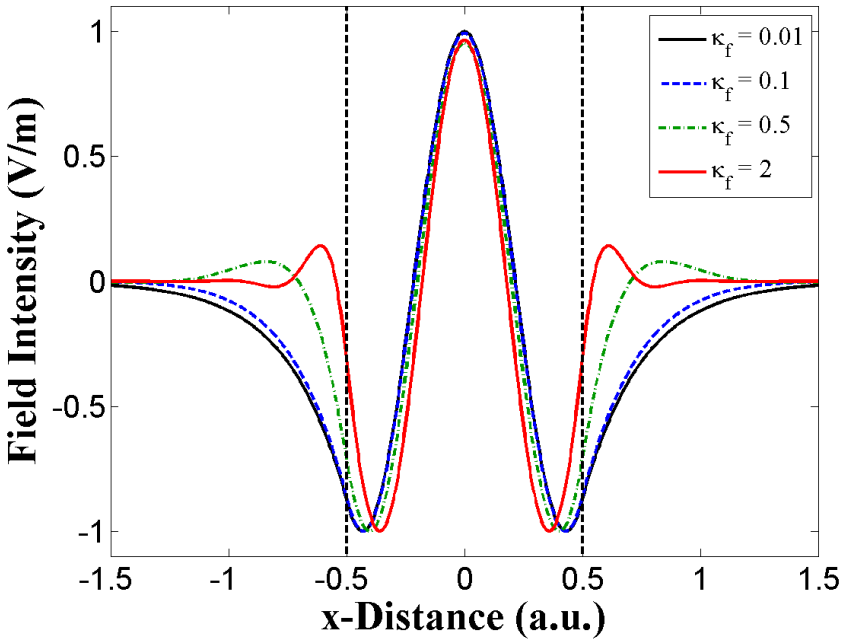

Figure 3.5. $M = 2$ profile from the previous figure under increasing values of κ_f.

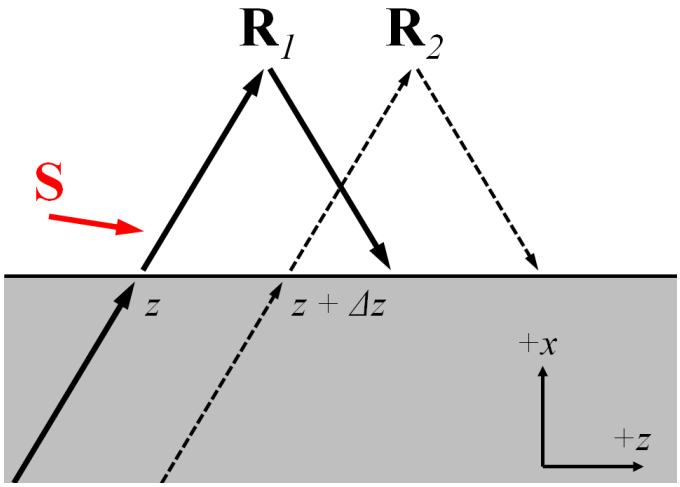

Figure 3.6. Ray diagram of the Goos-Hanchen effect for a lossy film. The ray $\mathbf{R}_1$ is more intense than the ray $\mathbf{R}_2$, leading to a net flow of power into the film at any given point along z. Consequently, the time-averaged Poynting's vector $\mathbf{S}$ in the cladding region has an x-component that points toward the film.

is lossy, the ray $\mathbf{R}_1$ carries greater field intensity than the ray $\mathbf{R}_2$. This means that, for $|x| > h$, the time-averaged Poynting's vector $\mathbf{S} = \frac{1}{2}\mathrm{Re}\{\mathbf{E} \times \mathbf{H}^*\}$ will always contain some nonzero x-component that points toward the film region. Visually speaking, this manifests as a "skewing" of the fields in the cladding region as the constant phase fronts are pushed off-normal with respect to the waveguide.

3.4.1 Cladding Loss

Let us now turn our attention to the more general case of loss within the cladding region. This situation can be demonstrated by specifying a film index of $\tilde{n}_f = 2.0 + j0.2$ and a cladding index $\tilde{n}_c = 1.5 + j0.5$. Figure 3.7 shows the logarithmic power of the misfit while Figure 3.8 shows the $M = 2$ field profile. Waveguide dimensions are the same as before, with $h/\lambda_0 = 0.5$. Because we made no assumptions about the nature of $\tilde{n}_c$, the same nonlinear inversion scheme is still perfectly valid when solving the eigenvalue equations. The solutions to the propagation constants were therefore found to be

$$k_x\lambda_0 = 7.53 - j0.35 \ ,$$
$$k_z\lambda_0 = 10.15 + j1.82 \ ,$$
$$\gamma\lambda_0 = 2.20 + j5.07 \ .$$

The general behavior of the waveguide remains mostly the same as before, with well-defined modes and a distinct longitudinal attenuation. The only significant difference is a reversal of the sign on γ_r, which manifests as a skewing of the cladding fields into the opposite direction. The actual direction of the skewing also depends strongly on the relative difference between κ_f and κ_c.

3.4.2 Branch Cuts

A special phenomenon worth noting is the existence of a branch cut in the misfit ϕ due to the square-root function within the residual. The cut occurs when the imaginary component of the radical is set to zero, since this is the point where the square-root of a complex value switches phase during numerical computation. Carrying out this calculation therefore leads us to the expression

$$\alpha_x = \frac{k_0^2(n_f\kappa_f - n_c\kappa_c)}{\beta_x} \ . \tag{3.46}$$

The branch point itself is then found by setting the argument of the radical to zero:

$$k_{x,BP} = \sqrt{k_f^2 - k_c^2} \ . \tag{3.47}$$

An example branch cut is highlighted by the dashed curves in Figure 3.9 and Figure 3.10 using the even mode solutions for the misfit function. Model parameters are given by $\tilde{n}_f = 2.0 + j0.5$, $\tilde{n}_c = 1.5 + j0.1$, and $h/\lambda_0 = 0.5$. Although ϕ maps to two unique values along every point in the complex plane, only one at a time can be rendered on a single 2D graph. The default mapping is shown in Figure 3.9 using the positive value of the radical. An alternative mapping is found by switching the sign of the square-root function in Equations (3.21)-(3.29) and then re-deriving ϕ accordingly. This function is shown in Figure 3.10 and reveals a potential set of new zeros in ϕ. However, because of the negative sign on the radical, γ_i generally becomes negative as well and produces a field profile that diverges as $|x| \to \infty$. We may therefore reject the solutions under a negative square-root function since such modes are not physically viable.

The origins of loss-guided modes can also be understood from Figures 3.9 and 3.10. As κ_f grows in value, the branch cut moves further away from the origin to expose new zeros in the positive solution for ϕ. Because of this trend, lossy waveguides will always possess an equal or greater number of viable mode solutions than their lossless counterparts. It also introduces a new set of mode solutions that violate the typical restrictions of total internal reflection (TIR). As an example, Figures 3.11 and 3.12 show a waveguide solution using $\tilde{n}_f = 2.0 + j0.1$, $\tilde{n}_c = 2.25$, and $h/\lambda_0 = 0.5$. Although the cladding index is greater than the

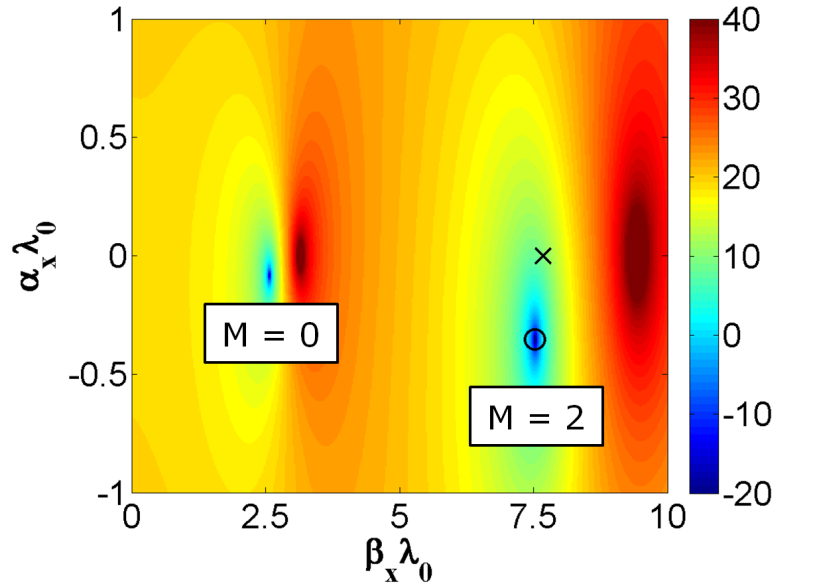

Figure 3.7. Logarithmic power ($10\log_{10}\phi$) for the even mode misfit with cladding loss. Model parameters are $\tilde{n}_f = 2+j0.2$, $\tilde{n}_c = 1.5+j0.5$ and $h/\lambda_0 = 0.5$. The "X" mark indicates the initial trial solution ($k_{x,0}\lambda_0 = 7.27$). The "O" mark indicates the lossy solution for the $M = 2$ mode ($k_x\lambda_0 = 7.53 - j0.35$).

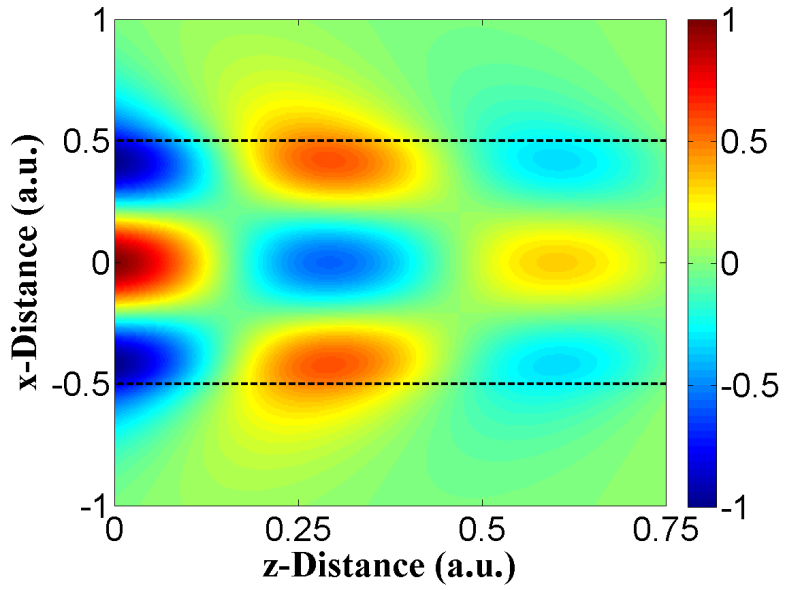

Figure 3.8. Normalized electric field profile for the $M = 2$ mode in the previous figure. Horizontal bars indicate the waveguide boundaries.

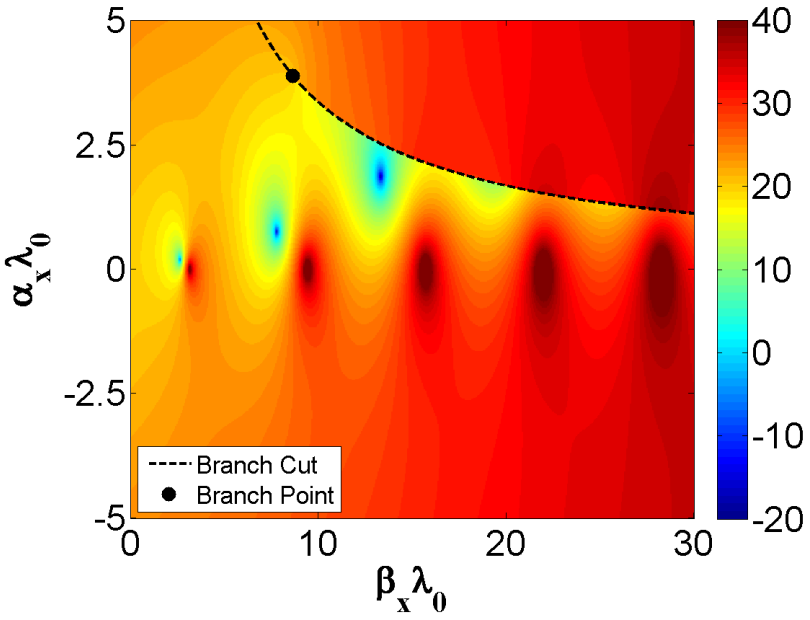

Figure 3.9. Positive solution to the misfit function with respect to the complex radical in Equation (3.21).

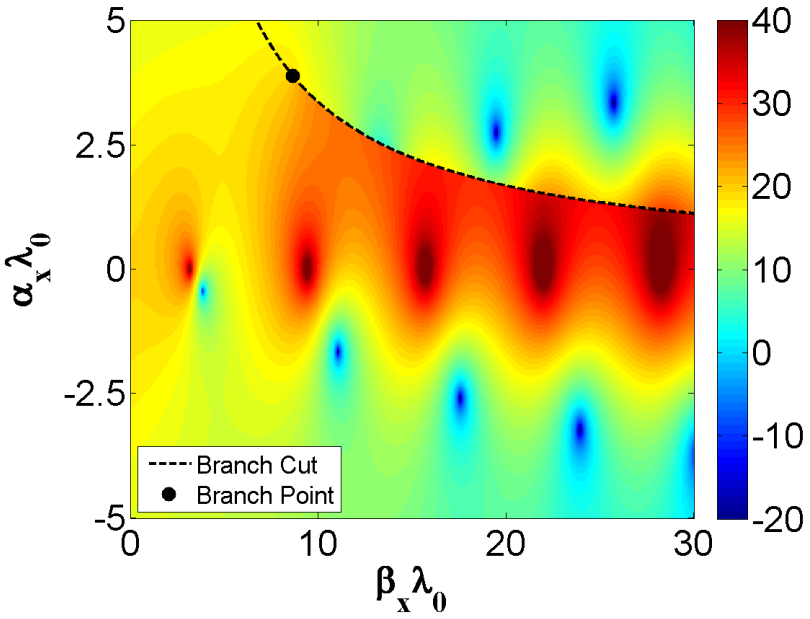

Figure 3.10. Negative solution to the misfit function with respect to the complex radical in Equation (3.21). The negative misfit reveals a new set of solutions to the eigenvalue equation, though such solutions are not physically admissible.

real part of the film index, there still exists a mode solution at $k_x\lambda_0 = 2.8 + j0.77$, called an *antiguided* mode [45]. If we solve for the n_{eff}, we also find that

$$n_{eff} = k_z/k_0 = 1.95 + j0.07 \ ,$$

which is lower than either the film or cladding. The transition for this mode occurs at $\kappa_f \approx 0.03$, below which the branch cut overlaps the zero in ϕ and removes it as a physically viable solution. Low-loss and lossless waveguides therefore do not possess guided mode solutions for $n_c > n_f$, which serves to reinforce the conventional TIR condition.

3.4.3 Longitudinal Attenuation

Another aspect of lossy mode propagation is that mode attenuation along the z-direction increases with mode number. This behavior is demonstrated in Figure 3.13(a) using $\tilde{n}_f = 2.5 + j0.01$, $\tilde{n}_c = 1.5$, $h = 1.5$ μm, and $\lambda_0 = 1.0$ μm. This prediction can be corroborated through numerical simulation with the finite-difference time-domain method [35]. Because the mode profiles change very little under low-loss conditions, we may excite the lossy film with its equivalent lossless mode and then measure the simulated power loss over some fixed distance. This result is plotted in Figure 3.13(a) by the red data points and agrees extremely well with the analytical computations.

Such behavior in mode attenuation may be visually understood from a geometric optics perspective by considering the ray paths illustrated in Figure 3.13(b). Because the high-order modes (black) propagate at steeper angles than low-order modes (red), each ray must propagate through more material for the same displacement along z. For the case of low-loss dielectrics ($\kappa_f << 1$), simple trigonometry suggests that

$$\alpha_z \approx \alpha_0 \Gamma \sec\theta \ , \tag{3.48}$$

where $\theta = \tan^{-1}(\beta_x/\beta_z)$ is the elevation angle of the ray and $\alpha_0 = k_0\kappa$ is the intrinsic attenuation coefficient of the film. The coefficient Γ is a correction factor that accounts for the fraction of total power in the film region relative to the total power in the mode itself. Because the cladding layers are not lossy, the evanescent fields do not experience any Ohmic power loss and therefore need to be accounted for. A rigorous discussion of this problem is presented in [50] for the case of amplifying media, but naturally carries over to the case of lossy media. The parameter Γ can therefore be set to the modal confinement factor given by

$$\Gamma = \frac{\int_{-h}^{+h} |\mathcal{E}_m(x)|^2 \, dx}{\int_{-\infty}^{+\infty} |\mathcal{E}_m(x)|^2 \, dx} \ , \tag{3.49}$$

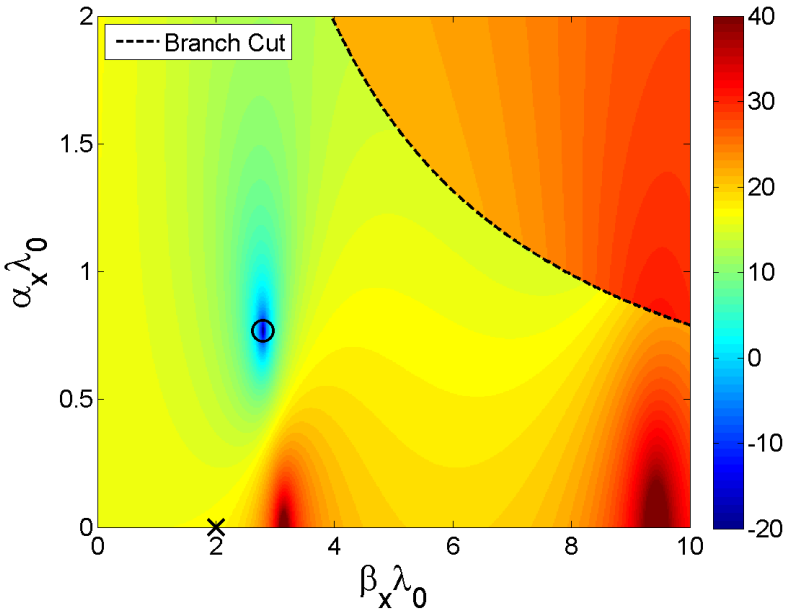

Figure 3.11. Log-power of the even misfit using $\tilde{n}_f = 2.0 + j0.1$, $\tilde{n}_c = 2.25$, and $h/\lambda_0 = 0.5$. The solution at $k_x\lambda_0 = 2.8 + j0.77$ is an antiguided mode.

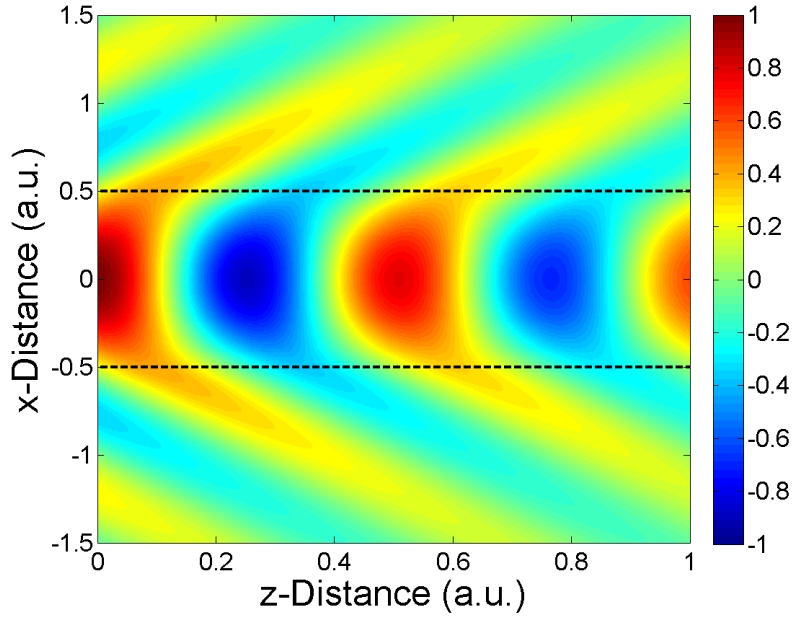

Figure 3.12. Normalized field profile of the antiguidance mode from Figure 3.11. The "skewing" effect on the evanescent fields is much more dramatic in these modes.

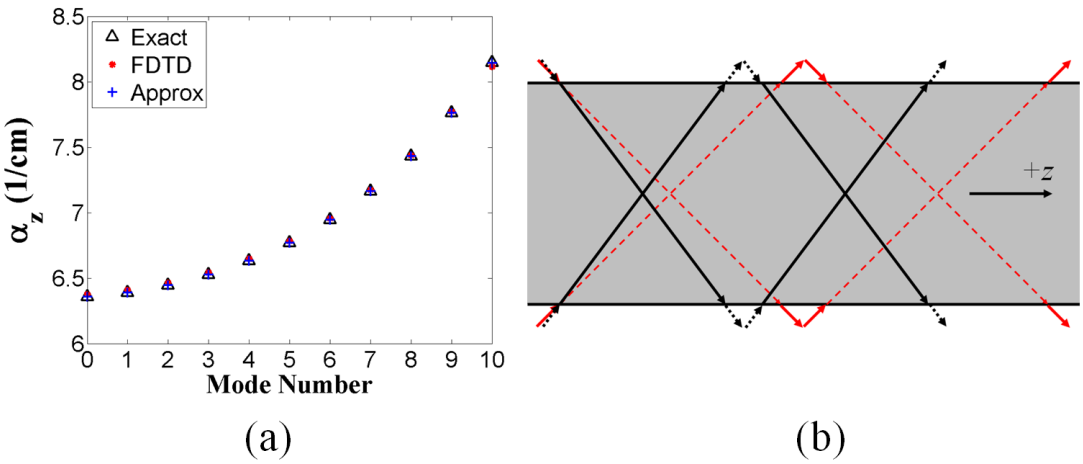

Figure 3.13. Longitudinal attenuation with $\tilde{n}_f = 2.5 + j0.01$, $\tilde{n}_c = 1.5$, $h = 1.5$ μm and $\lambda_0 = 1.0$ μm. (a) Exact computation (black) for the longitudinal attenuation coefficient (α_z) compared against numerical simulation (red) and the low-loss approximation (blue). (b) Ray propagation in the film according to geometric optics.

where $\mathcal{E}_m(x)$ is the normalized TE field profile along x for the mth mode. These mode profiles can be filled by the solution for an equivalent lossless slab, which is valid as long as the lossless field profiles generally match the lossy case. Using Figure 3.5 as a guide, we surmise that this will generally be true for $\kappa_f << 1$. If the cladding is lossy as well, then a more general solution needs to be applied to the model.

Computations from Equation (3.48) are also plotted in Figure 3.13(a) and agree very well with the exact values. The utility of applying the low-loss approximation is that it avoids the added tedium of solving Equation (3.21) for complex wavenumbers. It also presents an intuitively satisfying picture based on purely ray-tracing arguments. For the case of TM modes, the normalized field profile $\mathcal{E}_m(x)$ can be taken from the y-component of the magnetic field for similar results [50]. In general, the net effect is that high-order modes will attenuate more rapidly than low-order modes. The only exception to this trend occurs for modes that propagate very close to the critical angle of the slab. In such cases, the evanescent fields will penetrate far into the cladding region, thereby reducing mode confinement. The result is a small value for Γ that offsets the large $\sec\theta$ dependence.

3.4.4 Applications to Thin-Film Photovoltaics

One simple way to model a photovoltaic cell is to consider a lossy dielectric slab backed by a perfect electrical conductor (PEC) as shown in Figure 3.14(a). Neglecting any surface oxide layers or anti-reflective coatings, such a model is a reasonable representation of a

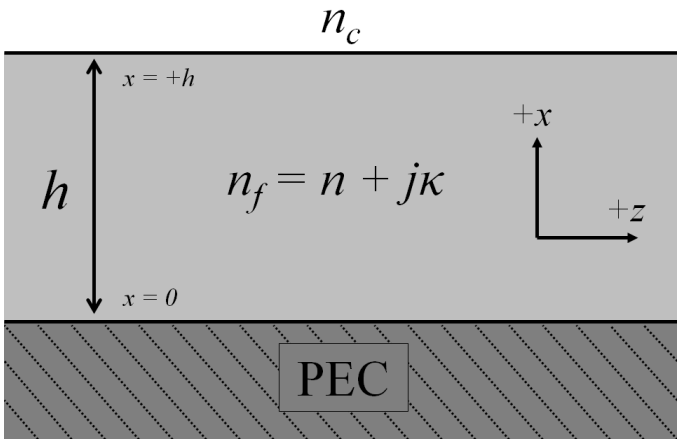

Figure 3.14. Configuration for a lossy dielectric waveguide backed by a PEC ground plane. Solutions are equivalent to the odd modes of a symmetric dielectric slab with twice the width.

typical thin-film solar cell. We can then mathematically solve for the eigenmodes by extracting only the odd-symmetry solutions from a symmetric dielectric slab with twice the width.

As an example, Figure 3.15 shows the TE field distribution for the $M = 4$ mode of an $h = 500$ nm film of amorphous silicon at $\lambda_0 = 600$ nm ($\tilde{n}_f = 4.6 + j0.3$, $\tilde{n}_c = 1$) [51]. Figure 3.16 computes α_z for all TE modes of the device. The solutions using the low-loss approximation are also indicated by the blue markers at each data point. Clearly, the low-loss approximation produces a very accurate measure of the mode attenuation. We can also see that high-order modes are generally more lossy than low-order modes, with the $M = 6$ mode possessing an absorption coefficient that is roughly twice that of the fundamental $M = 0$ mode. However, the lossy waveguide also possesses an extra five eigenmodes in addition to the seven that exist for the equivalent lossless model. These loss-guided modes cannot be derived from any low-loss approximation and are strictly unique to the lossy waveguide model. It is also apparent that such modes possess dramatically higher values for α_z than do the classical modes.

An example profile of the $M = 7$ mode is illustrated in Figure 3.17(a). When viewed along the transverse axis, such modes generally behave in the familiar fashion one should expect from a guided mode. In particular, there are eight characteristic peaks and valleys, as well as a strong evanescent decay in the cladding region. Figure 3.17(b) shows the same mode when viewed along the longitudinal axis. From this perspective, the mode is almost

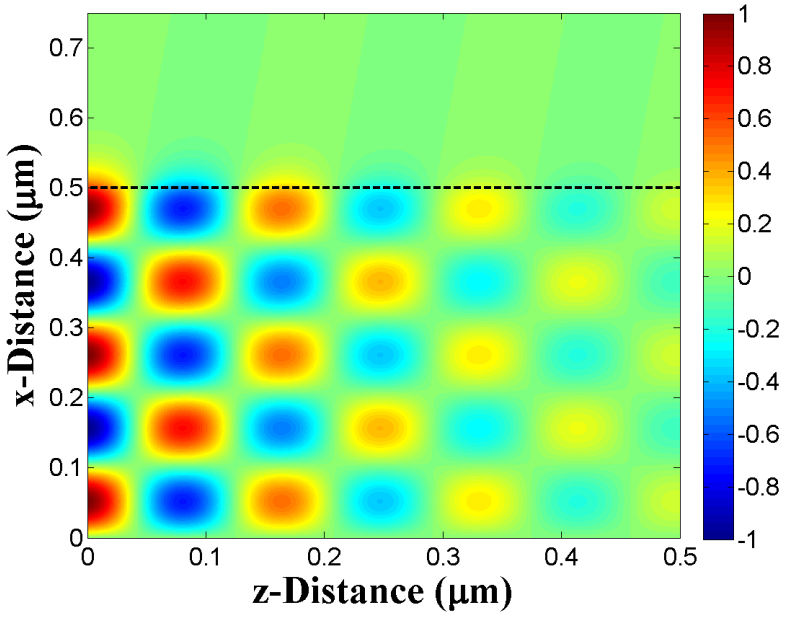

Figure 3.15. Electric field profile of the $M = 4$ mode for thin ($h = 500$ nm) film of amorphous silicon at $\lambda_0 = 600$ nm. Indices are given by $\tilde{n}_f = 4.6 + j0.3$ and $\tilde{n}_c = 1$.

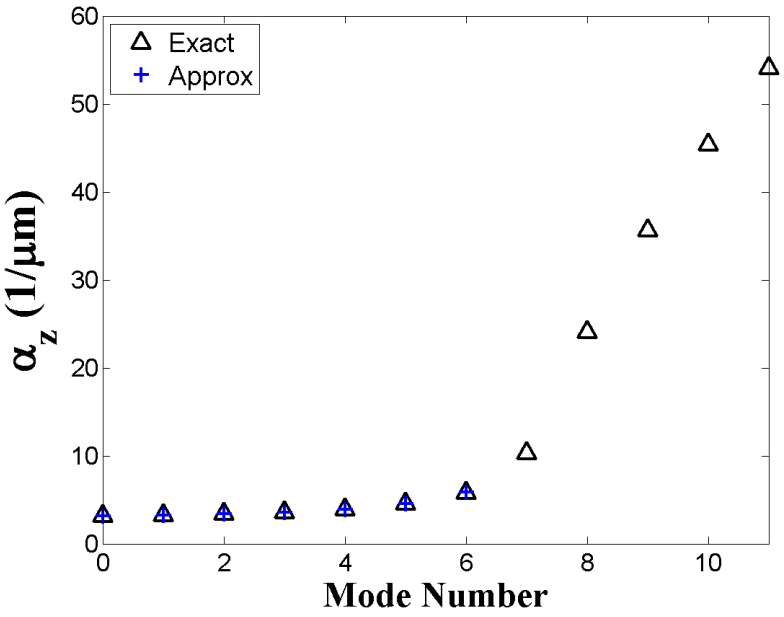

Figure 3.16. Longitudinal attenuation coefficient versus mode number for the same model in Figure 3.15. The low-loss approximation is applied to the first seven modes, but does not exist for the extra five in the lossy model.

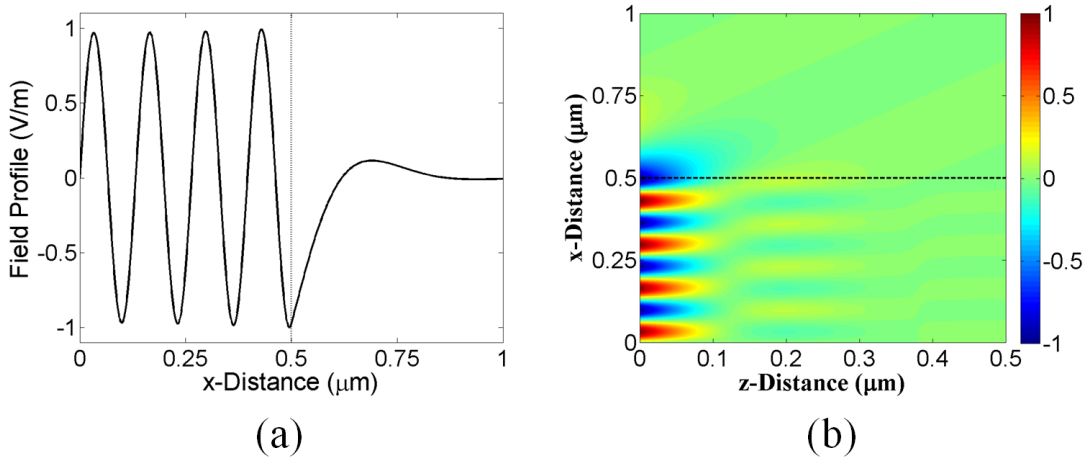

Figure 3.17. Electric field profile of the $M = 7$ mode from the previous figure. (a) 1D profile along x. (b) Full 2D profile, showing dramatic longitudinal absorption of the loss-guided mode.

completely attenuated within a single wavelength cycle. This behavior is characteristic for the additional modes in a lossy dielectric waveguide, which tend to have very high values for α_z. Such results may have useful implications for light-trapping applications where the ultimate goal is to maximize light absorption in a finite film [20].

3.5 Asymmetric Waveguide, TE Case

Let us now turn our attention to the case of an asymmetric waveguide such that $\tilde{n_c} \neq \tilde{n}_s$. In this case, we shall assume an electric field profile with the functional form of

$$\mathbf{E}(x,z) = \hat{\mathbf{y}}\, E_0 e^{+jk_z z} \begin{cases} Ce^{+j\gamma_c(x-h)} & (x > h) \\ e^{+jk_x x} + Be^{-jk_x x} & (|x| \leq h) \\ De^{-j\gamma_s(x+h)} & (x < h) \end{cases} . \tag{3.50}$$

Note that the new coefficients B and D account for the asymmetry in the system. We have also introduced the distinct propagation constants γ_c and γ_s for the cladding and substrate regions. Solving for the magnetic field intensity therefore leads to

$$\mathbf{H}(x,z) = \frac{E_0}{\omega\mu_0} e^{+jk_z z} \begin{cases} C\left(\gamma_c\,\hat{\mathbf{z}} - k_z\,\hat{\mathbf{x}}\right) e^{+j\gamma_c(x-h)} & (x > h) \\ \left(\hat{\mathbf{z}}\,k_x - \hat{\mathbf{x}}\,k_z\right) e^{+jk_x x} - \left(\hat{\mathbf{z}}\,k_x + \hat{\mathbf{x}}\,k_z\right) Be^{-jk_x x} & (|x| \leq h) \\ -D\left(\gamma_s\,\hat{\mathbf{z}} - k_z\,\hat{\mathbf{x}}\right) e^{-j\gamma_s(x+h)} & (x < h) \end{cases} . \tag{3.51}$$

Next, we enforce continuity on the tangential field components at the planar boundaries. This leads us to the following system of equations:

$$e^{+jk_xh} + Be^{-jk_xh} = C \ , \tag{3.52}$$

$$e^{-jk_xh} + Be^{+jk_xh} = D \ , \tag{3.53}$$

$$k_x\left(e^{+jk_xh} - Be^{-jk_xh}\right) = \gamma_c C \ , \tag{3.54}$$

$$k_x\left(e^{-jk_xh} - Be^{+jk_xh}\right) = -\gamma_s D \ . \tag{3.55}$$

Using a little clever manipulation and substitution, it is possible to combine these expressions into a single equation in terms of k_x. The TE asymmetric eigenvalue equation is therefore found to be

$$j\tan(2k_xh) = \frac{k_x\left(\gamma_c + \gamma_s\right)}{k_x^2 + \gamma_c\gamma_s} \ , \tag{3.56}$$

where γ_c and γ_s satisfy the dispersion relations

$$\gamma_c = j\sqrt{k_f^2 - k_c^2 - k_x^2} \ , \tag{3.57}$$

$$\gamma_s = j\sqrt{k_f^2 - k_s^2 - k_x^2} \ . \tag{3.58}$$

Again, it is worth nothing that Equation (3.56) is identical to the eigenvalue equation one would find for the equivalent lossless system [40]. The only difference is the addition of complex values for the propagation constants, thereby requiring a more difficult inversion scheme for generating the eigenmode solutions.

3.6 Asymmetric Waveguide, TM Case

Following an identical procedure to the TE case, the magnetic field intensity is expressed as

$$\mathbf{H}(x,z) = \hat{\mathbf{y}}\, H_0 e^{+jk_zz} \begin{cases} Ce^{+j\gamma_c(x-h)} & (x > h) \\ e^{+jk_xx} + Be^{-jk_xx} & (|x| \le h) \\ De^{-j\gamma_s(x+h)} & (x < h) \end{cases} \ . \tag{3.59}$$

We can similarly derive the electric field intensity as

$$\mathbf{E}(x,z) = \frac{H_0}{\omega\epsilon_0} e^{+jk_zz} \begin{cases} \left(C/\tilde{n}_c^2\right)\left(-\gamma_c\,\hat{\mathbf{z}} + k_z\,\hat{\mathbf{x}}\right)e^{+j\gamma_c(x-h)} & (x > h) \\ \left(1/\tilde{n}_f^2\right)\left(-k_x\,\hat{\mathbf{z}} + k_z\,\hat{\mathbf{x}}\right)e^{+jk_xx} & \\ \quad + \left(1/\tilde{n}_f^2\right)\left(k_x\,\hat{\mathbf{z}} + k_z\,\hat{\mathbf{x}}\right)Be^{-jk_xx} & (|x| < h) \\ \left(D/\tilde{n}_s^2\right)\left(+\gamma_s\,\hat{\mathbf{z}} + k_z\,\hat{\mathbf{x}}\right)e^{-j\gamma_s(x+h)} & (x < h) \end{cases} \ . \tag{3.60}$$

Enforcing continuity then leads us to

$$e^{+jk_xh} + Be^{-jk_xh} = C \ , \tag{3.61}$$

$$e^{-jk_xh} + Be^{+jk_xh} = D \ , \tag{3.62}$$

$$k_x\left(e^{+jk_xh} - Be^{-jk_xh}\right) = \frac{\tilde{n}_f^2}{\tilde{n}_c^2}\gamma_c C \ , \tag{3.63}$$

$$k_x\left(e^{-jk_xh} - Be^{+jk_xh}\right) = -\frac{\tilde{n}_f^2}{\tilde{n}_s^2}\gamma_s D \ . \tag{3.64}$$

By analogy with the TE case, we now arrive at the TM eigenvalue equation

$$j\tan(2k_xh) = \frac{k_x\tilde{n}_f^2\left(\tilde{n}_s^2\gamma_c + \tilde{n}_c^2\gamma_s\right)}{k_x^2\tilde{n}_c^2\tilde{n}_s^2 + \tilde{n}_f^4\gamma_c\gamma_s} \ . \tag{3.65}$$

3.7 Nonlinear Inversion: Generic Case

Just like the case of the symmetric waveguide model, the asymmetric eigenvalue equations are nonlinear and can be solved only through iterative methods. We therefore define the residual functions as

$$f_{TE}(k_x) = \tan(2k_xh)\left(k_x^2 + \gamma_c\gamma_s\right) + jk_x\left(\gamma_c + \gamma_s\right) \ , \tag{3.66}$$

$$f_{TM}(k_x) = \tan(2k_xh)\left(k_x^2\tilde{n}_c^2\tilde{n}_s^2 + \tilde{n}_f^4\gamma_c\gamma_s\right) + jk_x\tilde{n}_f^2\left(\tilde{n}_s^2\gamma_c + \tilde{n}_c^2\gamma_s\right) \ . \tag{3.67}$$

Next, we need to solve for the derivatives of each residual with respect to k_x. For the TE case, this is found to be

$$\begin{aligned} f'_{TE}(k_x) =& \tan(2k_xh)\left(2k_x + \gamma_c\gamma'_s + \gamma'_c\gamma_s\right) + 2h\sec^2(2k_xh)\left(k_x^2 + \gamma_c\gamma_s\right) \\ &+ jk_x\left(\gamma'_c + \gamma'_s\right) + j\left(\gamma_c + \gamma_s\right) \ , \end{aligned} \tag{3.68}$$

where the parameters γ'_c and γ'_s are

$$\gamma'_c = jk_x\left(k_f^2 - k_c^2 + k_x^2\right)^{-1/2} \ , \tag{3.69}$$

$$\gamma'_s = jk_x\left(k_f^2 - k_s^2 + k_x^2\right)^{-1/2} \ . \tag{3.70}$$

For the TM case, we have the similar expression

$$\begin{aligned} f'_{TM}(k_x) =& \tan(2k_xh)\left(2k_x\tilde{n}_c^2\tilde{n}_s^2 + \tilde{n}_f^4\gamma_c\gamma'_s + \tilde{n}_f^4\gamma'_c\gamma_s\right) \\ &+ 2h\sec^2(2k_xh)\left(k_x^2\tilde{n}_c^2\tilde{n}_s^2 + \tilde{n}_f^4\gamma_c\gamma_s\right) \\ &+ jk_x\tilde{n}_f^2\left(\tilde{n}_s^2\gamma'_c + \tilde{n}_c^2\gamma'_s\right) + j\tilde{n}_f^2\left(\tilde{n}_s^2\gamma_c + \tilde{n}_c^2\gamma_s\right) \ . \end{aligned} \tag{3.71}$$

The solution for k_x can now be found by applying the same steepest descent algorithm outlined in Equations (3.39)–(3.44).

3.8 Asymmetric Branch Cuts

Just like the symmetric case, there also exist branch cuts in the misfit function for the asymmetric waveguide. However, because there are now two radicals instead of one, the misfit function ϕ maps to four unique solutions instead of two. By analogy with the symmetric case, we can therefore show that the branch cuts occur along the points where

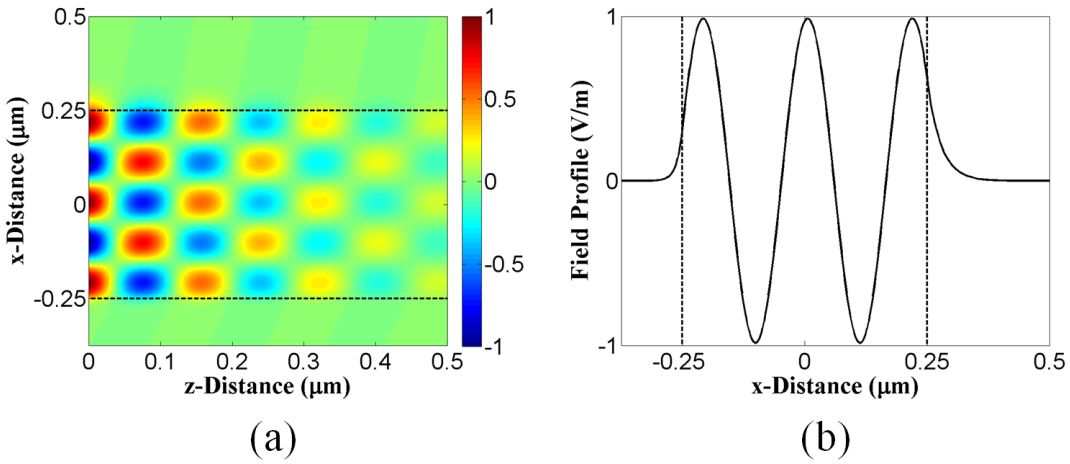

Figure 3.18. Field profiles for the $M = 4$ mode of an asymmetric lossy waveguide. (a) 2D field profile. (b) 1D field profile along x.

the imaginary components to the radicals in γ_c and γ_s equal zero. These values are found to be

$$\alpha_{x,c} = \frac{k_0^2 \left(n_f \kappa_f - n_c \kappa_c\right)}{\beta_x} \ , \tag{3.72}$$

$$\alpha_{x,s} = \frac{k_0^2 \left(n_f \kappa_f - n_s \kappa_s\right)}{\beta_x} \ . \tag{3.73}$$

Again, it is important to recognize that many solutions exist where $\phi(k_x) = 0$. The only criterion for an admissible eigenmode is that $|\mathbf{E}(x,z)|$ remain bounded along x. We can also solve for the branch points to find

$$k_{x,BPc} = \sqrt{k_f^2 - k_c^2} \ , \tag{3.74}$$

$$k_{x,BPs} = \sqrt{k_f^2 - k_s^2} \ . \tag{3.75}$$

3.9 Field Profiles

As a final demonstration case, consider a thin a-Si film backed by an imperfect metal contact like aluminum (Al). So instead of using the PEC contact like that in Figure 3.15, let us replace it with the complex index $\tilde{n}_s = 1.26 + j7.2$. Figure 3.18 shows the resultant field profile for the $M = 4$ mode that emerges from this model. As we should expect, the mode profile is very similar to the PEC example, but with some finite field penetration into the substrate.

CHAPTER 4

LIGHT TRAPPING WITH EMBEDDED NANOPARTICLES

This chapter introduces a novel technique for enhanced light absorption in optically thin solar cells by embedding particles directly within the active semiconductor layer. Data was generated exclusively through use of numerical simulation with the finite-difference time-domain (FDTD) method by utilizing the Lumerical software package [35]. The results of this chapter are therefore strictly theoretical, and many challenges must be overcome before a practical implementation may be demonstrated. Even so, the results presented here clearly demonstrate a potential for light trapping in thin films that works significantly better than scattering by noble-metal nanoparticles placed along the surface. The system geometry is also generalized to that of an infinite half-space in order to maintain a focus on the distinction between light injection and light trapping. The next chapter will then focus on a more realistic solar cell model by introducing a back contact to the system. We shall then explore the various design parameters which optimize light absorption in the active layer.

4.1 Background

Noble-metal nanoparticles (NPs) have received a great deal of theoretical and experimental attention in recent years for their ability to enhance the efficiency of thin-film solar cells [27, 52, 53, 54, 55, 56, 57]. Such metallic structures are commonly referred to as a *plasmonic* NPs due to the surface plasmon-polariton excitation that occurs under illumination by an external electromagnetic wave. High-conductivity metals like gold (Au) and silver (Ag) tend to make especially high-quality resonators due to the large polarizability of the electric dipole moment. Plasmonic NPs therefore tend to produce very large absorption and scattering cross-sections when excited at or near resonance.

Despite their reported successes, plasmon-enhanced solar cells suffer from many serious drawbacks that may limit their potential for commercial application. The first issue is the prevalent use of expensive noble metals as the materials of choice for plasmonic scattering.

Such metals can have practical advantages from the point of view of chemical application or light scattering, but potentially suffer from serious economic handicaps when implemented on a large, industrial scale. Another major problem is that plasmonic NPs have a difficult time cooperating with anti-reflective coatings (ARCs) made out of simple nitride layers [28, 58, 29]. So although metal nanospheres can potentially enhance light absorption in bare-surface designs, it can often be preferable to remove the spheres altogether and simply implement a planar nitride ARC instead.

In an effort to retain the light-scattering capabilities of spherical NPs as well as the light-injection properties of an ARC, this dissertation proposes that scatterers be placed directly within the active film layer of a silicon-based solar cell. As we shall see in the following sections, this effectively decouples the light-injection properties of the ARC from the light-trapping properties of the NPs. Absorption gains are therefore cumulative and complementary, allowing each to be independently optimized in a unified optical system.

4.2 Baseline Model

The simulation model used as a baseline throughout this discussion is depicted in Figure 4.1. The system of interest is an infinite half-space of c-Si with an optional ARC placed at the surface. This makes our findings more general and geometry-independent than, for example, if we had used a reflecting metal layer at the back surface. The ARC itself is modeled with silicon nitride (Si_3N_4) because it is a commonly used material in silicon-based solar cells. A nitride thickness of 75 nm was chosen in order to maximize light injection around a wavelength of $\lambda = 600$ nm, which is the approximate peak in the AM 1.5 spectrum. The dielectric properties of c-Si and Si_3N_4 are readily available from standard references such as the *Handbook of Optical Constants of Solids* [34], and were used to define the material constants on this model. Although a real solar cell would also be chemically doped to form an internal p-n junction, the dielectric function of Si is not significantly altered in the spectral range below 1200 nm for reasonable doping concentrations. We also assume that the model is irradiated from the $+z$-direction at normal incidence by the AM 1.5 solar spectrum.

Although a simple planar system can readily be solved analytically, the inclusion of spherical particles is much more difficult. We shall therefore utilize the Lumerical software package to numerically generate data from these models [35]. This package utilizes the finite-difference time-domain (FDTD) algorithm to simulate the full-wave propagation of electric and magnetic fields within the model [59]. To mimic the effects of an infinite half-space at the top ($+z$) and bottom ($-z$) boundaries of the domain, a perfectly matched

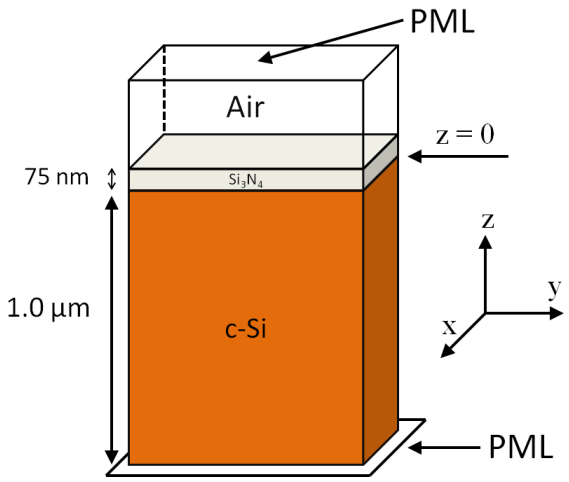

Figure 4.1. Baseline solar cell model used for simulation. The c-Si layer is 1.0 μm thick and topped by a 75 nm layer of Si_3N_4. Perfectly matched layers (PMLs) terminate the simulation volume at the top and bottom boundaries. Periodic boundary conditions along x and y mimic the effects of an infinitely repeating unit cell.

layer (PML) was inserted to absorb outgoing waves. We can also replicate the infinite extent of the absorber layer along x and y by utilizing periodic boundary conditions.

Next, let us define the power transmission coefficient $T(z, \lambda)$ as the fraction of incident power density with wavelength λ that penetrates an xy plane located at some depth z. For example, $T(0, \lambda)$ represents the fraction of incident power that enters the c-Si, since the $z = 0$ plane defines the top boundary of the c-Si half-space. Using this definition, we can now define the depth-specific absorption factor using

$$A(z, \lambda) = T(0, \lambda) - T(z, \lambda) \ . \tag{4.1}$$

The parameter $A(w, \lambda)$ therefore measures the total fraction of incident power absorbed within a c-Si layer of thickness w at the surface of the half-space.

With these parameters in mind, we can now define the *spectral absorbance factor* as

$$S(z, \lambda) = A(z, \lambda)\Phi_0(\lambda) \ , \tag{4.2}$$

where $\Phi_0(\lambda)$ is the AM 1.5 spectral reference given in Chapter 1 of this dissertation. Using this convention, the two parameters of interest will be $S(\infty, \lambda)$ and $S(w, \lambda)$. The parameter $S(\infty, \lambda)$ quantifies the total sunlight that physically enters the c-Si region, since all power is eventually absorbed in an infinitely thick half-space. $S(w, \lambda)$ then tells us the amount of sunlight that is absorbed in the top w thickness of the infinite half-space. In particular, we shall be interested in the value $w = 1.0$ μm, since this represents the approximate scale of

a typical thin-film device. These metrics allow us to independently differentiate between light injection into c-Si layer and light scattering within it.

4.2.1 Polynomial Correction

A subtle problem with numerical simulation arises from the nature of FDTD over a broad bandwidth. In order to simulate the dielectric properties of a material like c-Si, the Lumerical software package attempts to apply a polynomial curve fit to sampled data. However, as λ approaches the bandgap λ_g in c-Si, the extinction coefficient κ exponentially approaches zero. Because a finite-order polynomial cannot precisely track such changes, significant errors in the simulated absorption factor will accrue as $\lambda \to \lambda_g$, usually with a significant bias toward higher absorption.

To correct for this error, we first solve for the equivalent path length of the simulated absorption factor using

$$\ell_{\text{sim}} = -\frac{1}{2\alpha} \ln\left[1 - A(z, \lambda)\right] \ . \tag{4.3}$$

Even though the attenuation coefficient α is inaccurate, the propagation of electromagnetic waves is reasonably independent of α in a low-loss system. The ultimate value for ℓ_{sim} should therefore remain constant even if we re-ran the simulation with modified values of α. This allows us to correct the absorption factor by replacing the inaccurate α with a corrected value α' taken directly from linearly interpolated material data. Solving for the corrected absorption A' therefore gives

$$A'(z, \lambda) = 1 - e^{-2\alpha' \ell_{\text{sim}}} \ . \tag{4.4}$$

Figures 4.2 and 4.3 show the spectral absorbance curves for the case of a bare c-Si half-space and a c-Si half-space with a nitride ARC. These values were first generated by FDTD simulation and then corrected using Equation (4.4). Comparison against analytical calculations shows that the mean error after correction is less than 1 %. Each plot contains a $z = \infty$ curve and a $z = 1.0$ μm curve, showing the disparity in absorption that occurs at wavelengths above $\lambda = 500$ nm (Note that the $z = \infty$ curve does not need any corrections). Using numerical integration of the two curves, it is found that the presence of the ARC adds an additional 39 % of light injection to the c-Si half-space relative to the bare surface. Total light absorption within the top 1.0 μm layer is also found to increase by 47 % because of the ARC. These results therefore validate the FDTD simulation as well as demonstrate the absorption gains that may be achieved through the application of a simple nitride ARC.

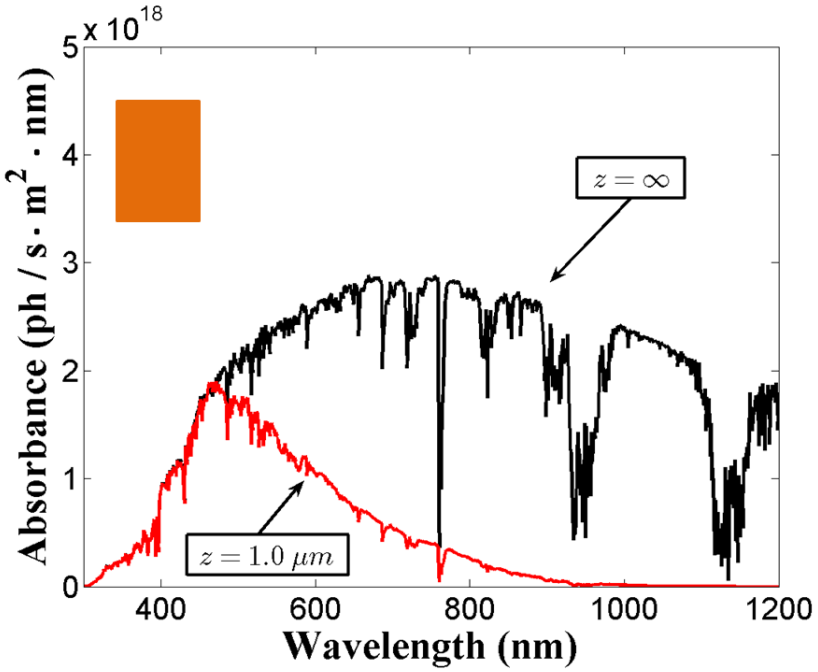

Figure 4.2. Spectral absorbance curves for a bare c-Si half space.

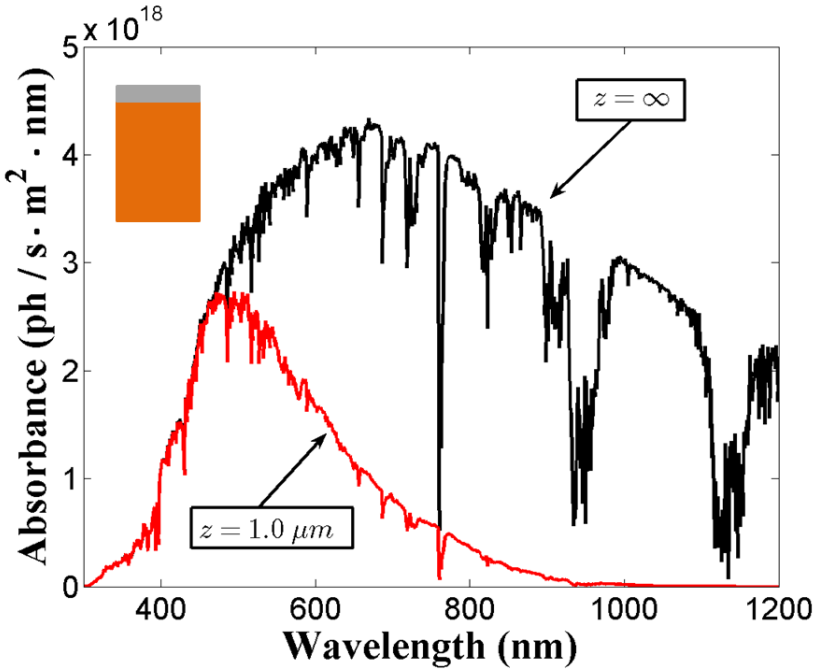

Figure 4.3. Spectral absorbance curves a c-Si half space with a 75 nm ARC made from Si_3N_4. The presence of the ARC increases light injection by 39 % and light absorption within the top 1.0 μm layer by 47 %.

4.3 The Problem with Plasmons

To demonstrate the effectiveness of plasmonic nanoparticles, consider now the model in Figure 4.4. A common technique with plasmon-enhanced solar cells is to deposit an array of gold (Au) or silver (Ag) nanospheres along the surface of the device. The key design parameters are therefore spherical diameter D and array pitch p. Typical values for these parameters are on the order of $D = 100$ nm and $p = 400$ nm [56], and Figures 4.5 and 4.6 show the spectral absorbance curves using these values with an Au sphere.

Several key features are apparent from these simulation results. Starting with the $z = \infty$ curve in Figure 4.5, we can see that the presence of the Au sphere helps to increase light injection between 500–900 nm. When integrated across the entire spectrum of interest, light injection is further seen to increase by 2.5 %. Below 500 nm however, the presence of the spheres actually reduces light injection. Since this is the region where c-Si absorbs very strongly, the net absorption within the top 1.0 μm balances out to almost no change at all (-0.6 %). From the results in Figure 4.6, it is also apparent that the nanospheres do not cooperate well with the nitride ARC. Below $\lambda = 700$ nm, the $z = \infty$ curve shows a strong reduction and loses 1.8 % in the overall light injection. Worse still, the light absorption in the top 1.0 μm is reduced by 7.1 %.

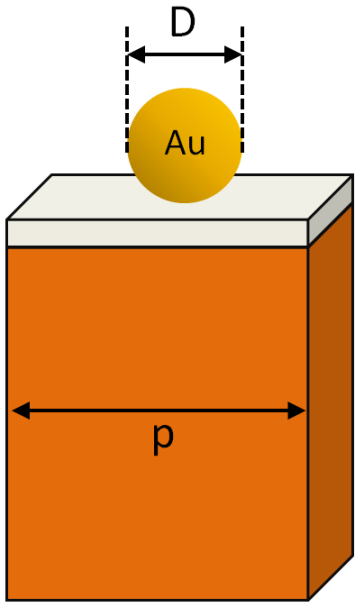

Figure 4.4. Metallic nanoparticle deposited along the surface of the baseline model. The particle is defined by a diameter D and array pitch p.

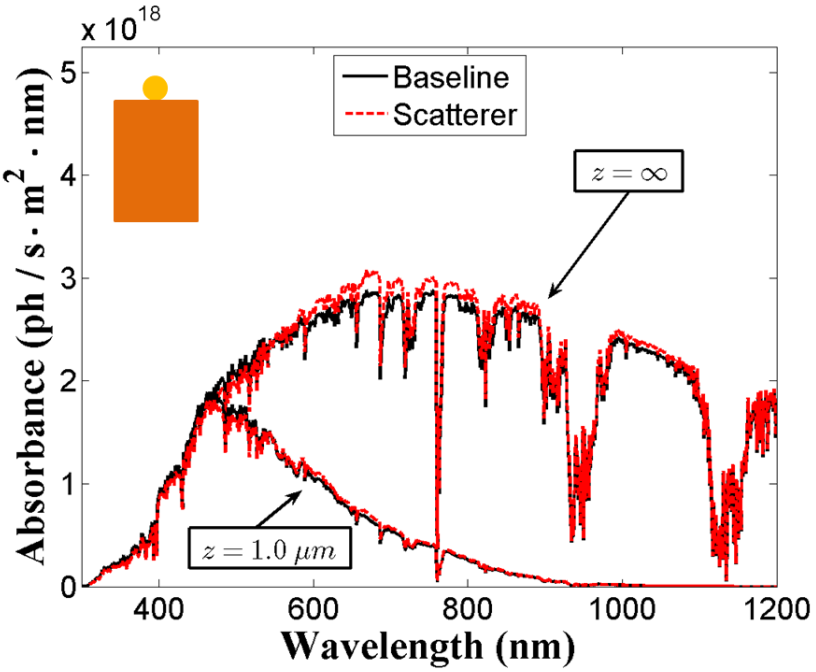

Figure 4.5. Spectral absorbance curves for a $D = 100$ nm sphere of Au placed at the surface for a bare c-Si half-space. Array pitch is $p = 400$ nm, giving 4.9 % area coverage.

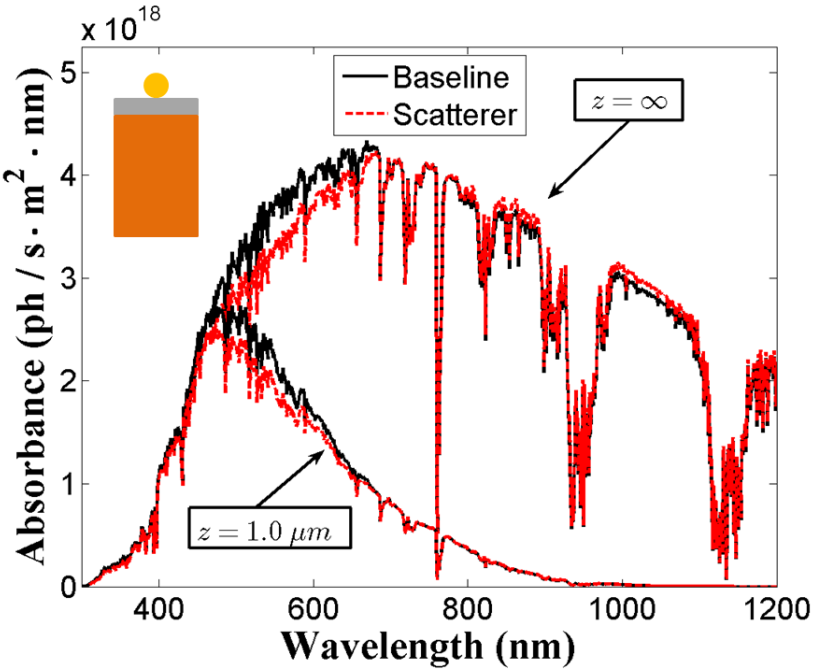

Figure 4.6. Spectral absorbance curves with a $D = 100$ nm sphere of Au placed along the same geometry, but with a 75 nm layer of Si_3N_4 at the surface.

Although this is only a single example out of many possible geometric configurations, such results are very typical of plasmonic enhancement in thin films. Specifically, the anti-reflective properties of plasmonic nanoparticles are much more effective on a bare c-Si surface rather than a surface already coated with an ARC. Similar research from other sources have also corroborated this outcome in a variety of configurations [58, 29]. So while many experimental solar cells have still been able to report efficiency gains through the use of plasmonic nanoparticles, it is debatable if such designs would not have performed better with just a nitride ARC.

4.4 Embedded Dielectric Nanospheres

We now turn our attention to the model in Figure 4.7, which shows a dielectric nanosphere embedded directly within the active semiconductor layer underneath the ARC. The geometry is again defined by a characteristic diameter D and array pitch P, but also by a characteristic depth z_0 below the surface. There are also many available choices for the material of the particle, but silicon dioxide (SiO_2) possesses several properties that make it an ideal candidate for investigation:

1. SiO_2 is optically lossless, thereby avoiding the complication of any absorption by the nanosphere itself.

2. SiO_2 ($n \approx 1.5$) possesses a reasonably strong dielectric contrast with c-Si ($n \approx 3.5$). This guarantees a significant amount of light scattering by the spheres.

3. The interface between SiO_2 and c-Si can potentially lead to extremely low dangling bond densities and interface recombination velocities. This is in contrast to metallic particles, which would be very strong recombination centers and dramatically reduce the quantum efficiency of a real solar cell.

4.4.1 Light Scattering by SiO_2 Spheres in c-Si

The ideal choice of D is not immediately straightforward, but classical Mie theory does provide useful insight into where to begin. We start by imagining a uniform plane wave with power density S_i as it illuminates a particle of some arbitrary geometry and index of refraction. As the incident field strikes the particle, some of those fields will naturally scatter away in various directions with some total power P_s. The ratio of P_s to S_i then has units of area and is called the *scattering cross section*:

$$C_s = \frac{P_s}{S_i} \ . \tag{4.5}$$

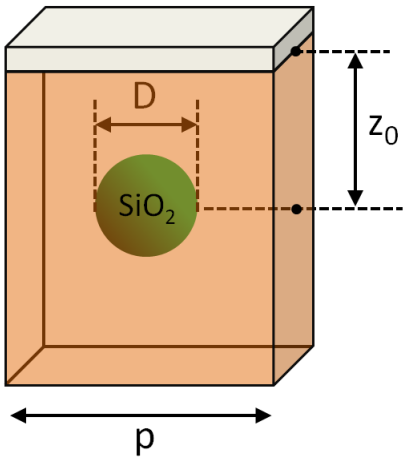

Figure 4.7. Dielectric nanosphere embedded directly within the active semiconductor layer. The particle is defined by a diameter D, depth z_0, and array pitch p.

If we then normalize C_s by the physical cross-sectional area of the particle, the result is called the *scattering efficiency*. For the case of a spherical particle, the cross-sectional area is simply πr^2, with r being the radius of the sphere. The scattering efficiency of a spherical particle is therefore

$$Q_s = \frac{C_s}{\pi r^2} \ . \tag{4.6}$$

The key usefulness of spherical geometries is that calculations of Q_s take on closed-form solutions. A complete derivation of this is rather involved, so the reader is referred to Bohren and Huffman's excellent text, *Absorption and Scattering of Light by Small Particles* [60], for a rigorous introduction to classical Mie theory. However, most standard references will assume that the ambient medium of the system is lossless, which is definitely not the case for a material like c-Si. Special modifications must therefore be included in the standard Mie formulations to account for absorption in the ambient material. The solution to this problem was first derived by Sudiarta and Chylek in 2001 [61], and their formulation will be used throughout this chapter when performing Mie calculations.

Figure 4.8 shows the scattering efficiencies of SiO_2 nanospheres embedded in an ambient medium of c-Si. The diameters indicated are $D = 150$ nm, $D = 200$ nm, $D = 300$ nm, and $D = 400$ nm. The general behavior is that large-diameter spheres possess more broadband scattering efficiencies that peak around $Q_s \approx 2$. This means larger spheres are generally more desirable for trapping light due to their greater ability to scatter light over more

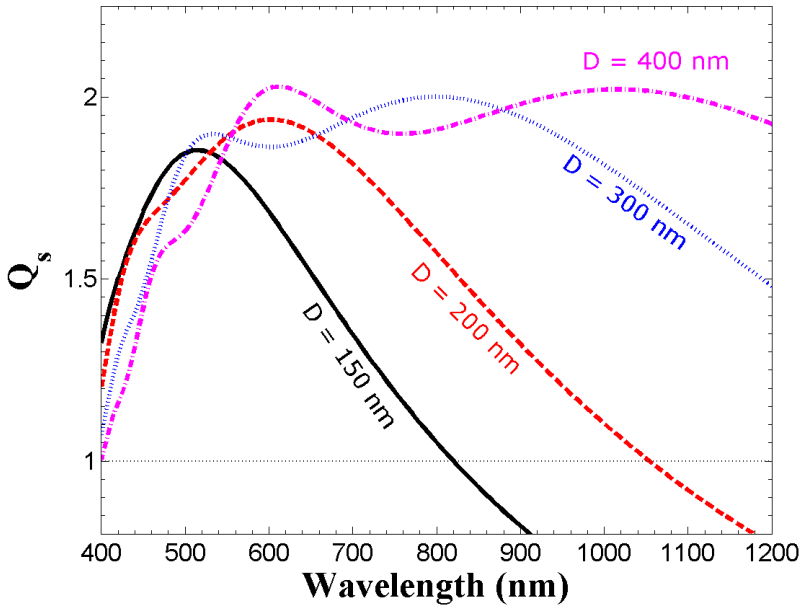

Figure 4.8. Scattering efficiencies of spherical SiO_2 particles embedded in c-Si at various diameters and wavelengths.

of the solar spectrum. However, larger nanospheres will also tend to displace the active semiconductor material in a fixed slab of c-Si, thereby reducing the overall absorption efficiency of a solar cell. We also note that larger spheres would tend to induce significant electrical effects such as larger spreading resistance due to current funneling, but such matters are not part of this investigation.

4.4.2 Simulation Results

To demonstrate the effectiveness of embedded dielectric nanoparticles, let us begin with a diameter of $D = 200$ nm, a depth of $z_0 = 150$ nm, and a pitch of $p = 400$ nm (≈ 20 % area coverage). The absorption spectra for this geometry are plotted in Figure 4.9 and compared to the baseline cell. Two key features are apparent from the simulation data. The first is that light injection into the c-Si layer is almost entirely unchanged by the presence of the embedded spheres underneath the ARC (-0.46 % in the total value). Second, we find that the total light absorption within the top 1.0 μm of the c-Si has been increased by 5.18 %. This tells us that the function of the ARC is nearly independent of any events occurring within the c-Si, and that the embedded spheres are introducing significant path-length enhancement to the incident radiation. We can even visualize this process directly by plotting the electric field profile within the active layer. Figure 4.10 also shows the

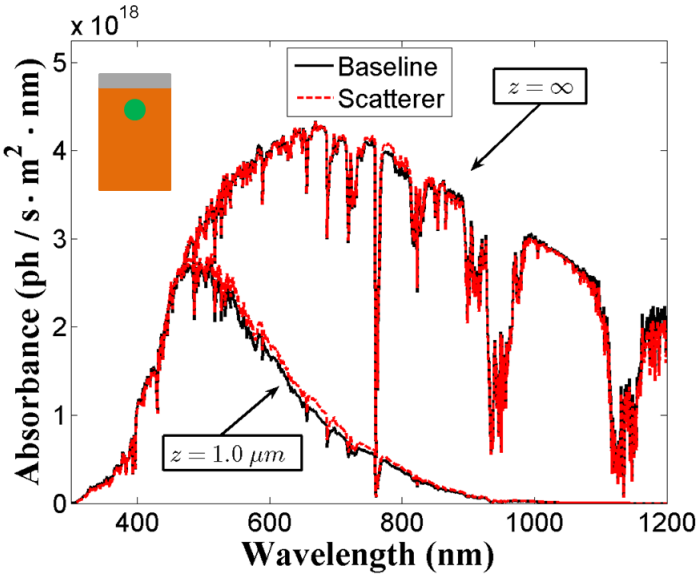

Figure 4.9. Absorption spectrum for a $D = 200$ nm sphere of SiO_2 embedded $z_0 = 150$ nm below the ARC with an array pitch of $p = 400$ nm. Absorption gain in the top 1.0 μm of the c-Si is 5.2 %.

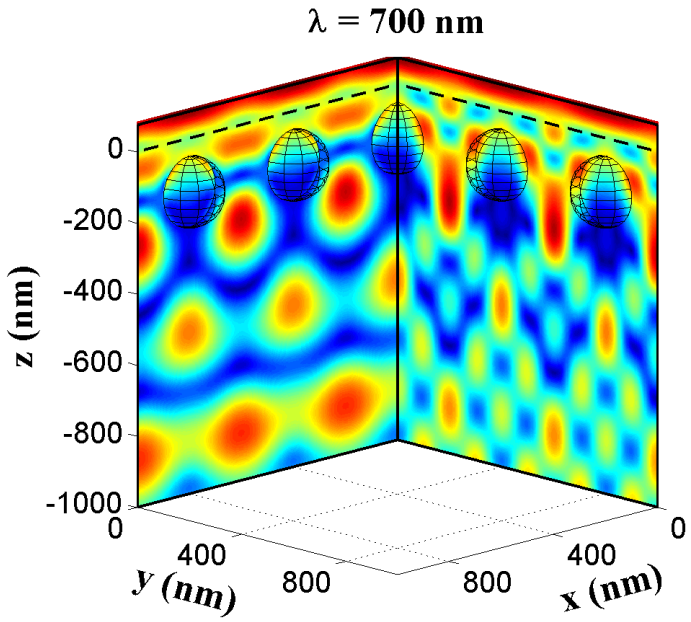

Figure 4.10. Electric field magnitude along two planar cuts at wavelength $\lambda = 700$ nm. Incident field polarization is $\hat{\mathbf{x}}$.

normalized electric field magnitude along two planar cuts at a wavelength of $\lambda = 700$ nm with an incident polarization along $\hat{\mathbf{x}}$. The presence of so many nodes and anti-nodes in the field profile is a direct manifestation of the off-normal scattering that is occurring as a result of the embedded nanospheres.

Due to the intense anti-nodes in the field intensity profile, it is tempting to suppose that a second sphere placed below the original should further scatter light and add to the overall absorption gain of the model. To test this hypothesis, a second sphere was inserted at $z_0 = 650$ nm and simulated under identical conditions. The resulting spectrum is plotted in Figure 4.11 and produces a 9.6 % absorption gain relative to the baseline. Another variation of interest is the SiO_2 hemisphere placed at the surface of the device as illustrated in Figure 4.12. Such a geometry could be produced via oxidation of selected areas through well-established Si-processing techniques for obtaining interfaces with low recombination velocity. The resultant absorption gain for this geometry was found to be 3.5 %. Though similar in principle to surface texturing, the feature size here is sub-wavelength and therefore advantageous in a thin-film device.

4.4.3 Grating and Coupling Effects

As stated previously, using periodic boundary conditions is equivalent to the simulation of an infinite array of particles. It is therefore worth asking how much of the efficiency improvement can be ascribed to the array structure, how much is caused by individual particle scattering, and how coupling interactions between adjacent particles affect performance. These questions begin to be answered in Figure 4.13, which shows efficiency gain as a function of particle density. At sparse densities ($< 10^9$ particles/cm^2), the inter-particle spacing is much greater than the wavelength in Si and well-outside the scattering cross-section. Each nanoparticle in this regime is therefore an effectively isolated scatterer. Under such ideal conditions, the scattering enhancement of each new particle adds a linear contribution to the net photon absorption within the cell, as is evidenced by the nearly linear slope below 10^9/cm^2. The diminishing return in cell efficiency enhancement above 10^9/cm^2 can then be understood by the overlap of scattering cross sections, which effectively reduces the power scattered laterally by each nanoparticle. Similar physics is at play in the peaking of the efficiency enhancement of metallic nanoparticle arrays. However, the scattering cross sections are larger for metallic arrays on resonance, and so the effects peak at lower areal density.

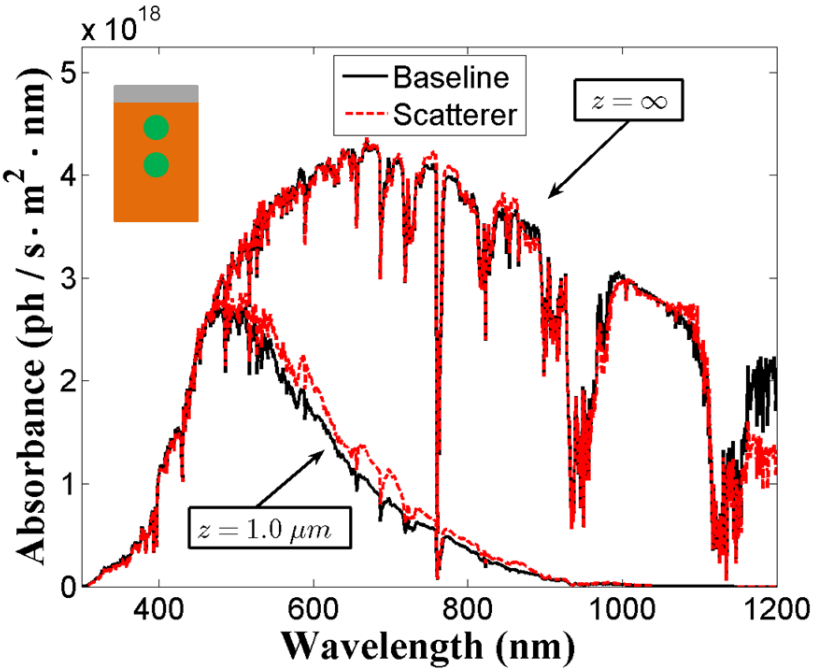

Figure 4.11. Absorption spectra for two stacked spheres placed at $z_0 = 150$ nm and $z_0 = 650$ nm. Absorption gain in the top 1.0 μm of the c-Si layer is 9.6 %.

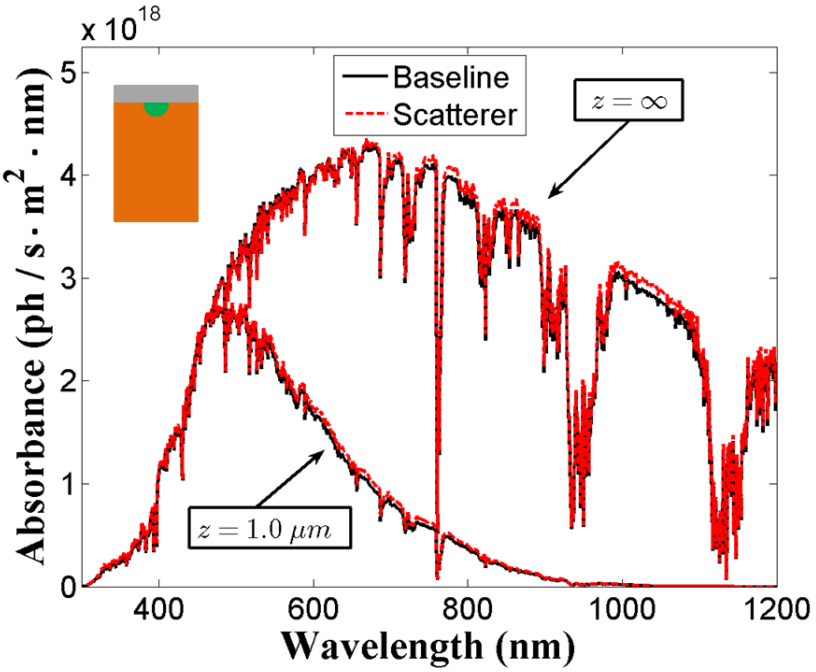

Figure 4.12. Absorption spectra for a half-sphere of SiO_2 embedded at $z_0 = 0$. Absorption gain in the top 1.0 μm of the c-Si layer is 3.5 %.

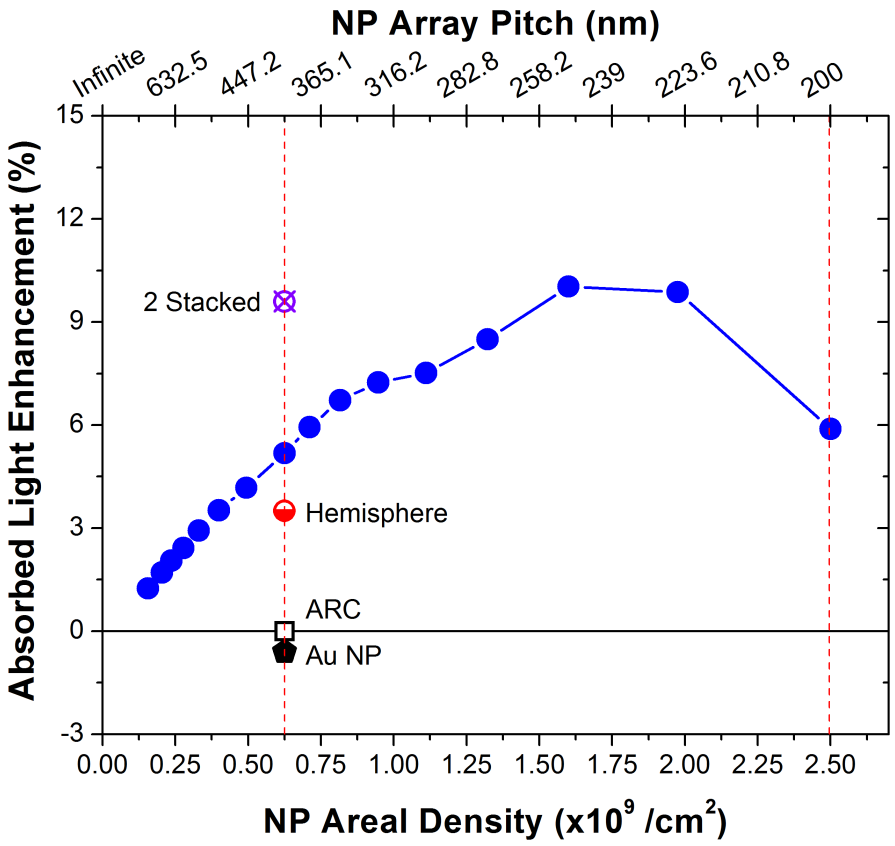

Figure 4.13. Efficiency trends versus particle density for periodic arrays of $D = 200$ nm of SiO_2 embedded in c-Si at a depth of $z_0 = 150$ nm. The points along the red vertical line at 6.25^8 /cm^{2}2 (400 nm spacing) summarize the absorption changes for the other geometries discussed in this chapter. At 2.5×10^9/cm^2 (200 nm), the dielectric spheres touch.

CHAPTER 5

DESIGN PRINCIPLES FOR LIGHT TRAPPING WITH EMBEDDED DIELECTRIC NANOSPHERES

This chapter is an expansion on the analysis from the previous chapter by considering a solar cell of finite thickness with an aluminum back contact. Adding a back contact introduces waveguide effects that were absent in the earlier analysis, which focused solely on the effects of embedded scatterers within a silicon half-space. The analysis in this chapter is therefore focused much more on the performance of a practical solar cell design rather than on the strict interaction of embedded particles with the antireflective coating (ARC). The results from such analysis can reveal useful information about the underlying physics of such a device and the optimal design parameters which maximize light absorption within the active layer.

5.1 Baseline Solar Cell Model

Depicted in Figure 5.1, the baseline cell consists of a 1.0 μm slab of crystalline silicon (c-Si) with an aluminum back-contact. The choice of 1.0 μm is somewhat arbitrary, and is only intended to serve as a representative model for a generic thin-film device. At the surface of the c-Si layer is a 75 nm slab of Si_3N_4 to serve as the ARC. Periodic boundary conditions were placed at the x- and y-boundaries to mimic the effects of an infinitely periodic unit cell. A perfectly-matched layer (PML) was placed 400 nm above the ARC to model a medium with infinite thickness. Because the skin-depth of aluminum is less than 50 nm for the entire visible spectrum, a simple, perfect electrically conducting (PEC) boundary was placed 200 nm below the back contact interface to remove the computational complexity of an extra PML. We also neglected the effects of doping on the dielectric properties of the c-Si layer, which are insignificant in the context of this work for wavelengths below 1200 nm. Simulations were again performed using the finite-difference time-domain (FDTD) run through the Lumerical software package [35].

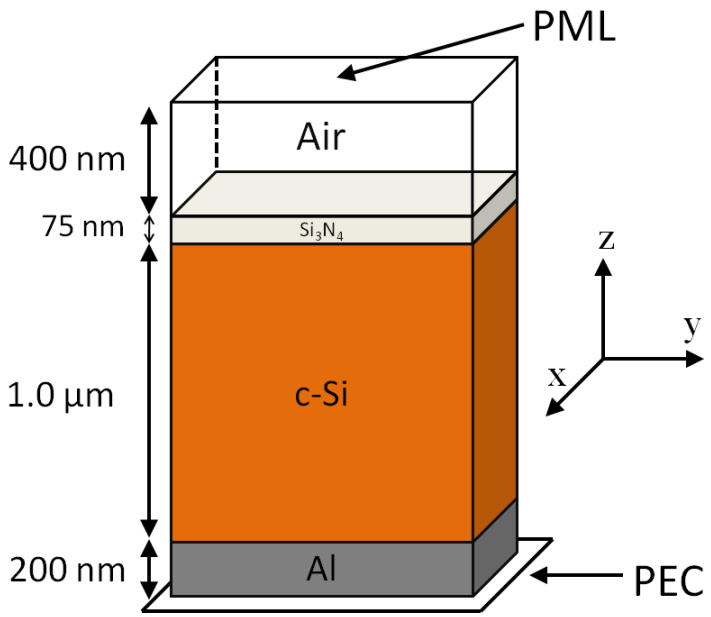

Figure 5.1. Baseline solar cell simulation model. The FDTD boundary conditions are periodic along x and y, mimicking an infinite array of cells. The top boundary above the cell is a PML while the bottom boundary is a PEC just below the back Al contact.

The output of interest from a given simulation is the absorption factor $A(\lambda)$, defined as the fraction of incident power that is absorbed within the c-Si layer at a specified free-space wavelength λ. Once the absorption factor is determined for a given model, the primary figure of merit is the solar flux absorbance $S(\lambda)$, which is defined as the absorption factor weighted by the AM 1.5 photon flux $\Phi_0(\lambda)$ [17]:

$$S(\lambda) = A(\lambda)\Phi_0(\lambda) \ . \tag{5.1}$$

Note that the units of $S(\lambda)$ are given by photons $\cdot\, \mathrm{s}^{-1} \cdot \mathrm{m}^{-2} \cdot \mathrm{nm}^{-1}$. The short-circuit current density J_{sc} is therefore related to the integral of $S(\lambda)$ times the internal quantum efficiency IQE(λ):

$$J_{sc} = q \int_0^{\lambda_g} S(\lambda)\, \mathrm{IQE}(\lambda)\, d\lambda \ , \tag{5.2}$$

where $q = 1.602 \times 10^{-19}$ C is the electron charge and $\lambda_g = 1120$ nm is the bandgap wavelength of c-Si. Thus, if the IQE were a known function, any simulation output could be used to compute J_{sc} under ideal AM 1.5 illumination. However, the focus of this dissertation is strictly limited to photon capture within the cell, which is equivalent to calculating J_{sc} under the assumption that IQE $= 1$ over all wavelengths below λ_g. Letting J_0 indicate the

total number of available photons below λ_g, we may further define the *spectrally integrated absorption efficiency* (IAE) using [62]

$$\text{IAE} = \frac{J_{sc}}{J_0} \ . \tag{5.3}$$

An example simulation output for the baseline geometry is depicted in Figure 5.2. Note that dielectric functions for each material were obtained from sampled data in Ref. [34]. Using analytical calculations derived from the analysis in Chapter 2, it is straightforward to verify that the simulation error is ≤ 1 %. For reference, the incident AM 1.5 photon flux is also plotted along with the ergodic limit for a 1.0 μm film of c-Si. For the sake of visual clarity, the data in the figure has been smoothed by an 8-point moving average (actual calculations were performed only on unsmoothed data).

Assuming perfect IQE, the IAE for the baseline cell was found to be 32 %. Without the ARC, the absorbance curve exhibits strong Fabry-Perot resonances and gives an IAE of only 23 %. The value of a simple ARC is therefore significant in a thin-film solar cell, and any practical light-trapping scheme should strive to be competitive with this baseline level of efficiency. For comparison, the ergodic limit is also plotted, which yielded an IAE of 77 %. This illustrates the untapped potential of simplistic thin-film designs due to poor light trapping. Another important feature is the dramatic decline in the ergodic absorption

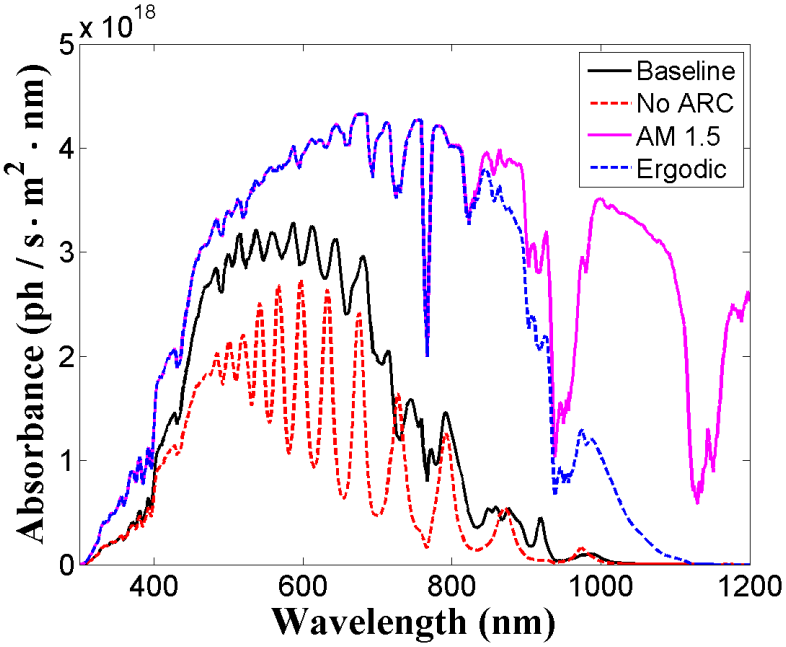

Figure 5.2. $S(\lambda)$ computed by the baseline model. Without the ARC, the c-Si layer absorbs 26 % fewer photons and exhibits strong Fabry-Perot resonances. For comparison, the total AM 1.5 spectrum and the ergodic limit are also plotted.

limit at wavelengths above 900 nm. This behavior is due to the exponential decline in $\alpha(\lambda)$, which effectively decays to zero near λ_g.

5.2 Embedded Dielectric Nanospheres

The experimental cell is identical to the baseline, but with a spherical SiO_2 nanoparticle embedded within the active c-Si layer. Depicted in Figure 5.3, the simulation model is defined by a specific depth z_0 below the c-Si surface, a diameter D, and a pitch p of the repeating array. As a demonstration case, Figure 5.4 plots $S(\lambda)$ for a $D = 200$ nm sphere at depth $z_0 = 450$ nm, and a pitch of $p = 375$ nm. These parameters represent nearly optimal values for light-trapping derived from the analysis in this paper. For reference, the baseline cell is also plotted to emphasize the increase in absorption that occurs across the solar spectrum. This gain is due solely to the increased path-length of the incident radiation as it scatters off the embedded nanoparticles and couples into guided or weakly radiating modes within the cell. Numerical integration of the two curves yields a 23.4 % gain in the IAE due to the presence of the embedded nanoparticles (IAE = 39 %).

5.3 Parametric Sweeps

This section summarizes the results from a set of sweeps over the three design parameters. For all three conditions, the slab thickness was fixed to a value of 1.0 μm. The first sweep was designed to infer the optimal height placement within the active layer for the embedded nanospheres. For starting parameters, we chose a diameter of $D = 200$ nm and an array pitch of $p = 400$ nm. These values were determined from the analysis in the previous chapter as a feasible starting point for this investigation. For the first sweep, particle depth was varied from $z_0 = 100$ nm to $z_0 = 900$ nm. Figure 5.5(a) summarizes the results, which show that the ideal height placement for embedded nanoparticles is within 300–500 nm. We can also see that gain drops off sharply as the particles are moved closer to the back contact of the cell.

Similar analysis to this has been performed by using an analytical model of scattering from embedded dipoles [62]. However, such analysis assumed incoherent scattering between particles and was only limited to wavelengths above 900 nm. Dielectric spheres are also poorly approximated as simple dipoles as the wavelength drops below 800 nm. One must further account for the fact that the c-Si layer is much more lossy in this regime as well. When the entire spectrum is taken into account, the simulated absorption gain tends to increase in effectiveness as a function of distance and then diminish when the particle

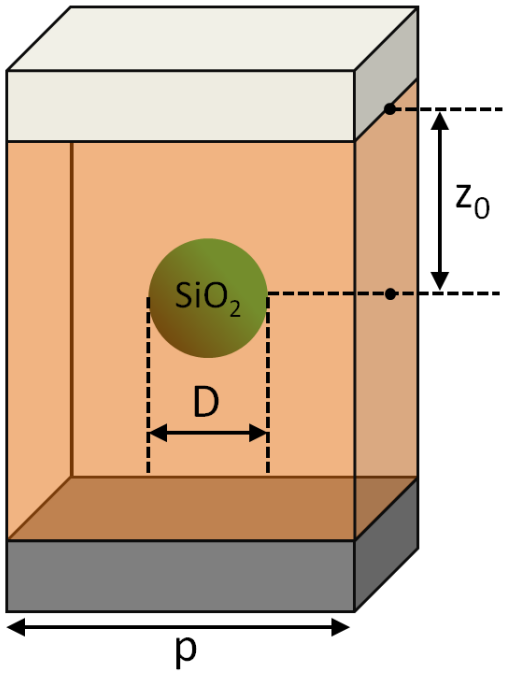

Figure 5.3. Geometry of the embedded NP array. The embedded sphere possesses a characteristic diameter D, array pitch p, and height z_0.

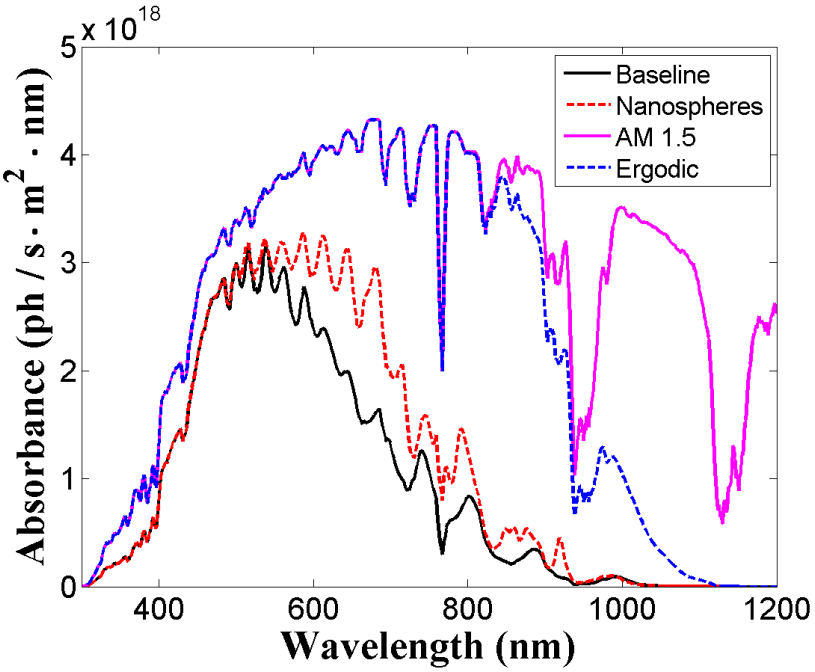

Figure 5.4. Absorption spectrum for $D = 200$ nm, $z_0 = 450$ nm, and $p = 375$ nm. Total absorption gain due to the embedded nanoparticle array is 23.4 %.

moves beyond 500–600 nm from the back contact. This is in stark contrast with previous analysis, which exhibited oscillations in absorption gain as a function of particle depth.

If we neglect the effects of secondary scattering between spheres, then we may understand this behavior in terms of the interaction between the embedded spheres and their image currents induced within the back contact of the cell. This problem has been analyzed in great detail by Johnson in 1992 [63], and helps to guide our understanding for this problem. It is known that as a sphere is moved away from a conducting plane, the scattering amplitude of the system tends to increase while the far-field pattern exhibits strong grating lobes. These grating lobes are especially desirable, as they imply a more isotropic pattern of scattered radiation as opposed to the predominantly forward scattering of an isolated sphere. However, absorption within the c-Si layer itself also tends to reduce the strength of the induced image, thereby counteracting the desirable effects of its presence as the sphere is moved away. Consequently, there is a diminishing return on the absorption gain as the spheres are moved beyond 600–700 nm from the back contact. In practice, we may also expect that the exact distance will vary heavily with such factors as the contact reflectance, the attenuation of the active layer, and secondary scattering between particles in the array.

Next, we varied the diameter of the spheres while fixing the embedded depth at $z_0 =$ 500 nm. The array pitch was also varied according to $p = 2D$ in order to maintain a constant area coverage ($\approx$ 19.6 %). The data points are plotted in Figure 5.5(b), which shows a weak absorption gain for small diameters that quickly grows to a strong peak within the 175–250 nm range. Larger particles then exhibit a marked decline in absorption gain that approaches $\approx$ 10 % when the spheres exceed 500 nm in diameter.

This behavior is indicative of a trade-off between scattering efficiency and the displacement of active semiconductor material. As was demonstrated by the Mie calculations in the previous chapter, Q_s tends to grow more broadband as the particle diameter is increased. Consequently, larger spheres tend to couple more of the incident spectrum into guided or weakly radiative modes. However, larger particles also physically displace the volume of active c-Si material that can absorb light. Furthermore, not all wavelengths of the visible spectrum can be absorbed with equal effectiveness in a 1.0 μm slab of c-Si. As Figure 5.4 shows, the ergodic limit drops off sharply for wavelengths above 950 nm. This is due to the fact that c-Si is extremely low-loss in this regime, and even large path-length enhancements result in relatively small gains in photon absorption. As a result, there is a diminishing return in light absorption that occurs as scattering efficiency includes more of the longer wavelengths. A particle with $D = 400$ nm is therefore worse than one with

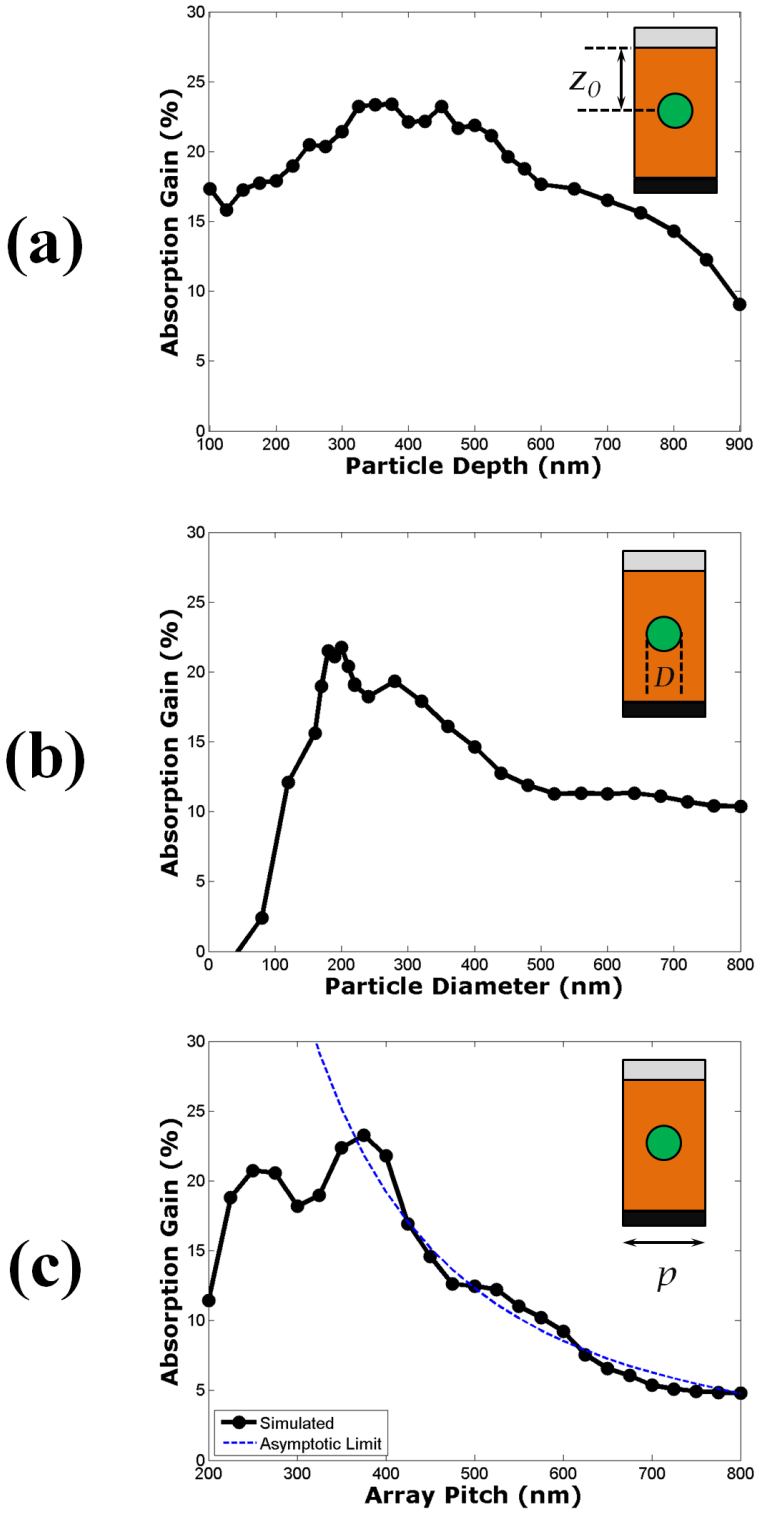

Figure 5.5. Variation of absorption gain with (a) particle depth for a fixed diameter of $D = 200$ nm and fixed pitch $p = 400$ nm; (b) particle diameter for a fixed depth of $z_0 = 500$ nm and increasing pitch $p = 2D$; (c) array pitch for a fixed height of $z_0 = 500$ nm and a fixed diameter $D = 200$ nm.

$D = 200$ nm because the path-length enhancements in the near-IR spectrum are offset by the displacement of active material.

It is possible to qualitatively model these effects to a first order by defining a generic *gain metric* $U(D)$ based on the above parameters. We therefore postulate a functional form for U given by

$$U(D) = V(D) \int_0^{\lambda_g} Q_s(D, \lambda) A_N(\lambda)\, d\lambda \ . \tag{5.4}$$

In essence, this expression simply weighs the competing factors that contribute to absorption gain and then averages them across the visible spectrum. Higher values for U indicate stronger absorption gain while lower values indicate weaker absorption gain. The function $Q_s(D, \lambda)$ is then given by the scattering efficiency of an SiO_2 sphere with diameter D embedded in c-Si. This term accounts for the relative ability of the embedded nanosphere to effectively scatter light within the solar cell. The function $A_N(\lambda)$ is then given by the value

$$A_N(\lambda) = 1 - e^{-4\alpha(\lambda)w} \ , \tag{5.5}$$

which is the absorption factor of a model-N slab with thickness $w = 2.0$ μm (representing both the forward and reverse path-lengths through the slab). This parameter serves to account for the relative ability of the c-Si medium to absorb light at a given wavelength. Finally, the function $V(D)$ is given by

$$V(D) = 1 - \frac{\pi D}{24w} \ , \tag{5.6}$$

which is the volumetric displacement factor that accounts for the displacement of active c-Si material by the embedded dielectric spheres.

Figure 5.6 shows the gain metric calculated from Equation (5.4) using the given model parameters. Comparison with Figure 5.5(b) reveals several similar features, including a sharp rise over small diameters and a slow decay over larger values. The peak value even agrees very well with the simulation results, indicating an ideal diameter in the 200–250 nm range. This strongly supports our simple model of competing first-order influences that ultimately determine absorption gain. The only second-order influences we have not accounted for are the secondary scattering events that occur between particles. These likely account for much of the chaotic variation on top of the overall trends.

In the final series, we varied the pitch of the array using $D = 200$ nm and $z_0 = 500$ nm, with results summarized in Figure 5.5(b). For a sparse array with large pitch, the absorption gain asymptotically approaches zero as the pitch approaches infinity. For a dense array with

$p < 400$ nm, there is a brief region of oscillation that converges on the point where individual particles are finally touching.

The explanation for this behavior can be broken down into contributions from multiple effects. For $p\alpha(\lambda) \gg 1$, the amplitudes of both radiation modes and guided modes will decay by the time they encounter any secondary scatterers. As a consequence, each embedded particle acts in isolation from all other particles, and gain in IAE is approximately linear with the area coverage. This effect is consistent with the case of a planar half-space demonstrated in Ref. [28] and the previous chapter. If we further note that area coverage is defined as $\pi r^2/p^2$, then asymptotic gain in IAE may be expressed as

$$G = m_0 \frac{\pi r^2}{p^2} \quad (p\alpha(\lambda) \gg 1) \ , \tag{5.7}$$

where $m_0 \approx 0.98$ is a constant scale factor that must be empirically determined from the data. A large value for m_0 implies very strong scattering by individual particles while a small value implies very weak scattering. This curve is superimposed into Figure 5.5(c) to demonstrate the limiting behavior at large p.

When the spheres are brought close together, photons begin to experience greater secondary scattering events. For weakly radiating modes, this can lead to greater coupling into the desirable guided modes and yield greater IAE. However, guided modes can also experience coupling back into radiation modes, thereby reducing the IAE. The dominance of each case depends heavily on array pitch and wavelength, as illustrated by the semi-chaotic

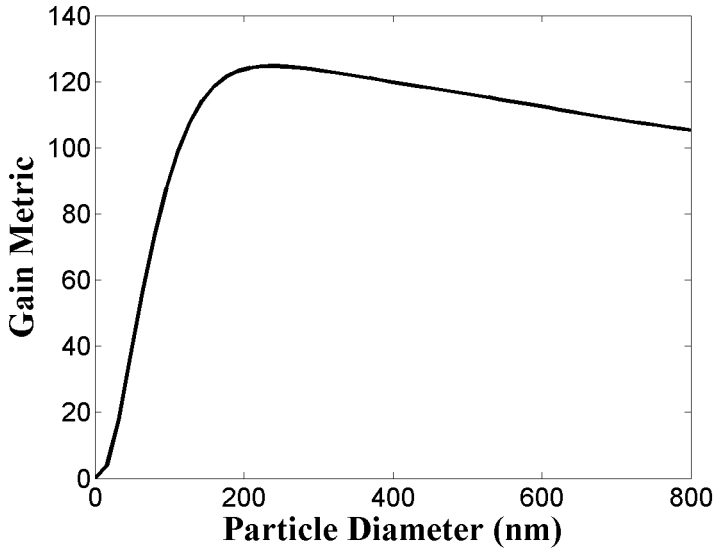

Figure 5.6. Absorption gain metric computed from Equation (5.4) for SiO_2 spheres embedded in a 1.0 μm slab of c-Si.

absorption spectrum of Figure 5.4(b). Such behavior is likewise present in the other two data sets and contributes to a small degree of chaotic variation on top of any general trends. For very closely-packed arrays, the displacement of active material also becomes a significant factor contributes to a net decline in the IAE.

A final effect is the overlap of scattering cross-sections σ_s from adjacent particles. If we define an equivalent scattering diameter using $D_s = 2\sqrt{\sigma_s/\pi}$, then Mie calculations of Q_s indicate that $D_s \approx \sqrt{2}D$ over much of the spectrum. This implies a critical distance of 283 nm for $D = 200$ nm spheres. Intuitively, one can think of this as two spheres attempting to scatter the same photons. Particles within this distance therefore experience a rapid decline in IAE. This behavior is also consistent with our results in Chapter 4, which showed a large drop in absorption gain as the particles nearly touched. The ideal array pitch is therefore within the range of 350–400 nm, which places the embedded particles as close as possible without displacing too much active material or inducing secondary scattering into radiation modes.

5.4 Discussion

In principle, we expect the embedded nanoparticle concept to be compatible with alternative choices for the design of a photovoltaic device. For example, the active semiconductor need not be exactly 1.0 μm, and could even be replaced with amorphous silicon rather than crystalline. Alternative choices for the back contact, such as Ag/ZnO, are also potential options, and overall light absorption will likely be improved with higher back-surface reflectance. Another interesting possibility is the use of embedded nanovoids rather than dielectric nanospheres [64, 65, 66]. In such cases, it is likely that absorption gain will still experience qualitatively similar behavior to the results summarized in this work.

Further gains may likewise be achieved through the use of more complex scattering geometries. For example, nanospheres comprised of a gold core encapsulated by an SiO_2 shell can be readily manufactured [67] and possess much higher scattering efficiencies than pure SiO_2 spheres alone. It is also possible that the SiO_2 shell could maintain the same low recombination interface of a pure SiO_2 sphere by acting as a diffusion barrier for the gold core. Figure 5.7 shows the scattering efficiencies of a $D = 200$ nm sphere of Au embedded in c-Si under varying thicknesses of an SiO_2 shell. These calculations were likewise performed using standard Mie theory [60], though the extinction coefficient of the c-Si medium has been neglected for the core/shell case. This assumption is reasonably accurate in c-Si for wavelengths above $\lambda = 500$ nm.

As the Mie calculations show, Au nanospheres possess a much higher scattering efficiency than SiO_2 spheres over much of the visible spectrum. However, a shell thickness of only $t = 10$ nm is enough to completely negate this advantage. This behavior strongly indicates that much of the scattering efficiency of a core/shell geometry is dominated by the shell itself. We therefore chose to simulate a shell thickness of $t = 5$ nm as a reasonable trade-off between the need for high scattering efficiency and a thick diffusion barrier. Figure 5.8 summarizes the simulation results for an embedded core/shell nanoparticle using the same parameters as those in Figure 5.4 ($D = 200$ nm, $z_0 = 450$ nm, $p = 375$ nm). After subtracting Ohmic losses within the Au-core, the gain in IAE was found to be 30.5 %. This demonstrates that further gains in IAE are possible when the embedded nanospheres possess higher scattering efficiency than pure SiO_2.

Although we have assumed a perfectly periodic lattice in our simulation models, such a feature is not essential for absorption gain in a real device. Whether scattering is coherent or not, any feature that redirects the incident radiation from normal propagation must result in a subsequent path-length enhancement. From Figure 5.5(c), we can also infer that coherent scattering effects should only be significant when the mean particle spacing is less than $p = 400$ nm, since this is the region where absorption gain strongly deviates from the ideal assumption of perfectly isolated scatterers. Rigorous analysis has also shown that asymmetric structures are actually superior to periodic structures in terms of optimal light trapping [20, 23]. Consequently, we expect to see significant absorption gains whether the embedded particles are ordered or disordered.

Upon examination of the absorption spectrum of Figure 5.4(b), it is apparent that overall absorption efficiency falls far short of the ergodic limit. This is in contrast with other forms of light-trapping that have demonstrated near-optimal absorption efficiencies via surface texturing [20, 23]. However, the trade-off to such performance is often paid in the form of tight restrictions on the necessary specifications of the surface features. If such structures could be manufactured cheaply in an industrial scale, then surface texturing would certainly possess an economic advantage. Embedded nanospheres therefore have a practical advantage in terms of lower restrictions to their geometries in exchange for a modest gain in light absorption. We leave it as a topic of further research to directly compare the economic distinctions and light-trapping performance between various design concepts.

Although we have focused this work solely on the light-trapping properties of embedded nanospheres, it is important to remember that such structures will have many electrical

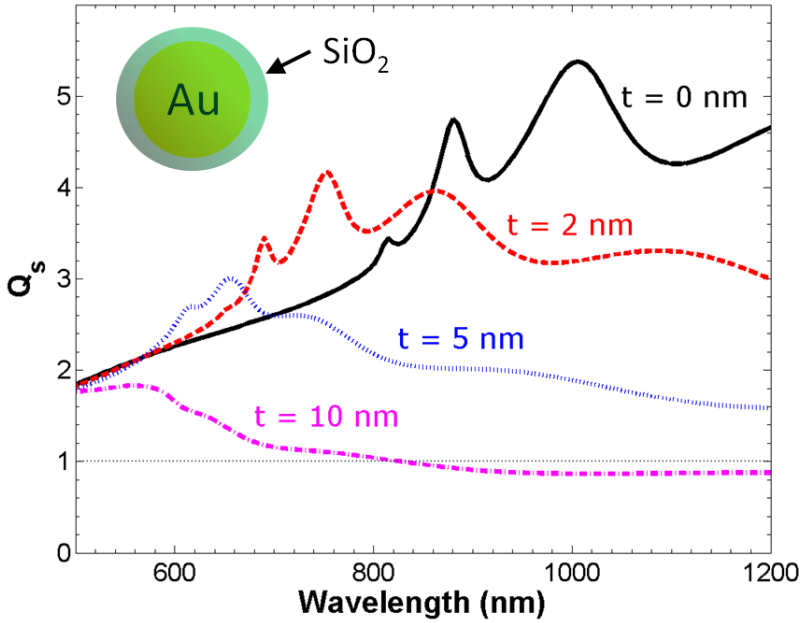

Figure 5.7. Scattering efficiencies for a $D = 200$ nm sphere of Au embedded in c-Si. The Au is enclosed in a spherical shell of SiO_2 of varying thickness t.

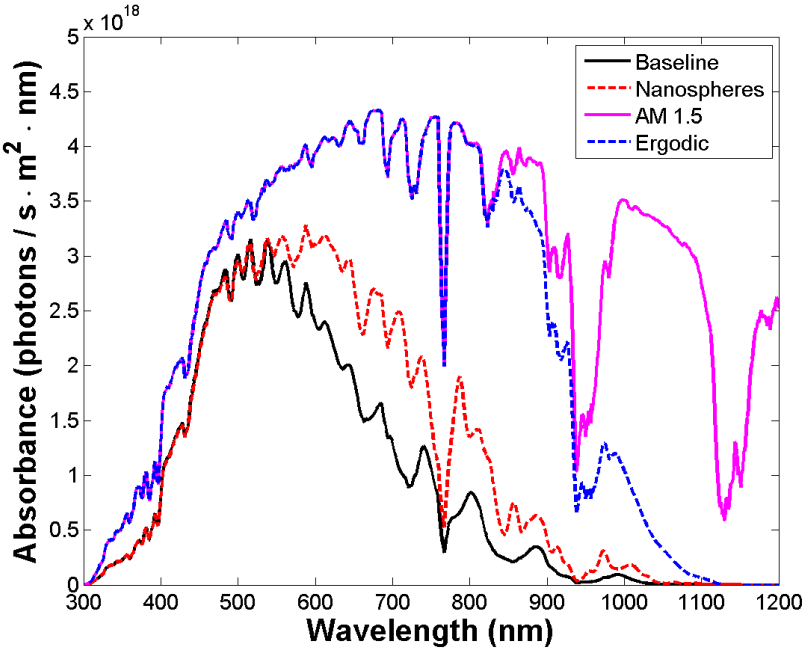

Figure 5.8. Spectral absorbance for an Au-core and SiO_2 shell with $t = 5$ nm embedded in a c-Si solar cell using $D = 200$ nm, $z_0 = 450$ nm, and $p = 375$ nm.

consequences for the photovoltaic device as a whole. For example, although Nunomora, et al [30], reported a net gain of 16 % to short-circuit current density after embedding SiO_2 spheres, the fill factor also fell from 0.84 to 0.76. This was attributed to the increase in series resistance caused by the dielectric spheres as they blocked charge transport within the cell. It is also fairly certain that these nanoparticles will induce extra recombination within the cell. However, by placing the particles at the tunnel junctions between the individual cells of tandem and multijunction structures, this recombination could actually help to increase the efficiency of a device. Designers should therefore take care to account for such issues while searching for a globally optimal layout of embedded particles.

CHAPTER 6

A COMPARISON OF LIGHT TRAPPING BETWEEN SURFACE TEXTURES AND EMBEDDED DIELECTRIC NANOSPHERES

This final chapter compares surface texturing against embedded dielectric nanospheres for their affects on absorption gain in a thin silicon film. The inspiration for this work stems from a report by Nunomura, et al, in which a gain of 16 % was reported in a thin silicon solar cell after embedding spheres of SiO_2 within the active layer [30]. However, the process of embedding the dielectric spheres also introduced texturing along the surface of the cell. This was likely due to the nature of chemical vapor deposition, which tends to conform material to the underlying features as it is deposed from above. Because surface textures are also known to generate path-length enhancements, it is an open question whether the resultant absorption gain was due primarily to the embedded spheres, the conformal surface texturing, or a combination of both. Thus, the goal of this chapter is to compare the light-trapping performance between these two mechanisms and determine which one likely dominated the absorption gains within the device.

6.1 Simulation Models

The baseline geometry for this chapter is similar to that of the previous chapter. Namely, a 1.0 μm layer of crystalline silicon (c-Si) is topped by a 75 nm antireflective coating (ARC) made out of Si_3N_4. However, instead of an aluminum back contact, the base of the model has simply been replaced with perfect electric conductor (PEC) as illustrated in Figure 6.1. This greatly simplifies the comparison and removes any concern over energy loss within the back contact.

The embedded dielectric nanoparticle is defined by a solid sphere of SiO_2 embedded directly below the ARC. For this series of simulations, the particle geometry will be specified by a diameter of $D = 200$ nm, a depth of $z_0 = 200$ nm, and a pitch of $p = 1.0$ μm. These

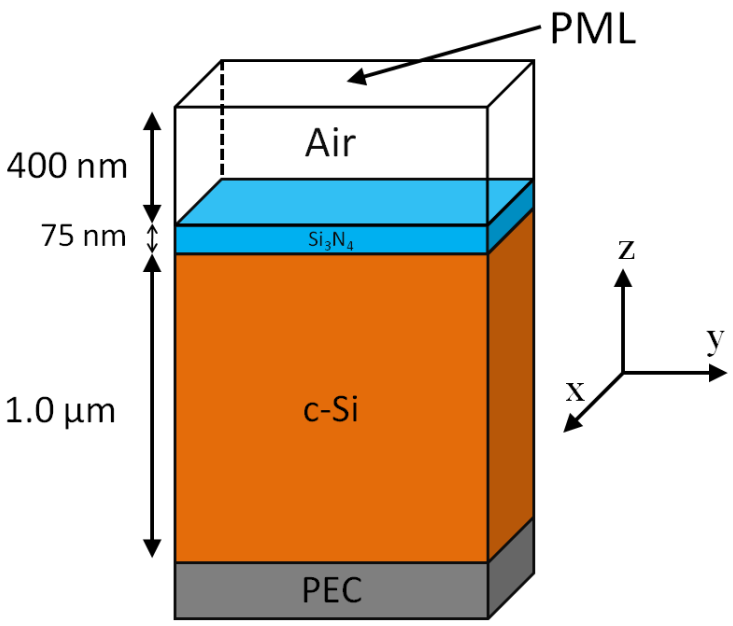

Figure 6.1. Baseline geometry for referencing absorption gain.

are intended to crudely approximate the same parameters utilized by the experimental cell in [30], which were determined using an atomic force microscope.

To model the surface texture above the solar cell, we shall assume a conformal coating of material over the nanoparticle itself. This is intended to model the sort of surface texturing that might occur from such growth processes as chemical vapor deposition. The texture itself is therefore defined by a sphere with a radius R_1 that is centered on the SiO_2 nanoparticle. The ARC is then another spherical shell deposited atop the c-Si layer with radius R_2. Such a geometry is depicted in Figure 6.2, with $R_1 = 400$ nm and $R_2 = 475$ nm.

The experimental simulations were broken down into four cases that are all summarized in Figure 6.3. The baseline simulation is represented by the solid black curve, which includes no surface texturing and no embedded nanoparticles. The first test simulation then embeds the SiO_2 nanoparticles ("NP") but does not include any surface texturing. The next simulation applies the surface texture to the cell ("ST") but does not embed any nanoparticles. The final simulation then includes both the embedded nanoparticles and the surface texturing ("NP & ST"). For reference, the ergodic limit is also plotted in the figure.

Using numerical integration on the simulation curves, the absorption gains relative to the baseline were found to be:

$$\text{NP} = 5.18\ \% \ ,$$
$$\text{ST} = 47.4\ \% \ ,$$
$$\text{NP \& ST} = 52.3\ \% \ .$$

Clearly, these results indicate a strong bias toward the surface texture as a means of enhancing light absorption within the c-Si layer. Such results are also consistent with the analysis of the previous chapter which indicated an absorption gain on the order of $\approx 5\ \%$ for embedded spheres of SiO_2 at an array pitch of $p = 1.0\ \mu$m.

One possible explanation for the strong bias toward surface texturing is that the extra volume of material introduced by the texture itself is artificially inflating the observed absorption gains. We can test this by also comparing against a planar design like the baseline geometry, but with a c-Si layer that is 1.2 μm thick instead of 1.0 μm. This adds a layer of c-Si as thick as the conformal surface texture but with a planar geometry. However, despite the fact that such a geometry adds even more absorber material than the surface texture does, the absorption gain relative to a 1.0 μm geometry is only 7.44 %. It is therefore apparent that the light scattering effects of the surface texture indeed dominate the absorption gain of the system.

An alternative geometry is the pyramidal texture illustrated by the model in Figure 6.4. Pyramids are also a common surface texture in photovoltaics that are usually implemented by etching along the crystal planes in c-Si. We may therefore define the surface geometry by a height h and a base length specified by the array pitch p. The spectral absorbance curves are plotted in Figure 6.5 using $h = 200$ nm and $p = 1.0\ \mu$m. Absorption gains were then calculated as

$$\text{NP} = 5.18\ \% \ ,$$
$$\text{ST} = 38.4\ \% \ ,$$
$$\text{NP \& ST} = 46.5\ \% \ .$$

These results indicate once again that surface texturing is much more potent than embedded spheres of SiO_2.

As a final experiment, let us examine the model depicted in Figure 6.6. This model represents the tandem solar cell design employed by Nunomura et al in their experiments. The top layer is a 75 nm ARC made out of indium tin oxide (ITO). Directly underneath the ARC was a 350 nm layer of amorphous silicon (a-Si), followed by a 1.0 μ layer of c-Si. The next layer is a thin, 35 nm region of zinc-oxide (ZnO) all resting atop a silver

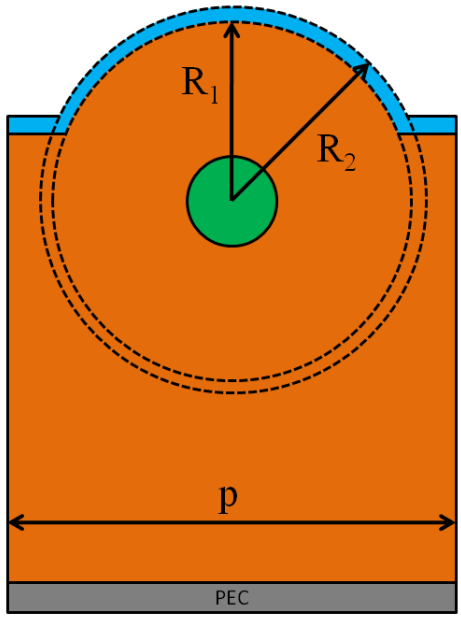

Figure 6.2. Model geometry for the embedded dielectric nanosphere and surface texture above. $R_1 = 400$ nm, $R_2 = 475$ nm, and $p = 1.0$ μm.

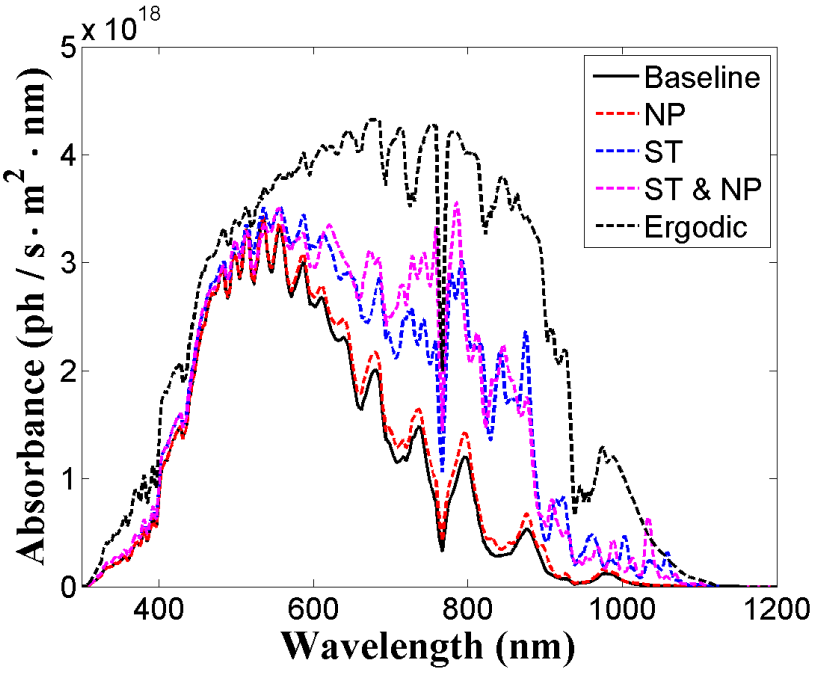

Figure 6.3. Absorption spectra comparing embedded nanospheres with surface texturing. Absorption gains relative to the baseline are 5.18 % (NP), 47.4 % (ST), and 52.3 % (NP & ST).

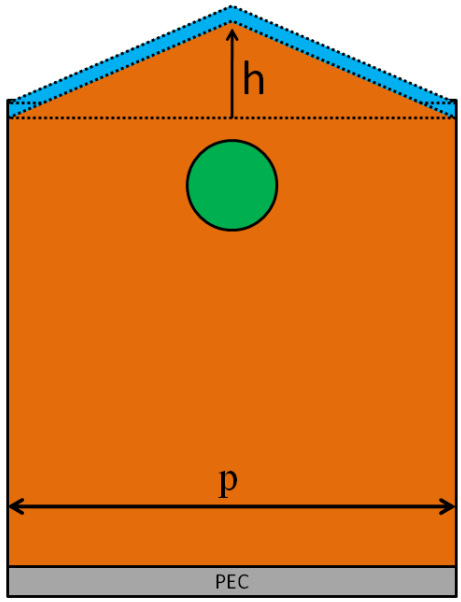

Figure 6.4. Model geometry for the embedded dielectric nanosphere and pyramidal surface texture.

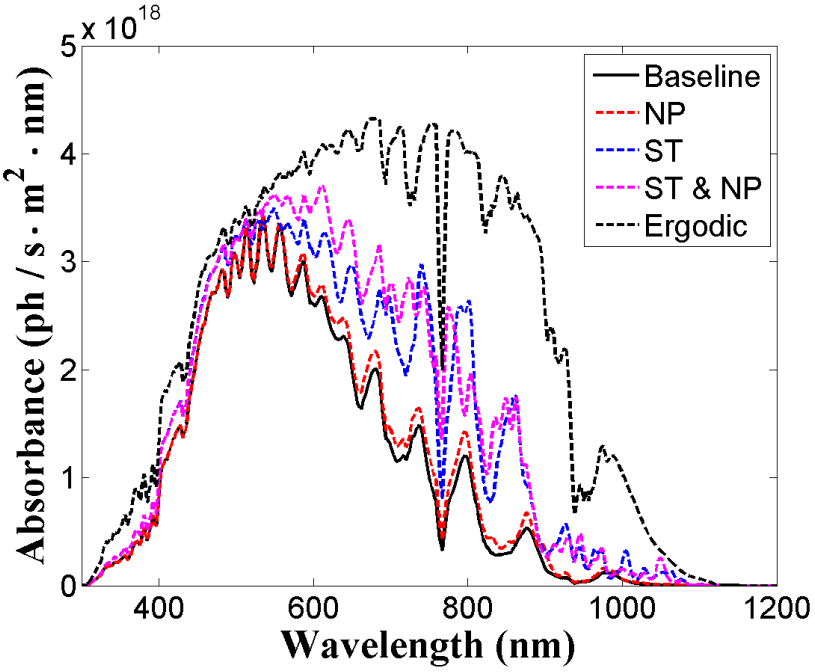

Figure 6.5. Absorbance spectra for the pyramidal surface texture. Absorption gains relative to the baseline are 5.18 % (NP), 38.4 % (ST), and 46.5 % (NP & ST).

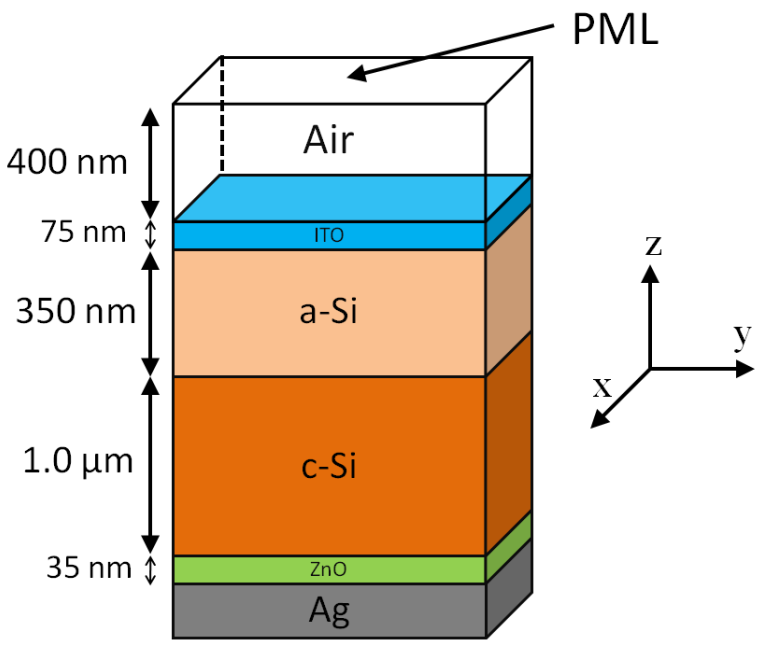

Figure 6.6. Baseline geometry for a tandem solar cell representing the design by Nunomura, et al.

(Ag) back contact. The embedded spheres of SiO_2 and accompanying surface texture are illustrated in Figure 6.7. The mean radius of the embedded spheres was given by $r = 130$ nm, with deposition accomplished through spin-coating. The a-Si layered was then generated afterward by using standard vapor deposition techniques. Our assumption for the model is that deposition of the a-Si layer will conform to the height of he embedded spheres. As noted earlier, analysis with an atomic force microscope revealed a peak-to-peak elevation of the surface texture that was approximately 200 nm with a periodicity of roughly 1.0 μm. The simulation model was therefore specified by a hemispherical surface texture with $R_1 = 480$ nm and $R_2 = 555$ nm.

Figure 6.8 shows the resulting absorbance spectra generated by the simulation model. The absorption gains relative to the baseline were found to be

$$\text{NP} = 2.0\ \% \ ,$$

$$\text{ST} = 14.9\ \% \ ,$$

$$\text{NP \& ST} = 15.1\ \% \ .$$

Although these values are not quite as dramatic as the earlier cases, it is again apparent that the surface texturing dominates the absorption gain in the device. The lower absolute values are likely due to the presence of the a-Si layer, which is much more strongly absorbing

than the c-Si layer and therefore more difficult to improve upon. It is also possible that variations between the simulated surface topology and that of the real device would account for further deviations.

6.2 Discussion

It is apparent from all three simulations that the surface texture has dominated the absorption gain of the solar cell when compared to embedded dielectric spheres. However, when viewed in a wider contest, such results should come as no surprise. Research into optimal surface texturing has revealed that properly engineered surfaces can meet, and even partially exceed, the Yablonovitch limit of light absorption [20, 23]. Based on the analysis of the previous chapter, it is also apparent that embedded nanospheres alone can only provide a gain in IAE of only ≈ 25 % at best. We may therefore conclude that surface texturing is likely the most promising candidate for maximizing light absorption in thin film solar cells.

Although surface textures appear to trap light much more efficiently than embedded nanoparticles, there is still some value in exploring the embedded nanoparticle concept further. In practice, manufacturing a precise surface texture at the scale of hundreds of nanometers is currently a difficult prospect. As the experiments of Nunomura, et al, show, the spheres themselves can actually be used to generate a crudely engineered surface texture. This is a direct result of the conformal nature of material deposition over the top of the spheres. So although the contribution by the spheres to overall light trapping may be relatively small, the spheres themselves can apparently help to generate a surface texture with reasonable control. It is even possible that alternative choices of the material properties can help to significantly improve absorption efficiency in the cell while still preserving the conformal surface texture above. These questions may have tremendous value in the ongoing search for an economically viable solution to the problem of mass-production of efficient photovoltaic devices. However, such topics must wait for further investigation into light trapping with thin silicon films.

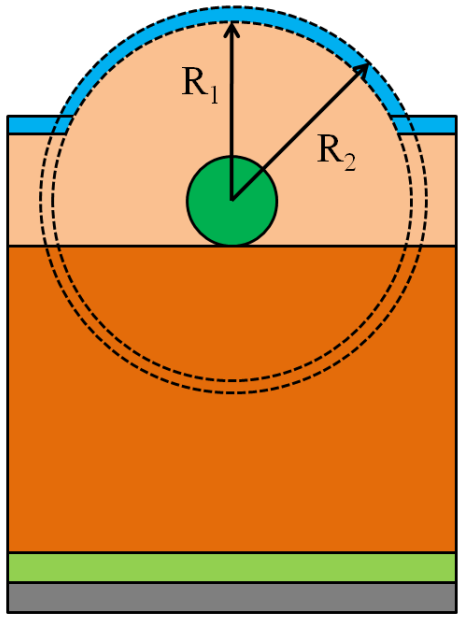

Figure 6.7. Geometry for the embedded dielectric nanosphere and surface texture using the Nunomura design. Simulation parameters are the same values as those in Figure 6.2.

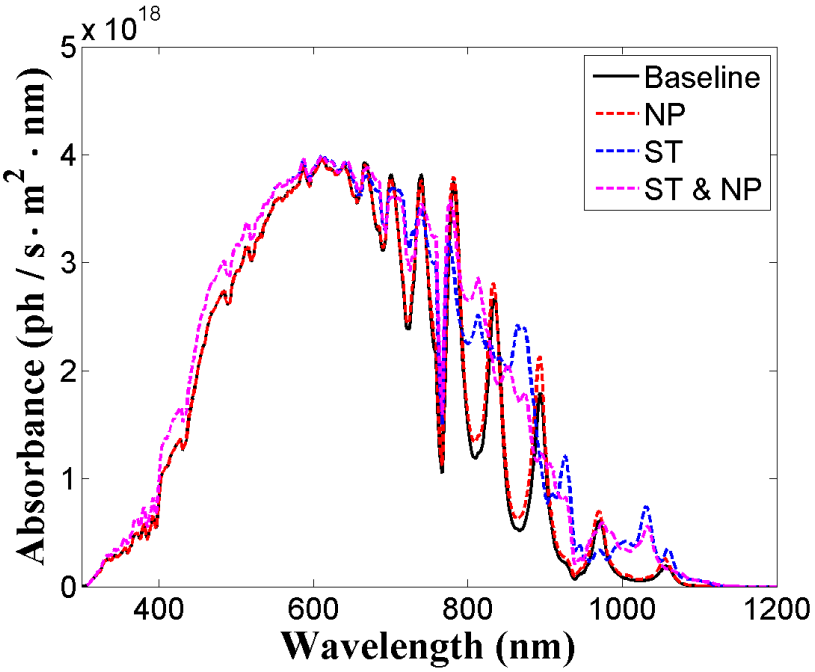

Figure 6.8. Absorbance spectra for the Nunomura cell. Absorption gains relative to the baseline are 2.0 % (NP), 14.9 % (ST), and 15.1 % (NP & ST).

CHAPTER 7

CONCLUSION

The primary goal of this work was to explore the theoretical limits to light trapping in thin silicon films through the utilization of embedded dielectric nanoparticles. This was explored primarily through the use of numerical simulation using the finite-difference time-domain (FDTD) method. It was found that embedded spheres of SiO_2 do not significantly interfere with the function of anti-reflective coatings (ARC's), thereby scattering light only after it has been maximally injected. It was also found that under optimal conditions, embedded SiO_2 spheres can produce nearly 24 % improvement in the spectrally integrated absorption efficiency of a simple 1.0 μm silicon solar cell.

A secondary goal of this research was to compare various light trapping schemes against one another in performance. Using FDTD simulations on a select set of solar cell models, it was found that surface texturing is the clearly dominant winner at producing absorption gain. Embedded dielectric spheres can produce significant absorption gains as well, but are likely better utilized as avenues for producing surface texture than they are as light scatterers. Plasmonic nanoparticles placed along the surface of the cell tended to perform worst of all, and generally cannot even compete well against a simple nitride ARC.

A final contribution from this research has been a full-field solution to the problem of guided wave propagation in a lossy thin film. The solutions are applicable for the generalized three-layer dielectric waveguide under any arbitrary combination of gain or lossy materials. Although this problem has been examined to varying degrees in the past, this seems to be the first time such a model has been applied to the study of photovoltaic devices. Further contributions have been made in the fundamental analysis of path-length enhancement in simple planar structures as well as the introduction of the concept of equivalent deflection angle.

The following sections discuss some of the potential avenues for future research inspired by the results of this dissertation.

7.1 Model Internal Quantum Efficiency

Throughout this dissertation, we have focused entirely on the effects of light absorption in lossy materials and completely neglected the effects of carrier generation or recombination. Without these effects, our models may as well be nothing more than sophisticated heating elements rather than efficient photovoltaic devices. So although we have demonstrated enhanced photon capture using surface textures and embedded SiO_2 nanospheres, it is unknown what effects these features will have on the internal quantum efficiency. For example, Nunomura, et al [30] noticed a reduction in fill factor from 0.84 to 0.76 after embedding silica nanospheres in a tandem cell. This result was attributed to increased series resistance by the presence of the particles, but no models exist to theoretically predict such an outcome. Other unknown effects include the nature of recombination at the interface between SiO_2 nanospheres and the ambient c-Si medium. If not designed properly, it is very likely that the absorption gain due to light trapping will be offset by the internal recombination loss induced by the spheres. Further recombination effects are known to occur along the features of a surface texture as free carriers migrate toward any metal contacts. It is therefore an important part of the modeling procedure to account for the eventual motion of excited photocarriers within the active semiconductor layers of a solar cell.

7.2 Generalized n-Layer Waveguide Solution

Although the general solution to the n-layer waveguide problem was initially solved in 1995 [46], there has been relatively little application of this theory to the field of photovoltaics. Due to the complex and transcendental nature of the eigenvalue problems, it is also an active field of research just to efficiently solve for the propagation constants of the system itself [68, 69]. So although we have a complete solution for the asymmetric three-layer problem, such a model is limited only to very crude and simplified designs like the bare c-Si cell backed by aluminum. Even the addition of a simple nitride ARC would convert the problem into a four-layer system, and it is uncertain what effect this would have on the modal properties of the device. We are also interested in the modal structure of tandem designs like the Nunomura cell, which would require a five-layer solution in order to properly model.

7.3 Targeted Mode Excitation

One of the more potentially useful discoveries from this work is the fact that high-order modes tend to possess much higher longitudinal absorption than low-order modes. This is

especially true for the extra loss-guided modes that only exist in lossy films. Coupled mode theory tells that it is possible to couple energy into these modes, though it is uncertain if one could deliberately engineer a feature that specifically targets them. Further research is necessary in order to understand the nature of mode coupling in lossy waveguides and possible methods to exploit targeted modal excitation.

7.4 Experimental Demonstration

The results presented in this dissertation have so far all been theoretical and numerical. The next step is therefore to devise an experimental demonstration of the new discoveries. Many of these should be relatively simple to do if given the right resources. A demonstration of enhanced absorption in a tandem solar cell using embedded dielectric nanospheres would serve to replicate the results of Nunomura, et al [30]. A further variation on this design would be to polish the front surface after depositing SiO_2 spheres inside. This would serve to demonstrate the differences in light trapping due to the embedded spheres versus surface textures. If possible, it would be especially useful to design a structure that specifically targets the lossy modes of a thin film device. A numerical demonstration of this using FDTD would be a good first step, but a demonstration with a real-world cell would be especially noteworthy.

APPENDIX A

OPTICAL CONSTANTS OF COMMON MATERIALS

The nature of electromagnetic wave propagation through a given isotropic material may be readily characterized by a value known as the *complex index of refraction*, written as

$$\tilde{n} = n + j\kappa \ . \tag{A.1}$$

The real part n determines the phase velocity of a uniform plane wave as it propagates through the medium. The imaginary component κ, called the *extinction coefficient*, determines the attenuation of that wave. These values vary with frequency but are usually expressed as a function of free-space wavelength λ in the optical regime.

Effective simulation of a given material relies heavily on knowing the refractive index over the spectrum of interest. It is therefore important to document the sources for such information in any scientific study. Such information can often be difficult to acquire and assemble into a single archive, so this appendix will serve as a reference for all of the material properties simulated throughout this dissertation.

In practice, it is important to note that the optical constants of any given material sample will invariably contain some deviation from its standard reference values. For some materials like crystalline silicon, this is usually not a problem since efficient processing techniques can lead to a strong uniformity across many samples. For other materials like amorphous silicon or indium-tin-oxide, relatively strong deviations can occur through the presence of impurities in the bulk material or variations in the physical process by which the material was grown. These references therefore represent only the models that were used throughout this dissertation for the purposes of numerical simulation, and one should exercise caution when applying such data to the real world.

The Lumerical software package contains a large built-in library of material properties. Most of these libraries were taken from the *Handbook of Optical Constants of Solids* [34], which is a standard reference for this kind of information. However, several materials were used throughout this research that are not readily available, but must be carefully

searched out in the literature. One very helpful online resource for such information is the Refractive Index Database [70], which offers instant refractive data access as well as links to the references from which they were derived.

A.1 Crystalline Silicon

Crystalline silicon (c-Si) is the semiconductor of choice and the current industry leader in the photovoltaics market. The optical constants of c-Si are well-studied and may be highly uniform across any given sample or set of samples. It is also an indirect bandgap semiconductor, causing the extinction coefficient to rapidly decay to zero as $\lambda \rightarrow 1120$ nm. This behavior is difficult to model numerically, since the FDTD algorithm attempts to apply a polynomial curve fit to optical constants. As a result, simulated absorption in c-Si will often be greater than the true value since the curve fit tends to bias in favor of greater values for κ. Fortunately, this effect can be corrected by applying the techniques outlined in Chapter 4.2.1. Figure A.1 summarizes the optical constants for c-Si obtained from [34].

A.2 Amorphous Silicon

Amorphous silicon (a-Si) is a cheap alternative to purely crystalline silicon. The optical constants of a-Si are very similar to c-Si, but generally possess a much higher absorption coefficient. The diffusion length in a-Si is also much shorter than c-Si, making charge collection a much more difficult process. As a result, a-Si tends to suffer from much weaker internal quantum efficiency than c-Si. It is also common to hydrogenate the a-Si sample, which is usually denoted as a-Si:H. The exact concentration of hydrogen, coupled with variation between growth processes, can frequently lead to wide deviation in the exact optical properties of a given sample. The optical band gap is also highly dependent on the process used to grow the a-Si and tends to vary between 1.5–1.8 eV. However, the exact values themselves are not so important as finding a reasonably representative data set that covers the entire visible spectrum. Figure A.2(a) summarizes the optical constants for a-Si obtained from [70].

A.3 Aluminum

Aluminum (Al) is a cheap metal that serves well as a back or front contact in silicon solar cells. However, junction spiking is a Figure A.2(b) summarizes the optical constants for Al obtained from [34].

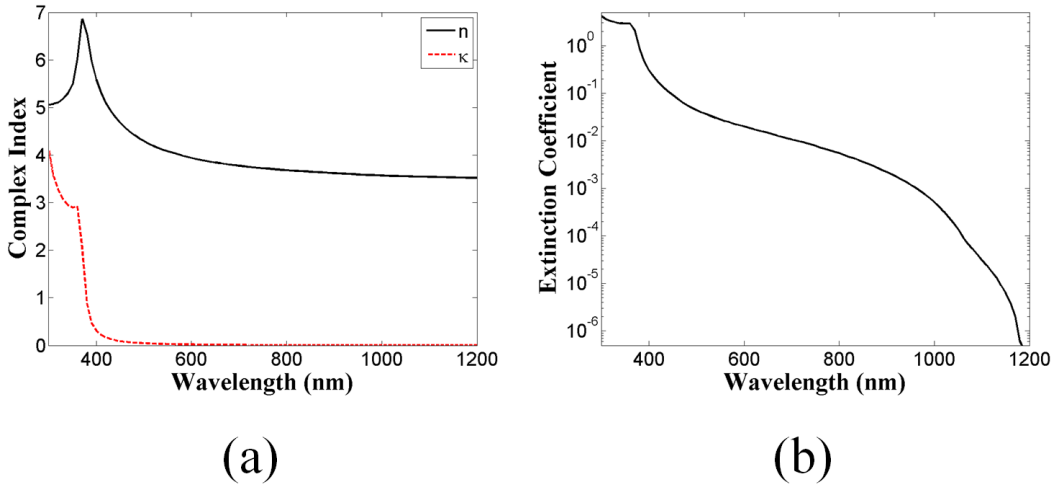

Figure A.1. (a) Optical constants for crystalline silicon. (b) Extinction coefficient plotted on a logarithmic scale.

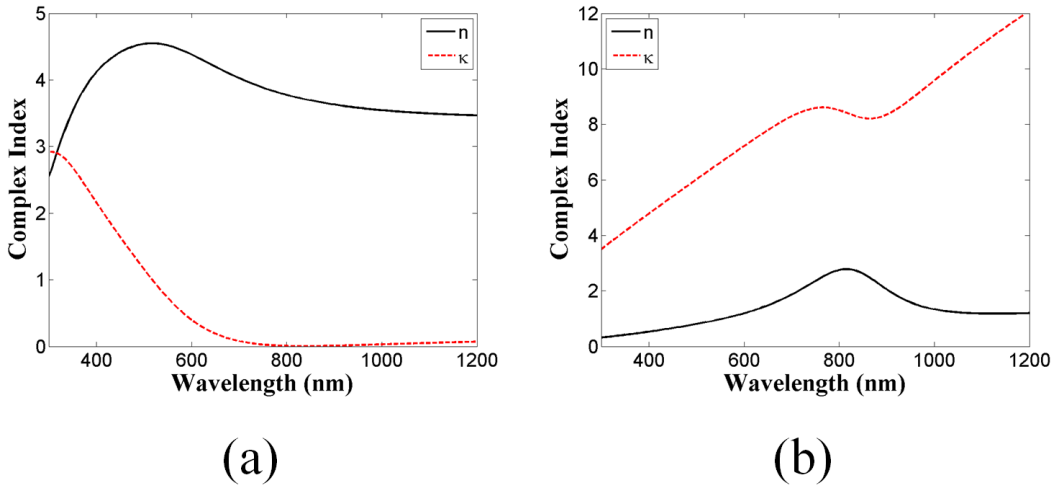

Figure A.2. Optical constants for (a) amorphous silicon and (b) aluminum.

A.4 Silicon Nitride

Silicon nitride (Si_3N_4) is a simple compound used in silicon photovoltaics to make anti-reflective coatings. The reason for this is because the real index of refraction for c-Si is very nearly $n = 4$ across much of the visible spectrum while Si_3N_4 is very nearly $n = 2$. This allows Si_3N_4 to be used as an efficient quarter-wave transformer for matching the optical impedance between c-Si and air. Si_3N_4 also has the added advantage of being almost perfectly lossless across the visible spectrum. Typical nitride thicknesses are usually between 60–80 nm for optimal capture of the peak in the AM 1.5 spectrum. Figure A.3(a) summarizes the optical constants for Si_3N_4 obtained from [70].

A.5 Silicon Dioxide

Silicon dioxide (SiO_2), also commonly referred to as *fused silica*, is a very common glass insulator that can be easily grown on c-Si wafers. SiO_2 has the advantage of being an extremely efficient electrical insulator as well as being optically lossless. When engineered correctly, SiO_2 can also occupy the many dangling bonds that typically serve as recombination centers at the interface to a c-Si lattice. This makes SiO_2 a natural choice for exploring the light-trapping behavior of embedded nanoparticles within the active semiconductor layer. Figure A.3(a) summarizes the optical constants for SiO_2 obtained from [34], which are virtually constant ($n \approx 1.5$) across the entire visible spectrum.

A.6 Indium Tin Oxide

Indium tin oxide (ITO) is a special compound known as a *transparent conductor*. This means that ITO is virtually lossless at optical wavelengths, but quickly becomes highly conductive at RF wavelengths and DC. ITO is therefore very popular in photovoltaics as a surface contact layer because it allows visible light to pass through but still serves as an efficient contact for gathering electrical current. ITO is much like a-Si in that the exact optical constants depend heavily on the process by which it was made. Figure A.4 summarizes the optical constants for ITO obtained from [71].

A.7 Gold (Au) and Silver (Ag)

Gold (Au) and silver (Ag) are part of a class of elements known as *noble metals*. The key utility behind these materials is their strong electrical conductivity at optical wavelengths, even when compared against aluminum. This makes these materials ideally suited for light trapping due to the strong scattering efficiencies they possess. Ag is also a popular material for generating good electrical contacts with c-Si and frequently appears at the front or rear

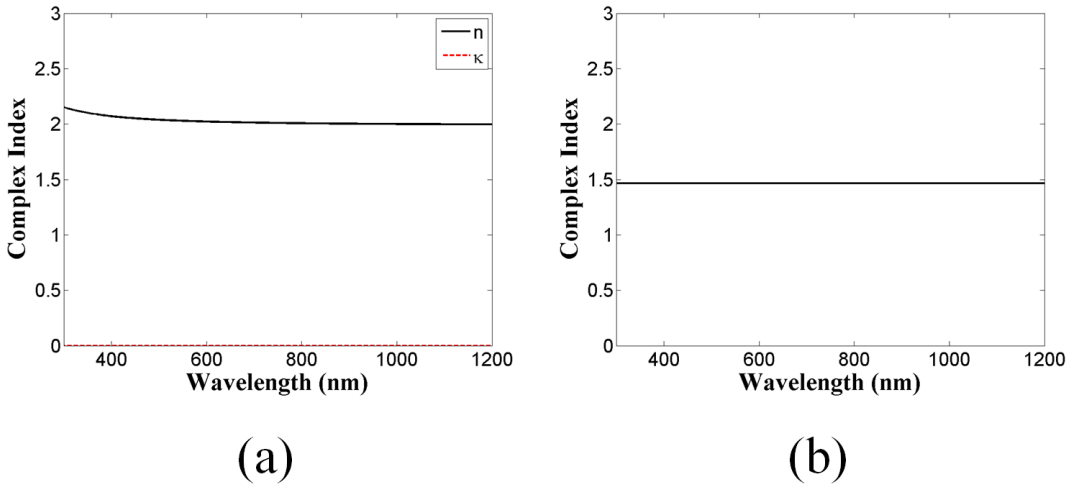

Figure A.3. Optical constants for (a) silicon nitride and (b) silicon dioxide.

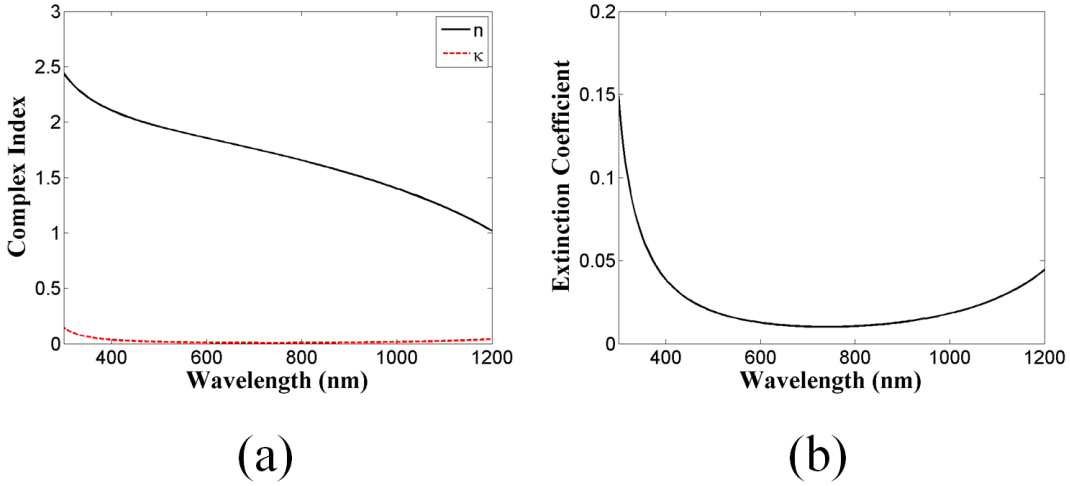

Figure A.4. (a) Optical constants for indium tin oxide. (b) Extinction coefficient only.

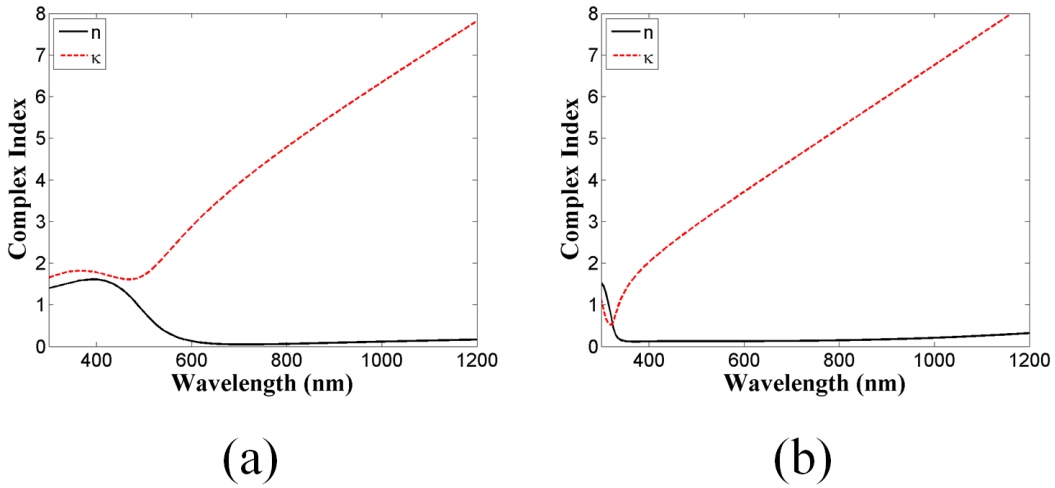

Figure A.5. Optical constants for (a) gold and (b) silver.

contact of a solar cell. Figure A.5 summarizes the optical constants for Au and Ag obtained from [34].

APPENDIX B

SOURCE CODES

The research presented in this dissertation required the development of several specialized numerical source codes. All programs were written in Matlab [72] and are presented below. Note that each file contains an extensive header to describe the underlying function as well as the last date of modification.

B.1 Layered Medium Solver

This code solves for the amplitudes and wavenumbers in a planar stratified medium. The algorithm for this code is summarized in Chapter 2.

```
%==========================================================================
%
%   Solve for Plane-Wave Propagation Amplitudes in a Layered Medium.
%
%       [A B] = solve_layered_medium(n,D,L0,THi,TE) computes the complex
%   wave amplitudes (A,B) for plane-wave propagation in a layered medium
%   that is excited from the (-z) direction.
%
%   n   = Vector of complex indices of refraction for each region.
%   D   = Vector of distances for each planar boundary (m).  Note that each
%           element in D needs to be increasing.
%   L0  = Free-space wavelength of excitation (m).
%   THi = Angle of incidence relative to z-axis (rads).
%   TE  = Boolean flag to indicate either transverse electric (TE == 1) or
%           transverse magnetic (TE == 0) polarization.
%
%       Note that for TE waves, the incident E-field is Y-polarized, and
%   all computed wave amplitudes are the E-FIELD amplitudes.  For TM waves,
%   (i.e.; TE == 0), the incident H-field is Y-polarized and all the wave
%   amplitudes are H-FIELD amplitudes.
%
%   [A B kx kz] = solve_layered_medium(...) also returns the X- and Z-
%   components to the wave-vectors in each region.  Note that due to
%   phase-matching, the kx component is identical for ALL REGIONS.  That
%   means kx is a single, scalar value, while kz is a vector of elements
%   representing each region.
%
%   [...] = solve_layered_medium(... , lossFactor) specifies a loss factor
%   for lossy media.  By default, this value is set to 1e-9.  Any region
%   that attenuates the incident wave by this much is the truncation point
%   for further reflections and transmissions beyond.  This measure greatly
%   helps to stabilize the algorithm in the presence of lossy media.  We
%   can certaintly make this value smaller, but it increases the risk of
```

```
%   numerical instability.
%
%                                SYSTEM GEOMETRY:
%
%                z = D(1)          z = D(2)  ...      z = D(M-1)
%                   |                 |                  |
%                   |                 |                  |
%                   |                 |                  |
%      A(1)         |      A(2)       |                  |    A(M)
%    ------->       |    ------->     |        ...       |  ------->        ^ +x
%                   |                 |                  |                  |
%                   |                 |                  |                  |
%    <-------       |    <-------     |        ...       |  <-------        |     +z
%      B(1)         |      B(2)       |                  |    B(M)          ------->
%                   |                 |                  |
%                   |                 |                  |
%                   |                 |                  |
%                   |                 |                  |
%      n(1)         |      n(2)       |        ...       |    n(M)
%                   |                 |                  |
%
%
%   FURTHER NOTES:
%
%        The computation assumes an incident plane wave propagating in the
%   +z-direction.  The angle of incidence (THi) is with respect to the
%   z-axis.  Given the system geometry, it should be apparent that for an
%   M-region system, there should be M-1 planar boundaries.
%
%        Another important note to keep in mind is the phase relationship
%   between the amplitudes in A and B.  Each field component is
%   phase-referenced against the planar boundary that INJECTS the field.
%   So for example, A(M) is phase-referenced against the z = D(M-1) planar
%   boundary.  This helps to make the computations more numerically stable,
%   as well as more meaningful when trying to calculate such parameters
%   like the transmittance into Region M.  The incident wave in Region 1 is
%   referenced against z = 0.
%
%        BEWARE: In theory, the values in D can be offest by any arbitrary
%   value.  However, I have not validated this code under anything other
%   than D(1) = 0.  The algorithm can certainly be tweaked to make this
%   work for arbitrary values, but has not yet been validated.  So just be
%   safe and assign D(1) = 0 whenever using this code.
%
%        Note that the imaginary component to the index can be either
%   POSITIVE OR NEGATIVE.  By the convention within this code, a POSITIVE
%   value for the imaginary index is LOSSY, while a NEGATIVE value
%   is AMPLIFYING.  BEWARE!  THIS CONVENTION IS NOT UNIVERSAL!  It is
%   therefore important to be sure that the imaginary index fits the
%   convention of this program.  Another way to think of this is that a
%   forward-propagating TE wave has the phasor/time-domain form:
%
%                E+(x,z)   = A * exp(+j(kx*X + kz*Z))
%                E+(x,z,t) = A * cos(kx*X + kz*Z - 2*pi*f*t)
%
%        Also note that overly lossy/amplifying media tend to behave in very
%   quirky ways.  The reason is because the computations become numerically
%   unstable and error quickly accumulates.  This makes the results
%   meaningless if the user attempts to push the materials too far.  For
```

```
%   purely lossy regions, this issue is stabilized by simply truncating the
%   waves after a certain point.  For regions with amplification, this gets
%   very tricky and the code will likely produce unreliable numbers if
%   pushed too hard.
%
%   This code has been validated against FDTD simulations for both TE and
%   TM cases at arbitrary incidence angle in a 4-layered system.  If any
%   bugs are found, please email the author.
%
%   REFERENCE:
%       J. A. Kong, "Electromagnetic Wave Theory," pp 385-397 (2000).
%
%   Note that I have made my own modifications to the notation and that I
%   have also neglected to include arbitrary magnetic media in the
%   solution.  I have also tweaked the derivation to make the output more
%   numerically stable from what Kong derives.  See chapter 2 in my PhD
%   dissertation for specific details.
%
%==========================================================================
%
%   James Nagel
%   Department of Electrical and Computer Engineering
%   University of Utah, Salt Lake City, Utah
%   nageljr@ieee.org
%   Copyright August 23, 2011


function [A,B,kx,kz] = solve_layered_medium(n,D,L0,THi,TE,lossFactor)

% Extract parameters from inputs.
M = length(n);          % Total number of regions.
k0 = 2*pi/L0;           % Free-space wavenumber (rad/m).
k = k0*n;               % Complex wavenumber in each region (rad/m).

% Instantaite forward and reverse amplitudes.  For TE polarization, the
% units are V/m.  For TM, the units are A/m.
A = zeros(M,1);         % Forward amplitudes.
B = zeros(M,1);         % Reverse amplitudes.

% Set the loss factor if not specified.  This helps to stabilize the
% algorithm when dealing with lossy media.  Any region where the E-field
% attenuates by this value is basically the cutoff point for all wave
% propagation beyond.
if nargin == 5
    lossFactor = 1e-9;
end

% Incident plane wave has unit amplitude.
A(1) = 1;

% x-components of wavenumbers.  These are all identical due to the
% phase-matching condition between boundaries.
kx = k0*n(1)*sin(THi);

% Square-root argument for the dispersion relation.
u = k.^2 - kx^2;

% z-components to the wavenumbers must all satisfy the dispersion relation
% within their respective media.
```

```
kz = sqrt(u);

%  Special case for solving the dispersion relation.  This represents an
%  incident wave from a lossy medium.  The square-root operator experiences
%  a branch cut under this condition that needs to be handled.
if ( real(u) < 0 ) & ( imag(u) < 0 )
    kz = -kz;
end

%  Check for length error on inputs.
if length(D) + 1 ~= M
    error('D not correct length.  Should be length(n) - 1.');
end

%  Check to make sure D is properly increasing.
if any(D < 0) || any(diff(D) < 0)
    error(['D must be positive and increasing.']);
end

%  Solve for the reverse-propagating wave in Region 1.  The recursion
%  algorithm for this is unconditionally stable for lossy systems.  See the
%  function description below for more details.
B(1) = solve_layered_reflection(n,kz,D,TE,1);

%=========================================================================
%  For the case where M>= 3, we have to be careful about directly applying
%  the propagation-matrix method.  Instead, begin with the numerically-
%  stable amplitudes in Region 1 and iterate through each region directly.
%  Do this by enforcing continuity at each boundary and by utilizing the
%  reflection/transmission coefficients at each interface.
%    When an extremely lossy region is encountered, just truncate the
%  series and assume all the wave amplitudes go to zero beyond it.  It will
%  not be perfectly accurate for a mixed gain/loss system, but such systems
%  are rarely encountered (if ever), and a highly-lossy system will become
%  much more numerically stable.
%=========================================================================
for m = 1:M-1

    %  Generate three z-distance references.  d0 is the z-value of the
    %  previous planar boundary.  d1 is the current planar boundary, and d2
    %  is the next planar boundary.

    %  For Region 1, the distance is referenced at z = 0.  Otherwise, use
    %  the previous distance value.
    if m == 1
        d0 = 0;
    else
        d0 = D(m-1);
    end

    %  This is true for all regions.
    d1 = D(m);

    %  For M-1, the "next" planar boundary does not exist.  Since B(M) is
    %  always zero, it makes no difference what value we use for d2.
    %  Otherwise, just use the next D-value.
    if m == M-1
        d2 = 0;
    else
```

```
        d2 = D(m+1);
    end

    %  Solve for exponential coefficients.  For lossless systems, these
    %  will just be phase factors.  For gain/lossy systems, these can
    %  easily lead to VERY LARGE or VERY SMALL numbers.
    am = exp( +1j*kz(m)   *(d1 - d0) );
    bm = exp( -1j*kz(m+1)*(d1 - d2) );

    %  This is the key step that stabilizes the algorithm.  Extremely lossy
    %  regions should effectively kill the signal, but numerical error
    %  tends to creep in and introduce energy where there should not be
    %  any.  So when am is a very small number, that is our clue to end the
    %  series and assume that no more signals get through.  So simply set
    %  everything beyond this point to zero and terminate the loop.
    if abs(am) < lossFactor
        B(m:end)   = 0;
        A(m+1:end) = 0;
        break;
    end

    %  Solve for normalized indices with respect to each planar boundary.
    %  These are needed in order to properly calculate the reflection
    %  coefficients.
    m12 = n(m+1)/n(m);      %
    m21 = 1/m12;            %
    %
    %  Solve for Fresnel reflection coefficients.  Note the convention "12"
    %  implies "Region 1 looking into Region 2" and vica versa.  See the
    %  nested function provided within this code for details.
    r12 = Fresnel_REFL(kz(m),kz(m+1),m12,TE);
    r21 = Fresnel_REFL(kz(m+1),kz(m),m21,TE);

    %  Transmission coefficients.
    t12 = 1 + r12;
    t21 = 1 + r21;

    %  For the final iteration, the Bmbm term is zero.  Otherwise, follow
    %  the formula.
    if m == M-1
        Bmbm = 0;
    else
        Bmbm = (B(m) - r12*A(m)*am)/t21;
    end

    %  Solve for the wave amplitudes in the next region.
    A(m+1) = r21*Bmbm + t12*A(m)*am;
    B(m+1) = Bmbm/bm;


end

%  End main function.
return;


%==========================================================================
%
%   Complex Fresnel reflection coefficient at a planar boundary.
```

```
%
%       r = Fresnel_REFL(k1z,k2z,m,TE) returns the complex-valued
%   reflection coefficient for an EM wave incident on a planar boundary
%   between two dielectric media.  For TE polarization, the coefficient is
%   with respect to the electric fields.  For TM, it computes the magnetic
%   field reflection coefficient.
%
%   INPUTS:
%
%     k1z = Z-component to the wavenumber in Region 1.
%     k2z = Z-component to the wavenumber in Region 2.
%       m = Complex-valued scalar representing the reduced index of
%           refraction (n2/n1), where n1 is the index of refraction for
%           Region 1 and n2 is the index for Region 2.
%      TE = Boolean flag that tells Matlab if the incident polarization is
%           transverse electric (TE == 1) or transverse magnetic (TE == 0).
%           For TE polarization, the incident E-field is y-polarized.  For
%           TM, the H-field is y-polarized.
%
%       System geometry is indicated below:
%
%
%
%                     (n1)                    (n2)
%                   REGION 1          |     REGION 2
%                                     |
%                                     |
%                                     |
%              Reflected Wave  \      |
%                               \     |
%                                \    |                    ^ x
%                                 \   |                    |
%                                  \  |                    |
%                                   \ |                    |
%                   ------------------|                    ------> z
%                                 |   /|
%                    THETA_i      |  / |
%                                  \/  |
%                                  /   |
%                                 /    |
%                                /     |
%                  Incident Wave       |
%                                      |
%
%
%   REFERENCES:
%       "Fundamentals of Applied Electromagnetics," 5th Edition, by Fawwaz
%   Ulaby.  In particular, see Equations (8.60) and (8.68).
%
%=========================================================================
function r = Fresnel_REFL(k1z,k2z,m,TE)

if TE
    r = (k1z - k2z) / (k1z + k2z) ;
else
    r = (k1z*m^2 - k2z) / (k1z*m^2 + k2z) ;
end

return
```

```
%=========================================================================
%
%   Complex reflection coefficient at a multi-layered planar boundary.
%
%       This function applies the recursive relation outlined in Kong,
%   pages 388 - 390.  Note that I actually tweaked the expressions to make
%   the formula simpler and more numerically robust.
%
%   INPUTS:
%        n = Complex indices of refraction for each region in the stack.
%       kz = z-components of the wavenumbers in each region (rad/m).
%        D = Vector of distances for each planar boundary (m).
%       TE = Transverse electric flag.  Use TE == 1 for transverse electric.
%            Otherwise, set TE == 0 for transverse magnetic.
%        m = Iteration number in the recusion.  Start at 1.  When m == M,
%            the recursion terminates.
%
%=========================================================================
function R_0 = solve_layered_reflection(n,kz,D,TE,m)

%  Solve for fractional coefficients in the recursion relation.  These vary
%  depending on polarization.
if TE
    u1 = kz(m) - kz(m+1) ;
    u2 = kz(m) + kz(m+1) ;
else
    u1 = kz(m)*n(m+1)^2 - kz(m+1)*n(m)^2 ;
    u2 = kz(m)*n(m+1)^2 + kz(m+1)*n(m)^2 ;
end


%  Solve for the first exponential term.  For m == 1, D(m-1) = 0, and so ai
%  is just unity.
if m == 1
    ai = 1;
else
    ai = exp(+1j*kz(m)*( D(m) - D(m-1) ) );
end

%  Recursion terminator.
if m == length(D)
    R_0 = ai*u1/u2;
    return;
else

    %  If the recursion has not yet terminated, then we need this
    %  coefficient as well.
    bi = exp(-1j*kz(m+1)*( D(m) - D(m+1) ) );

    %  Solve for the next recursion term.
    r = solve_layered_reflection(n,kz,D,TE,m+1);

    %  Re-expression of equation 3.4.68 in Kong.  Writing it this way is
    %  simpler and much more numerically stable.
    R_0 = ai * ( u1 + u2*bi*r ) / (u2 + u1*bi*r) ;

end
```

```
return;
```

B.2 Asymmetric Waveguide Solver

This function solves for the eigenmodes of the asymmetric three-layer dielectric waveguide with arbitrary gain and loss in each region. The algorithm utilizes the steepest decent method with linear line search as explained in Chapter 3.

```
%=========================================================================
%
%   Solve for transverse wavenumber of a lossy symmetric dielectric slab
%   waveguide.
%
%   [kx] = solve_lossy_symmetric_slab(PARAMS) solves for a complex-valued
%   transverse wavenumber component (kx) in a lossy, symmetric, dielectric
%   slab waveguide.  The allowed kx value is found by applying the steepest
%   descent method with linear line search (SDMLLS).  The user must
%   therefore specify a starting point from which to iteratively find a
%   solution.  The PARAMS structure contains all the information needed by
%   the function in order to calculate the kx solution.
%
%   INPUT PARAMETERS
%
%   PARAMS.h  = Film half-width (m).  Total slab width = 2*h.
%   PARAMS.k0 = Free-space wavenumber of excitation (rad/m).
%   PARAMS.nc = Complex index of refraction for the cladding.
%   PARAMS.nf = Complex index of refraction for the film.
%   PARAMS.ns = Index of refraction for the substrate.
%   PARAMS.kx0 = Initial guess for kx.  The solution is found iteratively,
%                and so needs an initial trial value.
%   PARAMS.TE   = Flag that indicates TE/TM polarization.  For TE == 1, the
%                electric field is y-polarized.  Otherwise, the H-field
%                is y-polarized.
%   PARAMS.errTol = Error tolerance of the mistfit function.  When the
%                misfit falls below this value, the solution search
%                terminates.
%
%
%    See the system geometry below:
%
%
%                                      nc      (Region 1)
%       ------------------------------------------------------------------
%                                                                        |
%                                                                        |
%             kx                                                         |
%              ^                                                         |
%              |                                                         |  2h
%              |                        nf      (Region 2)               |
%              |                                                         |
%              ------> kz                                                |
%                                                                        |
%                                                                        |
%       ------------------------------------------------------------------
%                                      ns      (Region 1)
```

```
%
%
%
%   OUTPUT VARIABLES
%
%       kx  = Final iterative solution for the transverse wavenumber
%             (rad/m).
%       M   = History of iterated search values to find kx.  Note that
%             M(end) == kx.
%       PHI = Misfit function used to compute kx.  This will vary depending
%             on even/odd mode solutions, TE/TM, and choice of branch
%             cut.
%
%
%=========================================================================
%
%   James Nagel
%   Department of Electrical and Computer Engineering
%   University of Utah, Salt Lake City, Utah
%   nageljr@ieee.org
%   Copyright August 18, 2011


function [kx M PHI] = solve_lossy_asymmetric_slab(PARAMS)

% Extract system parameters.
h    = PARAMS.h;            % Film half-thickness (m).
k0   = PARAMS.k0;           % Free-space wavenumber (rad/m).
nc   = PARAMS.nc;           % Cladding index.
nf   = PARAMS.nf;           % Film index.
ns   = PARAMS.ns;           % Substrate index.
kx0  = PARAMS.kx0;          % Initial trial solution for kx.
TE   = PARAMS.TE;           % Transverse electric/magnetic flag.
errTol = PARAMS.errTol;     % Error tolerance.
maxIter = PARAMS.maxIter;   % Maximum iterations to attempt solution.

% Check for defaults with the branch-cut conditions.
if (~isfield(PARAMS,'BC1'))
    BC1 = 0;
else
    BC1 = PARAMS.BC1;
end

if (~isfield(PARAMS,'BC2'))
    BC2 = 0;
else
    BC2 = PARAMS.BC2;
end

% Wavenumbers in each region.
kc = k0*nc;
kf = k0*nf;
ks = k0*ns;

% Define branch cut parameters.  These simply add a negative sign to the
% square-root functions when solving for uc and us.
if BC1
    T1 = -1;
else
```

```
    T1 = 1;
end
if BC2
    T2 = -1;
else
    T2 = 1;
end

% Reduced dielectric constant for TM case.
Mc = (nf/nc)^2;
Ms = (nf/ns)^2;

% Propagation constants for cladding/substrate regions as a function of
% transverse wavenumber kx.
uc  = @(kx) T1*sqrt(kc^2 + kx.^2 - kf^2);   % Cladding.
us  = @(kx) T2*sqrt(ks^2 + kx.^2 - kf^2);   % Substrate.

% Derivatives of the cladding/substrate regions as a funciton of kx.
duc = @(kx) T1*kx ./ sqrt(kc^2 + kx.^2 - kf^2); % Cladding.
dus = @(kx) T2*kx ./ sqrt(ks^2 + kx.^2 - kf^2); % Substrate.

% Modify functions for TM case.
if ~TE
    uc  = @(kx) uc(kx)*Mc;
    us  = @(kx) us(kx)*Ms;
    duc = @(kx) duc(kx)*Mc;
    dus = @(kx) dus(kx)*Ms;
end

% Residual function.
f = @(kx) tan( 2*kx* h ) .* ( kx.^2 + uc(kx).*us(kx) ) ...
    + 1j*kx.*( uc(kx) + us(kx) ) ;

% Frechet derivative of residual.
F = @(kx) tan( 2*kx* h ) ...
        .* ( 2*kx + uc(kx).*dus(kx) + duc(kx).*us(kx) ) ...
        + 2*h*sec(2*kx*h).^2 .* (kx.^2 + uc(kx).*us(kx) ) ...
        + 1j*kx.*(duc(kx) + dus(kx)) + 1j*(uc(kx) + us(kx) );

% Define the misfit function.
PHI = @(kx) abs(f(kx)).^2 ;

% Initial guess of "model" value.
kx_n = kx0;

% Model history.
M    = zeros(1,maxIter);
M(1) = kx_n;

% Instantiate iteration counter.
I = 1;

% Begin search algorithm.
while PHI(kx_n) >= errTol

    % Update the iteration count.
    I = I + 1;

    % If too many iterations have gone by, then just give up.
```

```
    if I > maxIter
        I = I-1;
        warning('No solutions found within error tolerance.');
        break;
    end

    % Residual.
    r = f(kx_n);

    % Frechet derivative.
    Fm = F(kx_n);

    % Line search parameters.
    Ln = conj(Fm)*r;
    gn = -Fm*Ln;

    % Step size.
    kn = abs(Ln)^2 / abs(gn)^2 ;

    % Tentative iteration for the next step.
    kx_X = kx_n - kn * Ln;

    % Check to see if the next step is better or worse than before.  If it
    % is better, then continue the algorithm.  If not, then keep reducing
    % the line-step by half until it is.
    while PHI(kx_X) > PHI(kx_n)

        kn = 0.5*kn;

        % Tentative iteration for the next step.
        kx_X = kx_n - kn * Ln;

    end

    % Store the model value for next iteration.
    kx_n = kx_X;

    % Store the model value for keeping track of the search path.
    M(I) = kx_n;

end

% Truncate any unused values in M.
M = M(1:I);

% Store the final return value.
kx = kx_n;
```

B.3 Mie Theory Calculations

Calculations of scattering efficiency for spherical particles may be accomplished using standard Mie theory as outlined in Ref. [60]. However, when the ambient medium is lossy, the standard formulations must be modified. This theory was first laid out in Ref. [61], and is implemented in the following sections.

B.3.1 Riccatti Bessel Functions

When performing calculations within Mie theory, a peculiar set of functions will periodically appear that require special attention. These functions are the *Riccatti Bessel functions* and the *Riccatti Hankel functions*. If we define $J_n(x)$ as the ordinary Bessel function of order n, then the Riccatti Bessel function is defined as

$$S_n(x) = \sqrt{\frac{\pi x}{2}} J_{n+1/2}(x) \ . \tag{B.1}$$

In a similar manner, we may let $H_n^{(1)}(x)$ be the ordinary Hankel function of the first kind, thus giving the Riccatti Hankel function of the first kind as

$$\xi_n^(x) = \sqrt{\frac{\pi x}{2}} H_{n+1/2}^{(1)}(x) \ . \tag{B.2}$$

Because Matlab has built-in functions for calculating $J_n(x)$ and $H_n^{(1)}(x)$, it is a simple matter to implement functions for $S_n(x)$ and $\xi_n^(x)$.

Two more functions that frequently occurs in Mie theory are the derivatives of the Riccatti Bessel and Hankel functions. These may be readily calculated by noting the recurrence relation

$$\frac{d}{dx} J_n(x) = J_{n-1}(x) - \frac{n}{x} J_n(x) \ . \tag{B.3}$$

Note that this same relation applies for $H_n(x)$ as well. From this, we may readily compute the derivative of the Riccatti Bessel function as

$$S_n'(x) = \sqrt{\frac{\pi x}{2}} J_{n-1/2}(x) - n\sqrt{\frac{\pi}{2x}} J_{n+1/2}(x) \ . \tag{B.4}$$

In a similar fashion, we also have

$$\xi_n'(x) = \sqrt{\frac{\pi x}{2}} H_{n-1/2}^{(1)}(x) - n\sqrt{\frac{\pi}{2x}} H_{n+1/2}^{(1)}(x) \ . \tag{B.5}$$

B.3.2 Mie Coefficients

This next function is a supplement to the previous function, and simply computes the standard Mie coefficients, a_n and b_n. These coefficients are necessary in order to compute the extinction absorption, and scattering efficiencies of spherical particle. Also note that these formulations do not change for the case of a lossy ambient medium.

```
%=========================================================================
%
%   Compute Mie Coefficient Vectors, a_n and b_n.
%
%       [a, b] = Mie_3D_ab(m,x) computes two vectors of Mie coefficients.
%   Values are computed using the formulation described in "Absorption and
```

```
%   Scattering of Light by Small Particles,"  by Bohren and Huffman, 1983.
%   See equations 4.56 and 4.57 on page 101.
%
%   INPUTS:
%       m = Relative index of refraction for particle with respect to host
%           medium.  That is, m = n_sphere / n_medium.
%       x = Size parameter (k*r) of the sphere relative to the ambient
%           medium, where k is the wavenumber in ambient medium and
%               'r' is the radius of the sphere.  Note that x can be complex.
%
%=========================================================================
%
%   James Nagel
%   Department of Electrical and Computer Engineering
%   University of Utah, Salt Lake City, Utah
%   nageljr@ieee.org
%   Copyright October 18, 2010

function [a, b] = Mie_3D_ab(m,x)

% Compute product between index and size parameter.
mx = m*x;

% Truncation point for computing coefficients.  See Appendix A in B & H,
% page 477.
N_STOP = round( abs(x + 4*x^(1/3) + 2 ) );

% Termination condition for coefficients.  When the latest coefficient in
% the series is some tiny fraction of the first coeffcient, that is, when
% a(n) < err*a(1) and b(n) < err*b(1), then the series is assumed to have
% converged and the calculations terminate.
err = 1e-6;

% Instantiate scattering coefficients.
a = zeros(N_STOP,1);
b = zeros(N_STOP,1);

% Compute scattering coefficients from Equations 8.30 and 8.32 from Bohren
% and Huffman, page 199.  Note that Matlab is able to compute these
% directly, thanks to the built-in Bessel functions.  We therefore do not
% need to bother with the recusion algorithm used by B&H in Appendix C.
for n = 1:N_STOP

    % Evaluate Riccati-Bessel function and its derivative at m*x.
    S1  = riccati_bessel(n,mx);
    dS1 = riccati_bessel_dx(n,mx);

    % Repeat above at x.
    S2  = riccati_bessel(n,x);
    dS2 = riccati_bessel_dx(n,x);

    % Evaluate Riccati-Hankel function and its derivative at m*x.
    E1  = riccati_hankel(n,x);
    dE1 = riccati_hankel_dx(n,x);

    % Compute numerators.
    Fa = m*S1*dS2 -   S2*dS1;
    Fb =   S1*dS2 - m*S2*dS1;
```

```
    % Compute denominators.
    Ga = m*S1*dE1 -   E1*dS1;
    Gb =   S1*dE1 - m*E1*dS1;

    % Finally compute scattering coefficients.
    a(n) = Fa/Ga;
    b(n) = Fb/Gb;

    % Check for early convergence and terminate.
    diff1 = abs(a(n)) / abs(a(1));
    diff2 = abs(b(n)) / abs(b(1));
    if ( diff1 < err ) && ( diff2 < err )
        a = a(1:n);
        b = b(1:n);
        break;
    end

end

return;

%=========================================================================
% Riccati-Bessel function.
%       n = Function order
%       x = argument
%=========================================================================
function S = riccati_bessel(n,x)

% Riccati-Bessel function definition.
S = sqrt(x*pi/2) * besselj(n+1/2,x);

return;

%=========================================================================
% Riccati-Bessel function derivative.
%       n = Function order
%       x = argument
%=========================================================================
function dS = riccati_bessel_dx(n,x)

% Coefficients.
a = sqrt(x*pi/2);
b = sqrt(pi/2./x)*(n);

% This is how you compute the derivative.
dS = a .* besselj(n-1/2,x) - b .* besselj(n+1/2,x);

return;


%=========================================================================
%  Riccati-Hankel function.
%       n = Function order
%       x = argument
%=========================================================================
function E = riccati_hankel(n,x)

E = x.*sqrt(pi./(2*x)).*besselh(n+1/2,x);
```

```
return;

%=========================================================================
%   Derivative of Riccati-Hankel function.
%       n = Function order
%       x = argument
%=========================================================================
function dE = riccati_hankel_dx(n,x)

% Leading coefficient terms.
a = sqrt(x*pi/2);
b = sqrt(pi/2./x)*(n);

% This is how you compute the derivative.
dE = a .* besselh(n-1/2,x) - b .* besselh(n+1/2,x);

return;
```

B.3.3 Mie Efficiencies

This function computes the extinction Q_e, absorption Q_a, and scattering Q_s efficiencies of a spherical particle embedded in a uniform, isotropic medium. Note that the previous function is necessary in order for this function to work.

```
%=========================================================================
%
%   Compute Mie Efficiencies for Scattering, Absorption and Extinction.
%
%       [Qext Qsca Qabs] = Mie_3D_Q(n_med, n_sph, x) computes the
%   extinction, scattering, and absorption efficiencies (Qext, Qsca, and
%   Qabs) for a spherical particle embedded in some ambient medium.  Values
%   are computed using the formulation described in "Absorption and
%   Scattering of Light by Small Particles," by Bohren and Huffman, 1983.
%   See equations 4.61, and 4.62 on page 103.
%
%   INPUTS:
%       n_med = Complex index of refraction (n' + j*n") of the ambient
%               medium.
%       n_sph = Complex index of refraction (n' + j*n") of the spherical
%               particle.
%       x     = Size parameter of the sphere, where x = k*r. 'k' is the
%               wavenumber in ambient medium and 'r' is radius of the
%               sphere.  Note that k (and therefore x) can be complex for
%               lossy media.  For example, if k0 is the wavenumber in
%               free-space, then k = k0*n_med.
%
%   OUTPUTS:
%       Qext = Extinction efficiency.
%       Qsca = Scattering efficiency.
%       Qabs = Absorption efficiency.
%
%       REQUIRED FUNCTIONS:
%           Mie_3D_ab.m
%
%       Note that if n_med (and therefore x) is a complex number, then the
%   formulation is slightly different from the standard Bohren and Huffman
%   equations.  In this special case, the formulation is taken from the
```

```
%   following reference:
%
%       I. W. Sudiarta and P. Chylek, "Mie-scattering formalism for
%   spherical particles embedded in an absorbing medium," J. Opt. Soc. Am.
%   A, Vol 18, No. 6, June 2001.
%
%       Bear in mind that I have simplified Sudiarta's math for the sake of
%   writing this code, which means the expressions are formulated
%   differently.  Nevertheless, the results are equivalent and may be
%   readily validated against his paper.
%
%==========================================================================
%
%   James Nagel
%   Department of Electrical and Computer Engineering
%   University of Utah, Salt Lake City, Utah
%   nageljr@ieee.org
%   Copyright October 18, 2010

function [Qext, Qsca, Qabs] = Mie_3D_Q(n_med, n_sph, x)

% Check for errors in input.
if length(n_med) > 1
    error('Error:  n_med must be a scalar.');
end
if length(n_sph) > 1
    error('Error:  n_sph must be a scalar.');
end
if length(x) > 1
    error('Error:  x must be a scalar.');
end


% Prevents any singularities that occur at a = 0.
if x == 0
    Qext = 0;
    Qsca = 0;
    Qabs = 0;
    return;
end

% Compute relative index of refraction for particle with respect to host
% medium.
m = n_sph / n_med;

% Compute the Mie a-b coefficients.
[a, b] = Mie_3D_ab(m,x);

% Extract vector size.
N = length(a);

% If x is a real number, then use standard Bohren and Huffman equations.
if imag(x) == 0

    % Summation indices.
    n = [1:N];

    % Leading coefficients in summations.
    cn = 2*n + 1;
```

```
    cn = cn.';

    % Coefficient magnitudes.
    A = abs(a).^2;
    B = abs(b).^2;

    % See equations 4.61 and 4.62. By dividing by x^2, we are able to
    % skip over the cross sections and directly compute the Mie
    % efficiencies.
    q    = 2/x^2;                        % Leading coefficient.
    Qsca = q*sum( cn.*(A + B) );
    Qext = q*sum( cn.*real(a + b) );

    % Store absorption efficiency.
    Qabs = Qext - Qsca;

else

    % If x is complex, use Sudiarta's modified formulations. This will
    % take significantly longer because we now have to re-compute the
    % Riccati-Bessel/Hankel functions.

    % Instantiate summation parameters.
    Yext = 0;
    Yabs = 0;
    Ysca = 0;

    for n = 1:N

        cn = 2*n + 1;

        % Evaluate Riccati-Bessel function and its derivative at x.
        Psi  = riccati_bessel(n,x);
        dPsi = riccati_bessel_dx(n,x);

        % Evaluate Riccati-Hankel function and its derivative at x.
        Xi  = riccati_hankel(n,x);
        dXi = riccati_hankel_dx(n,x);

        % Prepare summation terms. See Sudiarta, 2001.
        A = 1j*conj(Psi)*dPsi           - 1j*Psi*conj(dPsi);
        B = 1j*b(n)*conj(dPsi)*Xi       + 1j*conj(b(n))*Psi*conj(dXi);
        C = 1j*abs(a(n))^2*dXi*conj(Xi) - 1j*abs(b(n))^2*Xi*conj(dXi);
        D = -1j*a(n)*conj(Psi)*dXi      - 1j*conj(a(n))*dPsi*conj(Xi);

        % Add terms to the summation.
        Yext = Yext + cn*( A + B + D );
        Yabs = Yabs + cn*( A + B + C + D );
        Ysca = Ysca + cn*( - C );

    end

    % Prepare final coefficients.
    mr = real(n_med);
    xI = imag(x);

    % This next term behaves very poorly for small values of xI, so
    % replace it with the limiting value for tiny inputs.
    if xI < 1e-6
```

```
        Z = 0.5;            % Limiting value for small xI.
    else
        % This is the true expression for Z.
        Z = exp(2*xI) / (2*xI) + (1 - exp(2*xI) )/(4*xI^2);
    end

    % One last parameter.
    A = (1/abs(x)^2)*(1/mr)/Z;

    % Finally, compute the Mie efficiencies. See Sudiarta, 2001.
    Qext = A*real( conj(n_med)*Yext );
    Qabs = A*real( conj(n_med)*Yabs );
    Qsca = A*real( conj(n_med)*Ysca );

end


%=========================================================================
% Riccati-Bessel function.
%       n = Function order
%       x = argument
%=========================================================================
function S = riccati_bessel(n,x)

% Riccati-Bessel function definition.
S = sqrt(x*pi/2) * besselj(n+1/2,x);

return;

%=========================================================================
% Riccati-Bessel function derivative.
%       n = Function order
%       x = argument
%=========================================================================
function dPsi = riccati_bessel_dx(n,x)

% Riccati-Bessel function definition.
a = sqrt(x*pi/2);
b = sqrt(pi/2./x)*(n);

dPsi = a .* besselj(n-1/2,x) - b .* besselj(n+1/2,x);

return;


%=========================================================================
%  Riccati-Hankel function.
%       n = Function order
%       x = argument
%=========================================================================
function E = riccati_hankel(n,x)

% Riccati-Bessel function definition.
E = x.*sqrt(pi./(2*x)).*besselh(n+1/2,x);

return;

%=========================================================================
%  Derivative of Riccati-Hankel function.
```

```
%       n = Function order
%       x = argument
%=========================================================================
function dXi = riccati_hankel_dx(n,x)

% Leading coefficient terms.
a = sqrt(x*pi/2);
b = sqrt(pi/2./x)*(n);

% Derivative.
dXi = a .* besselh(n-1/2,x) - b .* besselh(n+1/2,x);

return;
```

B.4 Coated Spheres

The Mie efficiencies of the coated spherical particles from Chapter 5 can likewise be computed through similar calculations as a bare sphere. However, the computations for this case are significantly more complicated. Ref. [60] also includes a derivation for the lossless case, which is applied in this section. The case of coated spheres in a lossy ambient medium is more complicated still, but has not been utilized in this research. For the case of crystalline silicon, loss may generally be neglected at wavelengths above 500 nm as long as the particles are not too large.

B.4.1 Coated Mie Coefficients

The Mie coefficients a_n and b_n must be modified for the case of coated spheres. This special case also requires the Riccatti Bessel function of the *second kind*, which is defined as

$$\chi_n(x) = -\sqrt{\frac{\pi x}{2}} Y_{n+1/2}(x) \ , \tag{B.6}$$

where $Y_n(x)$ is the ordinary Bessel function of the second kind. Note also the derivative of $\chi_n(x)$, which is given by

$$\chi_n'(x) = -\sqrt{\frac{\pi x}{2}} Y_{n-1/2}(x) + n\sqrt{\frac{\pi}{2x}} Y_{n+1/2}(x) \ . \tag{B.7}$$

```
%=========================================================================
%
%   Compute Mie Coefficient Vectors, a_n and b_n for COATED sphere.
%
%       [a, b] = Mie_3D_coated_ab(m1,m2,x,y) computes two vectors of Mie
%   coefficients for a COATED particle in some ambient medium.  Values are
%   computed using the formulation described in "Absorption and Scattering
%   of Light by Small Particles,"  by Bohren and Huffman, 1983. See
%   equation 8.2 on page 183.
%
%   INPUTS:
```

```
%       m1 = Refractive index of the CORE relative to the surrounding
%            medium; ie, m1 = n_core / n_medium .
%       m2 = Refractive index of the SHELL relative to the surrounding
%            medium; ie, m1 = n_core / n_medium .
%            medium.  That is, m = n_sphere / n_medium.
%        x = Size parameter (k*a) of the CORE relative to the ambient
%            medium, where k is the wavenumber in ambient medium and
%                'a' is the radius of the core.
%        y = Size parameter (k*b) of the SHELL relative to the ambient
%            medium, where k is the wavenumber in ambient medium and
%                'b' is the radius of the shell.  Note that b > a.
%
%==========================================================================
%
%   James Nagel
%   Department of Electrical and Computer Engineering
%   University of Utah, Salt Lake City, Utah
%   nageljr@ieee.org
%   Copyright October 18, 2010

function [a, b] = Mie_3D_coated_ab(m1,m2,x,y)

% Precompute Bessel-function arguments.
m1x = m1*x;
m2y = m2*y;
m2x = m2*x;

% Truncation point for computing coefficients.  See Appendix A in B & H,
% page 477.
N_STOP = round( abs(y + 4*y^(1/3) + 2 ) );

% Termination condition for coefficients.  When the latest coefficient in
% the series is some tiny fraction of the first coeffcient, that is, when
% a(n) < err*a(1) and b(n) < err*b(1), then the series is assumed to have
% converged and the calculations terminate.
err = 1e-6;

% Instantiate scattering coefficients.
a = zeros(N_STOP,1);
b = zeros(N_STOP,1);

% Compute scattering coefficients from Equations 8.30 and 8.32 from Bohren
% and Huffman, page 199.  Note that Matlab is able to compute these
% directly, thanks to the built-in Bessel functions.  We therefore do not
% need to bother with the recusion algorithm used by B&H in Appendix C.
for n = 1:N_STOP

    % Evaluate Riccati-Bessel function at required arguments.
    Psi_y  = riccati_bessel_Psi(n,y);
    Psi_m1x = riccati_bessel_Psi(n,m1x);
    Psi_m2x = riccati_bessel_Psi(n,m2x);
    Psi_m2y = riccati_bessel_Psi(n,m2y);

    % Evaluate Riccati-Bessel functions of second kind.
    Chi_m2x = riccati_bessel_Chi(n,m2x);
    Chi_m2y = riccati_bessel_Chi(n,m2y);

    % Evaluate Riccati-Hankel functions.
    Xi_y = riccati_hankel(n,y);
```

```
    % Now evaluate all the derivatives.
    dPsi_y   = riccati_bessel_Psi_dx(n,y);
    dPsi_m1x = riccati_bessel_Psi_dx(n,m1x);
    dPsi_m2x = riccati_bessel_Psi_dx(n,m2x);
    dPsi_m2y = riccati_bessel_Psi_dx(n,m2y);
    dChi_m2x = riccati_bessel_Chi_dx(n,m2x);
    dChi_m2y = riccati_bessel_Chi_dx(n,m2y);
    dXi_y    = riccati_hankel_dx(n,y);

    % Start computing sub-coefficients. Begin with numerators. See
    % equation 8.2 in B&H.
    FA = m2*Psi_m2x*dPsi_m1x - m1*dPsi_m2x*Psi_m1x;
    FB = m2*Psi_m1x*dPsi_m2x - m1*Psi_m2x*dPsi_m1x;

    % Compute denominators.
    GA = m2*Chi_m2x*dPsi_m1x - m1*dChi_m2x*Psi_m1x;
    GB = m2*dChi_m2x*Psi_m1x - m1*Chi_m2x*dPsi_m1x;

    % Compute sub-coefficients.
    An = FA / GA;
    Bn = FB / GB;

    % Now start computing the final coefficients, beginning with
    % numerators.
    Fa =  Psi_y    *( dPsi_m2y - An*dChi_m2y ) ...
        - m2*dPsi_y*( Psi_m2y  - An*Chi_m2y  );
    Fb =  m2*Psi_y *( dPsi_m2y - Bn*dChi_m2y ) ...
        -    dPsi_y*( Psi_m2y  - Bn*Chi_m2y  );

    % Denominators.
    Ga =  Xi_y     *( dPsi_m2y - An*dChi_m2y ) ...
        - m2*dXi_y*( Psi_m2y  - An*Chi_m2y  );
    Gb =  m2*Xi_y  *( dPsi_m2y - Bn*dChi_m2y ) ...
        -    dXi_y*( Psi_m2y  - Bn*Chi_m2y  );

    % Finally, compute scattering coefficients.
    a(n) = Fa/Ga;
    b(n) = Fb/Gb;

    % Check for early convergence and terminate.
    diff1 = abs(a(n)) / abs(a(1));
    diff2 = abs(b(n)) / abs(b(1));
    if ( diff1 < err ) && ( diff2 < err )
        a = a(1:n);
        b = b(1:n);
        break;
    end

end

return;

%=======================================================================
%  Riccati-Bessel function of the first kind.
%       n = Function order
%       x = argument
%=======================================================================
function Psi = riccati_bessel_Psi(n,x)
```

```
% Riccati-Bessel function definition.
Psi = sqrt(x*pi/2) * besselj(n+1/2,x);

return;

%=========================================================================
% Riccati-Bessel function derivative.
%       n = Function order
%       x = argument
%=========================================================================
function dPsi = riccati_bessel_Psi_dx(n,x)

% Coefficients.
a = sqrt(x*pi/2);
b = sqrt(pi/2./x)*(n);

% This is how you compute the derivative.
dPsi = a .* besselj(n-1/2,x) - b .* besselj(n+1/2,x);

return;

%=========================================================================
% Riccati-Bessel function of second kind.
%       n = Function order
%       x = argument
%=========================================================================
function Chi = riccati_bessel_Chi(n,x)

% Riccati-Bessel function definition.
Chi = -sqrt(x*pi/2) * bessely(n+1/2,x);

return;


%=========================================================================
% Riccati-Bessel function of second kind derivative.
%       n = Function order
%       x = argument
%=========================================================================
function dChi = riccati_bessel_Chi_dx(n,x)

% Leading coefficient terms.
a = -sqrt(x*pi/2);
b = -sqrt(pi/2./x)*(n);

% This is how you compute the derivative.
dChi = a .* bessely(n-1/2,x) - b .* bessely(n+1/2,x);

return;

%=========================================================================
%  Riccati-Hankel function.
%       n = Function order
%       x = argument
%=========================================================================
function Xi = riccati_hankel(n,x)

% Compute spherical Bessel function.
```

```
f = sqrt(pi/(2*x));
h_n = f * besselj(n+1/2,x) + (1i*f) * bessely(n+1/2,x);

%  Riccati-Hankel definition.
Xi = x*h_n;

return;

%=========================================================================
%   Derivative of Riccati-Hankel function.
%       n = Function order
%       x = argument
%=========================================================================
function dXi = riccati_hankel_dx(n,x)

%  Leading coefficient terms.
a = sqrt(x*pi/2);
b = sqrt(pi/2./x)*(n);

%  This is how you compute the derivative.
dXi = a .* besselh(n-1/2,x) - b .* besselh(n+1/2,x);

return;
```

B.4.2 Coated Mie Efficiencies

This function computes the extinction Q_e, absorption Q_a, and scattering Q_s efficiencies of a coated spherical particle embedded in a uniform, isotropic medium. Note that the previous function is necessary in order for this function to work.

```
%=========================================================================
%
%   Compute Mie Efficiencies for Coated Spheres.
%
%       [Qext Qsca Qabs] = Mie_3D_coated_Q(n, n1, n2, x, y) computes the
%   extinction, scattering, and absorption efficiencies (Qext, Qsca, and
%   Qabs) for a COATED spherical dielectric particle embedded in some
%   arbitrary (lossless) dielectric medium.  Values are computed using the
%   formulation described in "Absorption and Scattering  of Light by Small
%   Particles," by Bohren and Huffman, 1983.  See equations 4.61, and 4.62
%   on page 103.  For extension to coated spheres, see equation 8.2 on page
%   183.
%
%   INPUTS:
%       n0 = REAL-VALUED index of refraction of the ambient medium.
%       n1 = Complex index of refraction (n' + j*n") of the CORE of the
%               spherical particle.
%       n2 = Complex index of refraction (n' + j*n") of the SHELL around
%               core of the spherical particle.
%       x  = Size parameter of the core, where x = k*r. 'k' is the
%               wavenumber in ambient medium and 'r' is radius of the
%               spherical core.  Note that k (and therefore x) can be
%               complex for lossy media, but has not been formulated yet
%               and will give bogus results.
%       y  = Size parameter of the shell, where y = k*R. 'k' is the
%               wavenumber in ambient medium and 'R' is outer radius of the
%               spherical shell.  Again, note that k (and therefore y) can
```

```
%               be complex for lossy media, but has not been formulated yet
%               and will give bogus results.
%
%   OUTPUTS:
%       Qext = Extinction efficiency.
%       Qsca = Scattering efficiency.
%       Qabs = Absorption efficiency.
%
%       REQUIRED FUNCTIONS:
%           Mie_3D_coated_ab.m
%
%=========================================================================
%
%   James Nagel
%   Department of Electrical and Computer Engineering
%   University of Utah, Salt Lake City, Utah
%   nageljr@ieee.org
%   Copyright OCtober 18, 2010

function [Qext, Qsca, Qabs] = Mie_3D_coated_Q(n0, n1, n2, x, y)

% Prevents any singularities that occur at a = 0.
if x == 0
    Qext = 0;
    Qsca = 0;
    Qabs = 0;
    return;
end

% Compute relative index of refraction for particle with respect to host
% medium.
m1 = n1 / n0;
m2 = n2 / n0;

% Compute the Mie a-b coefficients.
[a, b] = Mie_3D_coated_ab(m1,m2,x,y);

% Extract vector size.
N = length(a);

% If x is a real number, then use standard Bohren and Huffman equations.
if imag(x) == 0

    % Summation indices.
    n = [1:N];

    % Leading coefficients in summations.
    cn = 2*n + 1;
    cn = cn.';

    % Coefficient magnitudes.
    A = abs(a).^2;
    B = abs(b).^2;

    % See equations 4.61 and 4.62.  By dividing by x^2, we are able to
    % skip over the cross sections and directly compute the Mie
    % efficiencies.
    q    = 2/y^2;                       % Leading coefficient.
    Qsca = q*sum( cn.*(A + B) );
```

```
    Qext = q*sum( cn.*real(a + b) );

    % Store absorption efficiency.
    Qabs = Qext - Qsca;

else
    error('Ambient medium cannot be lossy.');
end
```

REFERENCES

[1] United States Department of Energy, "$1/W photovoltaic systems: Workshop summary," $1/W Workshop, August 2010.

[2] ——, "$1/W photovoltaic systems: White paper to explore a grand challenge for electricity from solar," $1/W Workshop, August 2010.

[3] C. Wadia, A. P. Alivisatos, and D. M. Kammen, "Materials availability expands the opportunity for large-scale photovoltaics deployment," *Environmental Science & Technology*, vol. 43, no. 6, pp. 2072–2077, February 2009.

[4] First Solar, Inc., http://investor.firstsolar.com/releasedetail.cfm?ReleaseID=571539, February 2009.

[5] V. M. Fthenakis, "Life cycle impact analysis of cadmium in CdTe PV production," *Renewable and Sustainable Energy Reviews*, vol. 8, no. 4, pp. 303–334, August 2004.

[6] F. Alharbi, J. D. Bass, A. Salhi, A. Alyamani, H.-C. Kim, and R. D. Miller, "Abundant non-toxic materials for thin film solar cells: Alternative to conventional materials," *Renewable Energy*, vol. 36, no. 10, pp. 2753–2758, October 2011.

[7] D. B. Mitzi, O. Gunawan, T. K. Todorov, K. Wang, and S. Guha, "The path towards a high-performance solution-processed kesterite solar cell," *Solar Energy Materials and Solar Cells*, vol. 95, no. 6, pp. 1421–1436, June 2011.

[8] P. P. Altermatt, T. Kiesewetter, K. Ellmer, and H. Tributsch, "Specifying targets of future research in photovoltaic devices containing pyrite (FeS_2) by numerical modelling," *Solar Energy Materials & Solar Cells*, vol. 71, no. 2, pp. 181–195, February 2002.

[9] Z. Shi and M. A. Green, "Survey of material options and issues for thin film silicon solar cells," *Progress in Photovoltaics: Research and Applications*, vol. 6, no. 4, pp. 247–257, July 1998.

[10] R. Bergmann, "Crystalline si thin-film solar cells: a review," *Applied Physics A: Materials Science & Processing*, vol. 69, no. 2, pp. 187–194, 1999.

[11] W. van Sark, G. Brandsen, M. Fleuster, and M. Hekkert, "Analysis of the silicon market: Will thin films profit?" *Energy Policy*, vol. 35, no. 6, pp. 3121–3125, 2007.

[12] J. Zhao, A. Wang, and M. A. Green, "24.5 % efficiency silicon PERT cells on MCZ substrates and 24.7 % efficiency PERL cells on FZ substrates," *Progress in Photovoltaics: Research and Applications*, vol. 7, no. 6, pp. 471–474, 1999.

[13] R. Brendel, *Thin-Film Crystalline Silicon Solar Cells: Physics and Technology*. Weinheim: Wiley-VCH, 2003.

[14] K. L. Chopra, P. D. Paulson, and V. Dutta, "Thin-film solar cells: An overview," *Progress in Photovoltaics: Research and Applications*, vol. 12, no. 2-3, pp. 69–92, March 2004.

[15] A. V. Shah, H. Schade, M. Vanecek, J. Meier, E. Vallat-Sauvain, N.Wyrsch, U. Kroll, C. Droz, and J. Bailat, "Thin-film silicon solar cell technology," *Progress in Photovoltaics: Research and Applications*, vol. 12, no. 2-3, pp. 113–142, 2004.

[16] C. Gueymard, D. Myers, and K. Emery, "Proposed reference irradiance spectra for solar energy systems testing," *Solar Energy*, vol. 73, no. 6, pp. 443–467, December 2004.

[17] http://rredc.nrel.gov/solar/spectra/am1.5/.

[18] D. Poitras and J. A. Dobrowolski, *Applied Optics*, vol. 43, no. 6, pp. 1286–1295, February 2004.

[19] W. H. Southwell, "Pyramid-array surface-relief structures producing antireflection index matching on optical surfaces," *Journal of the Optical Society of America: A*, vol. 8, no. 3, pp. 549–553, March 1991.

[20] Z. Yu, A. Raman, and S. Fan, "Fundamental limit of nanophotonic light trapping in solar cells," *Proceedings of the National Academy of Sciences*, vol. 107, no. 41, pp. 17 491–17 496, October 2010.

[21] E. Yablonovitch and G. D. Cody, "Intensity enhancement in textured optical sheets for solar cells," *IEEE Transactions on Electron Devices*, vol. 29, no. 2, pp. 300–305, February 1982.

[22] E. Yablonovitch, "Statistical ray optics," *Journal of the Optical Society of America*, vol. 72, no. 7, pp. 899–907, July 1982.

[23] S. E. Han and G. Chen, "Toward the Lambertian limit of light trapping in thin nanostructured silicon solar cells," *Nano Letters*, vol. 10, no. 11, pp. 4692–4696, October 2010.

[24] C. Seassal, Y. Park, A. Fave, E. Drouard, E. Fourmond, A. Kaminski, M. Lemiti, X. Letartre, and P. Viktorovitch, "Photonic crystal assisted ultra-thin silicon photovoltaic solar cell," *Proceedings of the SPIE*, vol. 7002, no. 1, p. 700207, 2008.

[25] S. Koynov, M. S. Brandt, and M. Stutzmann, "Black nonreflecting silicon surfaces for solar cells," *Applied Physics Letters*, vol. 88, no. 20, p. 203017, 2006.

[26] L. Zeng, Y. Yi, C. Hong, J. Liu, N. Feng, X. Duan, L. C. Kimerling, and B. A. Alamariu, "Efficiency enhancement in Si solar cells by textured photonic crystal back reflector," *Applied Physics Letters*, vol. 89, no. 11, p. 111111, 2006.

[27] H. A. Atwater and A. Polman, "Plasmonics for improved photovoltaic devices," *Nature Materials*, vol. 9, no. 3, pp. 205–213, March 2010.

[28] J. R. Nagel and M. A. Scarpulla, "Enhanced absorption in optically thin solar cells by scattering from embedded dielectric nanoparticles," *Optics Express*, vol. 18, no. S2, pp. A139–A146, June 2010.

[29] D. Wan, H.-L. Chen, T.-C. Tseng, C.-Y. Fang, Y.-S. Lai, and F.-Y. Yeh, "Antireflective nanoparticle arrays enhance the efficiency of silicon solar cells," *Advanced Functional Materials*, vol. 20, no. 18, pp. 3064–3075, September 2010.

[30] S. Nunomura, A. Minowa, H. Sai, and M. Kondo, "Mie scattering enhanced near-infrared light response of thin-film silicon solar cells," *Applied Physics Letters*, vol. 97, no. 6, p. 063507, August 2010.

[31] J. Nelson, *The Physics of Solar Cells*. London: Imperial College Press, 2003.

[32] J. A. Kong, *Electromagnetic Wave Theory*. Cambridge, MA: EMW Publishing, 2000.

[33] M.-L. Kuo, D. J. Poxson, Y. S. Kim, F. W. Mont, J. K. Kim, E. F. Schubert, and S.-Y. Lin, "Realization of a near-perfect antireflection coating for silicon solar energy utilization," *Optics Letters*, vol. 33, no. 21, pp. 2527–2529, November 2008.

[34] E. D. Palik, Ed., *Handbook of Optical Constants of Solids*. Academic Press, 1998, vol. 1.

[35] Lumerical Solutions, Inc., http://www.lumerical.com/.

[36] H. Sai, Y. Kanamori, K. Arafune, Y. Ohshita, and M. Yamaguchi, "Light trapping effect of submicron surface textures in crystalline si solar cells," *Progress in Photovoltaics*, vol. 15, no. 5, pp. 415–423, February 2007.

[37] R. Dewan, M. Marinkovic, R. Noriega, S. Phadke, A. Salleo, and D. Knipp, "Light trapping in thin-film silicon solar cells with submicron surface texture," *Optics Express*, vol. 17, no. 25, pp. 23 058–23 065, December 2009.

[38] C. A. Balanis, *Advanced Engineering Electromagnetics*. New York, NY: Wiley, 1989.

[39] G. H. Owyang, *Foundations of Optical Waveguides*. New York, NY: Elsevier, 1981.

[40] C. R. Pollock and M. Lipson, *Integrated Photonics*. Boston, MA: Kluwer Academic Publishers, 2003.

[41] A. W. Snyder and J. D. Love, *Optical Waveguide Theory*. New York, NY: Chapman and Hall, 1983.

[42] A. Reisinger, "Characteristics of optical guided modes in lossy waveguides," *Applied Optics*, vol. 12, no. 5, pp. 1015–1025, May 1973.

[43] I. P. Kaminow, W. L. Mammel, and H. P. Weber, "Metal-clad optical waveguides: Analytical and experimental study," *Applied Optics*, vol. 13, no. 2, pp. 396–405, February 1974.

[44] D. F. Nelson and J. McKenna, "Electromagnetic modes of anisotropic dielectric waveguides at p-n junctions," *Journal of Applied Physics*, vol. 38, no. 10, pp. 4057–4074, September 1967.

[45] A. E. Siegman, "Propagating modes in gain-guided optical fibers," *Journal of the Optical Society of America A*, vol. 20, no. 8, pp. 1617–1628, 2003.

[46] T. D. Visser, H. Blok, and D. Lenstra, "Modal analysis of a planar waveguide with gain and losses," *IEEE Journal of Quantum Electronics*, vol. 31, no. 10, pp. 1803–1810, 1995.

[47] J. A. Snyman, *Practical Mathematical Optimization: An Introduction to Basic Optimization Theory and Classical and New Gradient-Based Algorithms (Applied Optimization)*. Springer, 2005.

[48] M. S. Zhdanov, *Geophysical Electromagnetic Theory and Methods*. Oxford: Elsevier Science, 2009.

[49] A. W. Snyder and J. D. Love, "Goos-hanchen shift," *Applied Optics*, vol. 15, no. 1, pp. 236–238, 1973.

[50] T. D. Visser, H. Blok, and D. Lenstra, "Confinement factors and gain in optical amplifiers," *IEEE Journal of Quantum Electronics*, vol. 33, no. 10, pp. 1763–1766, 1997.

[51] G. K. M. Thutupalli and S. G. Tomlin, "The optical properties of amorphous and crystalline silicon," *Journal of Physics C: Solid State Physics*, vol. 10, no. 3, pp. 467–477, 1977.

[52] D. M. Schaadt, B. Feng, and E. T. Yu, "Enhanced semiconductor optical absorption via surface plasmon excitation in metal nanoparticles," *Applied Physics Letters*, vol. 86, no. 6, p. 063106, February 2005.

[53] C. Hägglund, M. Zäch, G. Petersson, and B. Kasemo, "Electromagnetic coupling of light into a silicon solar cell by nanodisk plasmons," *Applied Physics Letters*, vol. 92, no. 5, p. 053110, February 2008.

[54] F. J. Beck, A. Polman, and K. R. Catchpole, "Tunable light trapping for solar cells using localized surface plasmons," *Journal of Applied Physics*, vol. 105, no. 11, p. 114310, June 2009.

[55] K. R. Catchpole and A. Polman, "Design principles for particle plasmon enhanced solar cells," *Applied Physics Letters*, vol. 93, no. 19, p. 191113, November 2008.

[56] D. Derkacs, S. H. Lim, P. Matheu, W. Mar, and E. T. Yu, "Improved performance of amorphous silicon solar cells via scattering from surface plasmon polaritons in nearby metallic nanoparticles," *Applied Physics Letters*, vol. 89, no. 9, p. 093103, August 2006.

[57] S. Pillai, K. R. Catchpole, T. Trupke, and M. A. Green, "Surface plasmon enhanced silicon solar cells," *Journal of Applied Physics*, vol. 101, no. 9, p. 093105, May 2007.

[58] P. Spinelli, M. Hebbink, R. de Waele, L. B. F. Lenzmann, and A. Polman, "Optical impedance matching using coupled plasmonic nanoparticle arrays," *Nano Letters*, vol. 11, no. 4, pp. 1760–1765, 2011.

[59] D. M. Sullivan, Ed., *Electromagnetic Simulation Using the FDTD Method*. IEEE Press, 1998.

[60] C. F. Bohren and D. R. Huffman, *Absorption and Scattering of Light by Small Particles*. New York: Wiley, 1983.

[61] I. W. Sudiarta and P. Chylek, "Mie-scattering formalism for spherical particles embedded in an absorbing medium," *Journal of the Optical Society of America A*, vol. 18, no. 6, pp. 1275–1278, 2001.

[62] P. N. Saeta, V. E. Ferry, D. Pacifici, J. N. Munday, and H. A. Atwater, "How much can guided modes enhance absorption in thin solar cells?" *Optics Express*, vol. 17, no. 23, pp. 20 975–20 990, November 2009.

[63] B. R. Johnson, "Light scattering from a spherical particle on a conducting plane: I. normal incidence," *Journal of the Optical Society of America A*, vol. 9, no. 8, pp. 1341–1351, August 1992.

[64] A. A. Abouelsaood1, M. Y. Ghannam, L. Stalmans, J. Poortmans, and J. F. Nijs, "Experimental testing of a random medium optical model of porous silicon for photovoltaic applications," *Progress in Photovoltaics: Research and Applications*, vol. 9, no. 1, pp. 15–26, 2001.

[65] I. Kuzma-Filipek, F. Duerinckx, K. V. Nieuwenhuysen, J. P. G. Beaucarne, and R. Mertens, "Porous silicon as an internal reflector in thin epitaxial solar cells," *Physica Status Solidi (a)*, vol. 204, no. 5, pp. 1340–1345, May 2007.

[66] J. Zettner, M. Thoenissen, T. Hierl, R. Brendel, and M. Schulz, "Novel porous silicon backside light reflector for thin silicon solar cells," *Progress in Photovoltaics: Research and Applications*, vol. 6, no. 6, pp. 423–432, November 1998.

[67] L. M. Liz-Marzan, M. Giersig, and P. Mulvaney, "Synthesis of nanosized gold-silica core-shell particles," *Langmuir*, vol. 12, no. 18, pp. 4329–4335, September 1996.

[68] J. Li, C. Chen, and G. Shen, "The rps method applied to the numerical solution of multimode slab waveguides with complex indexes," *Journal of Lightwave Technology*, vol. 18, no. 10, pp. 1433–1436, October 2000.

[69] W.-J. Hsueh and J.-C. Lin, "Stable and accurate method for modal analysis of multilayer waveguides using a graph approach," *Journal of the Optical Society of America A*, vol. 24, no. 3, pp. 825–830, March 2007.

[70] http://refractiveindex.info/.

[71] S. Laux, N. Kaiser, A. Zöller, R. Götzelmann, H. Lauth, and H. Bernitzki, "Room-temperature deposition of indium tin oxide thin films with plasma ion-assisted evaporation," *Thin Solid Films*, vol. 335, no. 1-2, pp. 1–5, November 1998.

[72] Mathworks, http://www.mathworks.com/.